Time Resolved Anomalous Small Angle X-ray Scattering of the Sol-Gel Process

By
Twilight Barnardo

Aberystwyth University

THESIS
submitted to Aberystwyth University by Twilight Barnardo
in the subject of Physics
for the degree of
PHILOSOPHIAE DOCTOR

Abstract

This investigation employs Anomalous Small Angle X-ray Scattering (ASAXS), and further expands the technique for conducting time resolved experiments within synchrotron facilities. ASAXS utilises the absorption effects of a given element as photon energies approach an absorption edge, and is used to extract partial scattering functions of the individual species within a composite material.

In situ ASAXS is used to explore and understand the complex reactions in sol gel processing. The gelation process for zirconia, yttria stabilised zirconia (YSZ), YSZ and zirconia in silica, and zinc-silica systems are observed using in situ ASAXS across the zirconia and zinc absorption edges respectively. A new technique of high temperature time resolved double ASAXS, which explores two absorption edges in a single experiment, has also been employed to investigate phase changes during the sintering of YSZ and YSZ in silica.

A computational model for ASAXS is also proposed, which can be used as a tool for data analysis. It is shown that monochromator resolution induces an uncertainty into the correct values of the coefficients - used to extract scattering information from individual species within a composite material. The model suggests methods to reduce this uncertainty in order to converge on the correct solution. New techniques for future time resolved ASAXS experiments are also presented.

Time resolved ASAXS of the gelation process reveals contrast in the resonant term for sol-gels containing zirconia. The profile of which is independent of the relative concentrations of yttria and silica. It is proposed that the zirconia is being fully integrated into the gel network to form zirconia-silica chains. In comparison, the zinc systems did not reveal this effect, and instead display contrast in both the resonant and cross terms, implying a gel network is forming at the exclusion of zinc.

High temperature in situ double ASAXS of the YSZ materials reveals the nucleation of nano zirconia at temperatures close to 400ºC. The nano crystals grow to eventually incorporate yttria, preserving the zirconia in the cubic and tetragonal phases. Inhomogeneities are revealed during crystal growth; caused by the mixed phase states of zirconia and YSZ present in the material. It is also shown that the presence of a silica matrix delays the growth of these crystals until a temperature of 780 ºC is reached. Samples with high concentrations of yttria also reveal an additional feature beyond 900ºC indicating a saturation point for cubic YSZ formation.

To the memory of my Grandmother

Acknowledgements

Before all others, I would like to extend my deepest gratitude to my partner, Phoenix, whose support kept me sane during my research.
I would like to extend my gratitude to my supervisor, Dr Rudi Winter, for his advice and guidance throughout my PhD and thesis writing.
Special thanks is given to Dr Chris Martin, SRS Daresbury, and Armin Hoel, Sylvio Haas and Dragomir Tachev, BESSY, Berlin, for their invaluable help during my time resolved ASAXS experiments.
My deepest gratitude also goes to Dr Nicholas Terrill and his fellow beamline scientists on I22 at Diamond Light Source, for their continued help and guidance before, during and after experiments.

Funding from the Engineering and Physical Sciences Research Council is also gratefully acknowledged.

Contents

Introductory Statement

Sol-gel chemistry enables the production of novel ceramics, glasses and high purity metal oxides. Typically, a liquid organo-metallic compound such as an alkoxide is hydrolised under controlled conditions to obtain the desired product. Metal nitrate solutions can also be added to introduce dopants to the forming material.

The use of liquid precursors ensures homogeneity to the sub-nanometer level. Usually the precursors are mixed in a co-solvent such as alcohol for complete miscibility. The resultant sol is then kept at a temperature of between 50 and 80 degrees Celsius until a gel is formed. The gel can be dried in air to make a xerogel, or dried with supercritical carbon dioxide to produce an aerogel. Xerogels are then usually sintered in a furnace to give glasses and dense ceramics.

Such versatility provides the additional advantage of being able to adjust the materials and chemistry to suit. It may be desirable, for instance, to keep the precursor mixture in a constant liquid state, which can then be used for coating substrates. Ceramic fibres can be produced by drawing a highly viscous sol on the point of gelation. pH can be adjusted to induce either a clear gel (for Xerogels and Aerogels) or to force precipitation of a high purity oxide.

Despite the versatility and the obvious industrial applications sol-gel holds, the chemistry is still poorly understood. This investigation will focus on analysing sol-gel reactions using time resolved (*in situ*) X-ray scattering techniques. Ex-situ X-ray diffraction is first used to determine basic structural information on the atomic scale. In-situ small angle

scattering (SAXS) is used to track the growth of particles and networks on the nano-scale. In-situ anomalous small angle scattering (ASAXS) is then used to gather information on the roles of individual species within a composite material.

In conducting diffraction experiments I shall concentrate on the formation of zirconia derived ceramics. In particular, yttria stabilised zirconia (YSZ), which has important applications in solid-fuel cell production, and consists of two elements adjacent to each other on the periodic table. Silica-zirconia and silica-zinc systems are also explored. The compounds are important catalysts in the petroleum industry, and in ultraviolet filtering respectively.

Zirconium ions pose the advantage that their electron densities are relatively high, making them strong X-ray scatterers. The zirconium K-edge is also within range of a majority of synchrotron sources. Due to beamline experimental constraints it is only possible to do ASAXS on elements with absorption edges of between 5keV and 20keV. Yttria – zirconia systems pose the additional advantage that their absorption edges are relatively close together (1keV apart) making in-situ ASAXS studies across both absorption edges possible using modern synchrotron sources. Further understanding of this material will assist the further and more efficient development of solid fuel cells in the future.

Chapter 1

Sol Gel Processing

Sol-gel processing first began in 1845 when Ebelman reported the formation of a clear material after the slow hydrolysis of an ester of silicic acid [1]. Though his findings were not the result of a search for alternative ways of producing glass, he hoped the material could be used in the construction of optical devices. Later, in the 1930's, Geffcen and Berger of Schott Company devised a sol-gel process for dip-coating oxide layers on industrial glasses using organo-metallic precursors [2].

After the outbreak of the Second World War an interest in sol-gel came from laboratory studies. D. Roy and R. Roy conceived a method for preparing homogenous melts and glasses using a sol-gel route [3,4]. This led to an experiment by H. Shroeder in the early 60's, where he modified the refractive index of glass by coating the surface with thin layers of titanium butoxide [5]. At the same time, nuclear laboratories in the USA were already using a sol-gel route for the production of nuclear fuel pellets, which would ultimately minimise pollution hazards. Their results remained secret until the early 1970's.

By the beginning of the 1980's, several publications were released, one of which sparked major scientific interest after Dislich produced borosilicate glass by heating oxide powders obtained by a low-temperature sol-gel route [6]. This turning point launched sol-gel research as it is known today; a new branch from a pre-existing sol-gel technology.

From then on, a principle drive for sol-gel science was to manufacture glass by simply mixing several liquids at room temperature. Sol-gel techniques using other organo-metallic compounds were also devised, leading to the development of transition metal ceramics. Novel glasses, ceramics and high purity oxides could be made by varying the environment in which the precursor materials were mixed. Altering pH, for instance, while hydrolysing silicic acid esters would quickly lead to precipitation and agglomeration of silicon dioxide when slightly alkaline (pH greater than 7). A clear gel could be made in a slight acidic environment, which was found to be optimal pH 3 [7]. More acidic conditions led to a much longer gelation time, or resulted in the sol remaining a clear liquid which could then be used in dip-coating.

Gels could be further treated by either drying them in air to make xerogel. The xerogel is usually densified and sintered in a furnace to make a glass or ceramic [8]. Alternatively supercritical drying can be applied to the gels. In this process, carbon dioxide molecules replace surplus liquids in gel pores to preserve the gel network. [8,9] Such materials, known as aerogels, are known for possessing refractive indexes close to unity. Their porous structures give them ultra low density (and hence low mass) and make them one of the most efficient insulators of heat known today.[7,9] The properties of aerogels have made them ideal for insulating neutrino detectors and space satellites, where weight is a critical issue.

Today, Sol-gel technology has leant itself to a wide range of commercial applications, from solid fuel cells and oxygen sensors (YSZ), bone regeneration (calcium sol-gel), and satellite insulation (Aerogels) - to the repair of fractured car windscreens (silica sol-gel).

Traditionally sol-gels are made by the hydrolysis of metallic alkoxides in an organic solvent such as alcohol or cyclohexane [7]. As the name suggests; alkoxides are produced by the removal of a proton from an alcohol to produce an alkoxyl ligand; these ligands then bond with metallic ions. Alkoxides are popular precursors because they react readily with water, as in the following case:

$$M(OR)_x + H_20 \rightarrow HO\text{-}M(OR)_{x-1} + ROH$$

$$M(OR)_x + XH_2O \rightarrow M(OH)_x + XROH$$

Here 'OR' is the alkoxide ligand, M is the metallic ion and X is the valency of the ion. Such reactions lead to fractal polymers providing the number of bonding sites per building block is greater than two; forming a gel network, a sol or an oxide precipitate, depending on reaction environment. The ability to slow gelation and suspend particle size and growth allows one to add dopants or other alkoxides to the sol as it gels. The addition of zirconium-n-propoxide to a silica sol, for instance, produces mixed oxide catalysts useful for the n-hexane isomerisation reaction to petroleum [10-13]. Neodymia doped silica produced by the sol-gel route offers host glasses for high power laser applications [14]. Calcium-oxide gels have important applications in bone regeneration - while a careful mixing of zirconium and yttrium alkoxides gives yttria stabilised zirconia – an important material, for example, in the manufacture of oxygen sensors and coating jet engines[15].

Thus sol-gels are an attractive method for producing high quality glasses, ceramics and metallic oxides with novel properties.

1.1 Silica Sol-Gels

As previously mentioned, sol-gel techniques using silica derived materials were the first to be produced. It is also the most common technique in sol-gel science. Typically, tetraethylorthosilicate (TEOS) is mixed with an alcohol such as ethanol or isopropanol, and then hydrolysed under controlled conditions. The alcohol serves as a co-solvent to ensure complete miscibility of TEOS and water, which would otherwise not wholly blend. The addition of alcohol also aids in the slowing of hydrolysis reactions to further ensure the formation of a gel network if precipitation is not desirable. Water, in the form of a low concentration mineral acid such as nitric or hydrochloric (0.1M) is then added to the mixture while keeping the sol at a constant 50 degrees Celsius. A clear, homogenous, silica gel is obtained after three hours.

Silica readily forms a network due to the tetrahedral co-ordination of the silicon ion. In the above reaction it could be thought to proceed as follows:

$$\mathbf{Si(OC_2H_5)_4 + 4H_2O \rightarrow Si(OH)_4 + 4C_2H_5OH}$$

The introduction of protons (by, for example, nitric acid) serves to adjust the charge distribution of the TEOS molecule, resulting in a chemical polarity. This serves to promote polymerisation by means of an intermediate silica compound with a negatively

charged oxygen branch and positively charged silicon centre. The charged molecules can then attract and join with others as a silica polymer network.

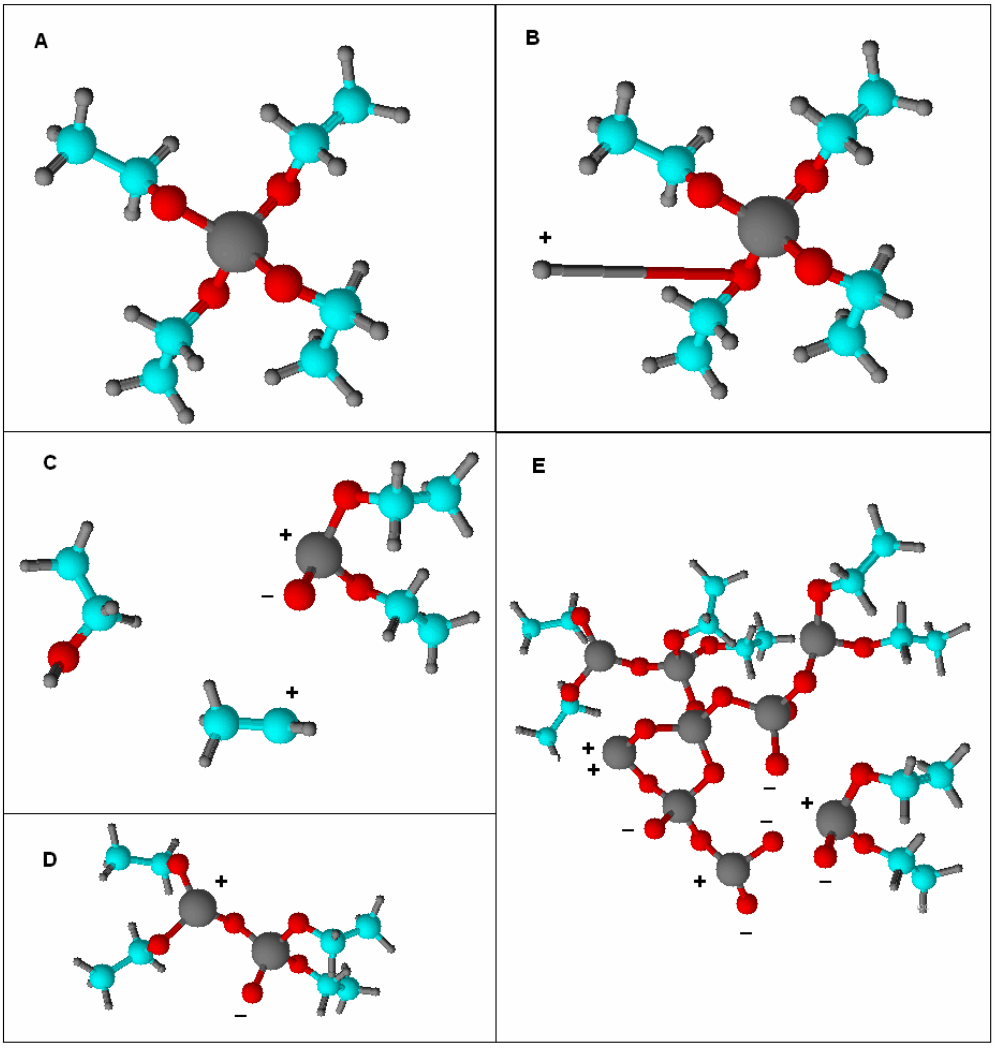

Figure 1.1 *The gelation of silica. Shown here: small pale grey – hydrogen, blue – carbon, red – oxygen, large silver - silion (A) TEOS a typical precursor for sol-gel synthesis is hydrolysed in acidic conditions. (B) a proton (hydrogen ion) interacts with one of the oxygens in the alkoxyl group through hydrogen bonding, This generates a distribution in charge across the TEOS molecule, weakening the Si-O and C-O bonds as electrons are drawn towards the region of positive charge. (C) The original bond is weakened sufficiently so an alcohol molecule is displaced, resulting in a silica network former and an alkyl radical. (D) the network formers begin to polymerise. (E) The charge centres on the silicon and oxygen atoms allow the formation of a gel network.*

Consequently, in alkaline conditions, it is the hydroxyl ion that plays the dominant role, and generates a charge current across the TEOS molecule in the opposite sense. This drives the hydroxyl ion to bond directly with the silicon atom, ejecting the alkoxyl ligand. The presence of the OH group on the silicon prevents polymerisation, resulting in the colloidal suspension of silicon tetrahydroxide nano-particles.

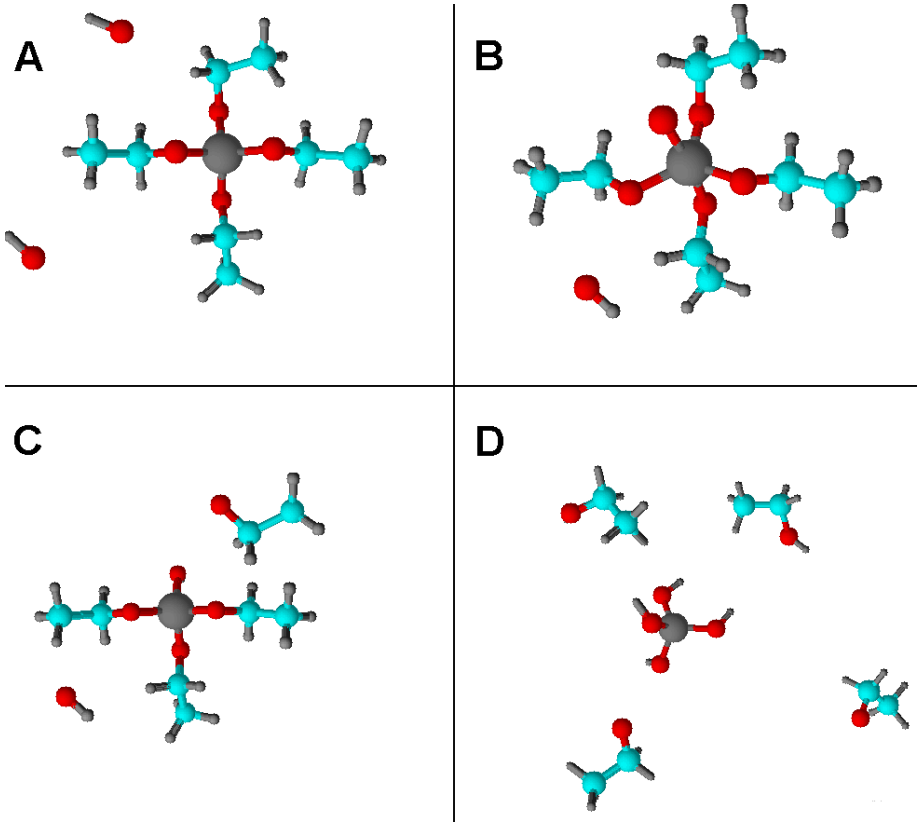

Figure 1.2 *The chemical reaction with hydroxyl ions. (A) TEOS in a strong alkaline solution first experiences a change current across the silicon atom, induced by the hydroxyl ions, which destabilises the alkoxide structure. (B). This leads to the ejection of alkyl ligands as the smaller, hydroxide state is more stable (C) and the formation of silicon hydroxide nanoparticles in an alcoholic medium (D)*

In conditions close to neutrality, silicon hydroxide agglomerates will occur with partial polymerisation, resulting in eventual precipitation if the particle agglomerates become too

large. The size and growth rate of these agglomerates will depend on the ratio of protons to hydroxyl ions. Such conditions can be adjusted to slow down particle growth and control their average size; making this a favourable technique in the production of nano-particles.

Extreme acidity can slow both polymerisation and precipitation by forcing the organo-silica moieties to remain in their charged molecular state. Excess protons can partially attach themselves to the negatively charged oxygen centres, thus preventing bonding with the positively charged silicon atoms in surrounding molecules. Too many protons can even stop gelation completely – leaving a clear sol; desirable for the dip coating process of thin silica layers.

In the vast majority of sol-gel processes, the reactions in both figure 1.1 and figure 1.2 will play a role in determining the appearance and property of the final gel, since hydroxyl ions will be present in even the most acid environments. This often results in large networks containing a suspension of smaller agglomerates. It is found that clear gel formation (in the optical region) is optimal at pH 3 [7], where all silica will be present in the gel network.

1.2 Transition metal gels

As well as silica sol-gels, other alkoxides are commonly used in sol-gel processing to produce a variety of novel glasses and ceramics. By conventional glass making methods, transition metal oxides possess higher melting points and glass transition temperatures

than conventional silicon dioxide. Sol-gel prepared transition metal ceramics and glasses have a much lower sintering temperature [17].

The chemistry of transition metal sol-gel reactions differs somewhat from silica [18,19]. Transition metals often have more than one valance state, which render them far more susceptible to hydrolysis reactions. Using methods employed in the production of silica-gels, reactions would occur through nucleophilic substitution of the alkoxyl ligand with a hydroxyl; with the remaining proton bonding with the alkoxyl to form alcohol. The reactions proceed too fast for polymerisation to occur, resulting in precipitation of transition metal hydroxides and oxo-hydroxides.

Transition metals are most stable in their highest valence state. Thus, to produce clear homogenous gels and sols, an additional compound must first be introduced to make the transition metal coordinatively saturated. Such compounds are known in sol-gel chemistry as chelating agents.

The most widely used chelating agent is acetylacetone [20, 21]. Acetic acid is also often co-employed for its additional properties as a proton donor. The chelating agent is added to the transition metal alkoxide, which react to form alkoxide-acetylacetonate complexes (see Figure 1.3), stabilising the transition metal to its highest coodination state.

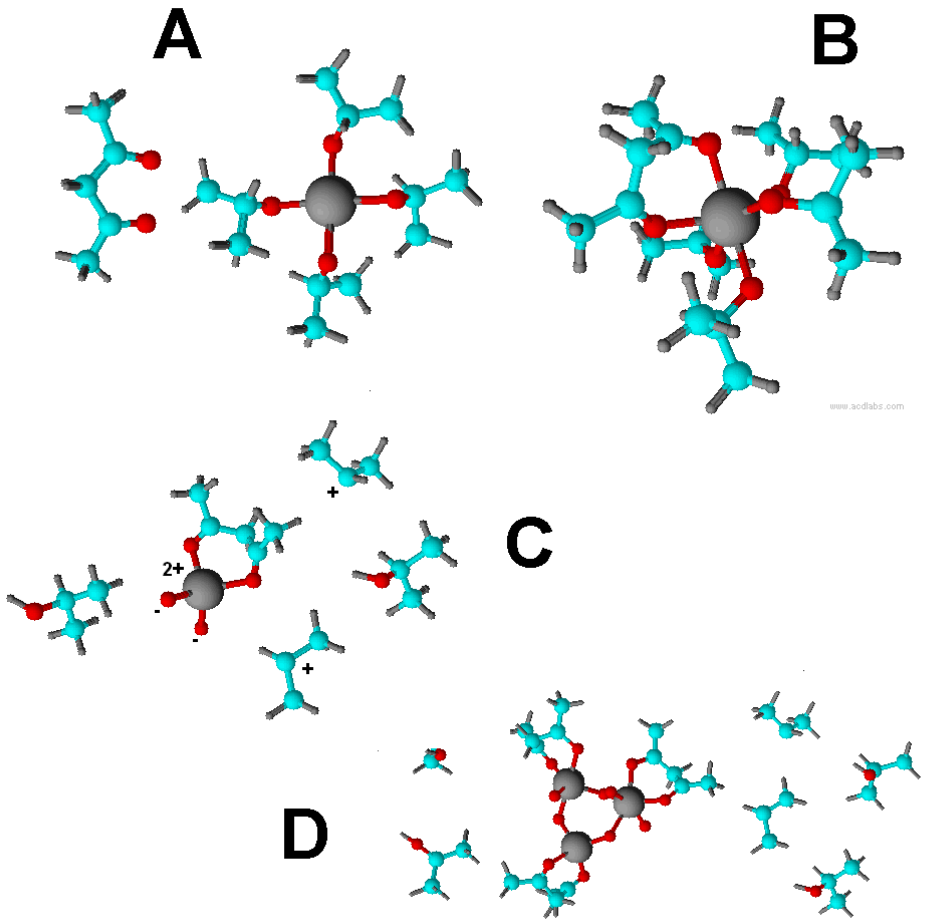

Figure 1.3: *The role of Acetylacetone in transition-metal sol gel reactions. (A) The acetylacetone and alkoxide begin to interact. The transition metal ion is in a 4-coordination state (A). The 2 oxygen atoms of the acetylacetone bond with the metallic ion to make a chellate ring, increasing the valence state of the ion to 6, and stabilising the metal to its highest valence state (B). The sol-gel reaction then proceeds as it would in the case of silica, resulting in network formers and alkyl radicals (C). A transition metal polymer begins to form (D).*

The result is highly dependent on the molar ratio of chelating agent to alkoxide used. For zirconia and titania, for instance, where acetylacetone is used, full coordinate saturation occurs when the molar ratio is greater than 1, which is desirable when only a liquid sol is required. On hydrolysis, the acetylacetoneate complexes remain in solution and cannot

polymerise into a gel, in much the same way an overly acidic environment prevents the polymerisation of silica sols. In addition, it is often prudent to dilute the water with a quantity of alcohol to slow the reaction further.

Conditions for gelation are optimal when the transition metal coordination is slightly under saturated. This way, not all the alkoxide has reacted to create a transition metal acetylacetonate and polymerisation can proceed as with silica sols. Decreasing the molar ratio acetylacetone:alkoxide further allows both agglomeration and polymerisation and results in more opaque gels.

To further complicate the process, the use of acetic acid can further prevent precipitation and also act to slow the polymerisation reactions. An overly acidic environment will again result in a clear sol where no polymerisation reactions occur. Calculating the chelating agent - alkoxide molar ratio must also include acetic acid due to its chelating properties. In the production of clear gels, a small quantity of acetic acid is always added at the time of chelating to provide additional protons which prevent precipitation. By comparison, the same recipe in the absence of acetic acid results in agglomeration.

The presence of so many compounds, each playing a major role in gel formation, means the reaction mechanisms for transition metal sol-gel processing is still poorly understood. Careful deduction of the molar ratios give a starting point in which, quite often, the desired product is obtained through a little trial and error. Such methods can be costly to industry, both in terms of man-power and materials expense.

1.3 Composite gels

So far, only single metal gels have been considered. In the vast majority of glasses and ceramics, more than one species is present. Sol-gel processing allows for the addition of dopant ions, which are added either before or during hydrolysis. The dopants can be added in two forms; alkoxides or acetylacetonates, or metallic salts such as nitrates and chlorides. Both of these have their own properties which must be taken into account during the sol-gel reaction.

Alkoxides of the more exotic metals, such as rare-earths, are often expensive and difficult to synthesise due to their extreme sensitivity to hydrolysis [22, 23, 24]. Small quantities can be made by alcoholisis of an anhydrous chloride: In the highly exothermic reaction, the chloride strips the proton from the oxygen atom in the alcohol to give hydrogen chloride. The alkoxyl ligand then bonds with the metal in the form of an alkoxide [25]. However, the quantity of hydrogen chloride gas, and the moisture sensitivity of the alkoxide make this an unattractive method for wide-scale production. Also, not all anhydrous chlorides react readily with alcohol, such as the case with yttrium III chloride. In these circumstances two solutions are prepared, and then mixed in a controlled environment. [7,23] The chloride is dissolved in alcohol, and mixed with a second alcoholic solution containing an alkali-metal alkoxide such as potassium propoxide.[24,25] The reaction proceeds with the formation of the desired alkoxide, and the precipitation of the alkali-metal chloride which is insoluble in alcohol. The alkoxide can then be siphoned off by centrifuge.

Once the dopant metal alkoxides are obtained, the alkoxides are combined, then chellated and hydrolysed in the usual manner. However, composites where one alkoxide is very much more reactive than the other can also lead to gel networks with agglomerates of the dopant material.

Where the alkoxides are too difficult or costly to produce, dopants can be added in an alternative form, usually as metal nitrates. [25] Though in principle the nitrates route is a safer alternative, the dopant percentage is limited by the solubility and pH of the nitrate. Most nitrates that are readily available also come in hydrated form, making them unpractical for addition to the alkoxide prior to hydrolysis. Nitrates also readily decompose on heating, which make the production of anhydrous nitrates a difficult task. Also, it is quite likely that not all the dopant ions will be incorporated into a gel network (if desirable).

The resultant sol-gel, and its structure, is very much dependent on the metals used. Silica-transition metal complexes where all metals have been added in the form of alkoxides, give a single silica-transition metal gel network - as in the case of zirconia-silica gels, which are sintered for use as a catalyst in the manufacture of high-octane in the petroleum industry. On the other hand, gels synthesised via the nitrates route will invariably consist of a principle gel network with the nitrate dopants remaining in solution, and hence contained within gel pores.

1.4 Alternative sol-gel routes

Due to the instability of many metallic alkoxides, attention has been given to searching an alternative method of producing nano-particles using non-alkoxide sol-gel routes.

The simplest method, sometimes used in the production of yttrium aluminium garnates and zinc oxide thin films with preferred orientation, is to mix solutions of metal nitrates with citric acid [19, 26, 27]. The citric acid forms complexes with the metallic ions, and gelation (if desired) can occur after heating for 12-24hours at 80 degrees Celsius. The sol or gel can be used for dip-coating, or dried to obtain nano-particles.

The obvious advantage in these routes is they allow for the precursor materials to be in an aqueous rather than alcoholic solution. There is less danger of undesired precipitation and agglomeration as the precursors are far less reactive than their alkoxide derivatives.

Alternative sol-gel routes can also be combined with the conventional alkoxide process to generate organo-metallic polymers involving transition and rare-earth metals. Citric acid can also replace acetylacetone and acetic acid as a chelating agent, particularly where rare-earth sol-gels are required, providing additional opportunities for the manufacture of more exotic systems - such as in the production of orientated zinc oxide thin films and quantum dots [29, 30].

1.5 Finishing – Drying and sintering

Once a gel has been made, it is necessary to further treat it to obtain the desired product. This treatment usually involves extracting the solvent to either preserve or densify the gel network and, if needed, sintering to give a ceramic or glass.

Solvent extraction by drying in open air results in a xerogel. Unless special chemical precursors have been used in addition to alcohol during the gelation stage, the gel itself will often crack and crumble as the network shrinks. Destruction of the gel network is increased if the solvent is allowed to evaporate too quickly; due to increased kinetic energy of the alcohol molecules trapped in pores destroying the surrounding walls of gel network [31]. Network destruction is not so important in the manufacture of dense ceramics, the process of which involves pressing into moulds and sintering at temperatures of 1000 degrees Celsius.[31] However glass formation requires the transparency of the network to remain intact. Gel cracking is also a major obstacle in the production of optical devices.

If the original undensified gel network is required, then solvents can be extracted by means of supercritical drying. In a typical synthesis, the wet gel is first washed with acetone, and then placed in a carbon dioxide chamber at a pressure of 72 atmospheres.[7,31] At such pressures, the barriers between liquid and gas become indistinguishable for carbon dioxide, and the supercritical fluid is able to penetrate gel pours and replace the solvent while at the same time preserving the network. Carbon

dioxide is favourable due to its relatively low supercritical limit at room temperature. The result is a porous, low density and highly insulating material known as an aerogel.

In addition to the above techniques, a viscous sol can be drawn into fibres or thin needles at the onset of gelation. This makes an attractive method for the manufacture of STM and SEM devices, which require needles with points of atomic thickness. The fragile gel needles can go on to become ceramic nano-fibres by sintering. Similarly, thin films are densified by drying and sintering using methods similar to those used in Xerogel production. Here, the dense film needs to appear at temperatures low enough not to melt or otherwise affect the underlying substrate. This makes sol-gel an attractive method in comparison to other techniques in thin-film production - such as sputtering and chemical vapour deposition; which require highly specialist equipment. In contrast, sol-gel can be deposited by either dip coating (a substrate is dipped into the sol, and the coating allowed to dry), or a substrate is coated using a spin-drying technique. Here, the substrate is spun at high velocity, and a droplet of sol is deposited in the centre. A thin coating is obtained as the sol spreads over the surfaces due to the centrifugal forces present during rotation.

Chapter 2

Sources of Synchrotron Radiation

When charged particles are accelerated by a magnetic field, they emit energy in the form of electromagnet radiation. The cause of this emission is more apparent from the reference frame of the charged particle. As it accelerates, the particle experiences a change in the magnetic field from the particle's own frame of reference. Schematically, this can be visualised by imagining a set of points spaced equally apart inside the field. As a particle accelerates and passes them, the time taken to travel from one point to the next decreases with increasing particle speed. In the reference frame of the particle, the magnetic field density appears to increase.

If the particle's velocity remains far below the speed of light (non-relativistic) - then emission occurs in the form of an isotropic dipole pattern, with the strongest emission taking place perpendicular to the acceleration vector. An example of this type of emission is in radio antennae, where electrons move back and forth along the length of the antenna and emit photons in the microwave and radio regime. In the most simple case, the length of the antenna is one quarter the wavelength of the electromagnetic radiation emitted.

As the motion of the charged particle becomes relativistic, emission is concentrated into the forward direction in the shape of a cone. This occurs due to light aberration and time dilation, which concentrates the emitted energy in the form of a beam relative to the observer. The radiation cone narrows as the velocity of the charged particle approaches

the speed of light. At these relativistic velocities, the electromagnetic radiation is linearly polarised in the centre of the beam-cone.

The existence of synchrotron radiation was first postulated nearly 100 years ago by theoretical physicists. They described the loss of energy in the form of electromagnetic radiation as electrons are accelerated in a magnetic field. The electromagnetic energy would be emitted along a path tangential to the election.[32,33,34]

It was not until after the Second World War, in 1947 that technological advancements allowed the construction of the first particle accelerators, and synchrotron radiation was detected for the first time [35,36]. During testing of a new 100MeV Betatron at Schenectady, New York, Blewitt and Livingstone observed radiation being emitted in the visible and infrared regions as the direction of motion of an electron was changed by a powerful magnetic field [37]. Since then, particle accelerators of ever increasing size have been built, many of which are designed specifically for harnessing synchrotron radiation.

2.1 The basic synchrotron

When electrons (or indeed any charged particles) are accelerated to velocities approaching the speed of light, the radiation is emitted in an increasingly narrow beam due to relativistic effects. The result is a highly collimated beam of light emitted in tangent to the electron path. The radiation will have a peak, critical wavelength

$$\lambda_c = \frac{4\pi}{3}\frac{E_0^3}{ecBE^2} \quad \ldots\ldots. (2.1)$$

Here, E_0 is the electron rest mass energy, e is the electron charge, c is the velocity of light, B is the magnetic field strength and E is the beam energy.

For synchrotron radiation sources the relation can then be simplified to, [16]

$$\lambda_c(nm) = \frac{1.864353}{B(T)E(GeV)^2} \quad \ldots\ldots \text{(2.2)}$$

Where E(GeV) is the electron beam energy, and B(T) is the magnetic field strength. In actual sources, λ_c, describes the peak of a Gaussian distribution of wavelength energies which usually span the ultraviolet to high energy X-ray regions. These energies make synchrotron radiation sources ideal for X-ray scattering experiments and EXAFS.

Figure 2.1 shows a schematic design of a typical synchrotron radiation facility. The electrons are initially fired into a booster ring with a linac (1). When the electrons reach sufficient energy, they are channelled into the main storage ring (2). Once inside the storage ring, the electrons are passed through a series of undulators or wigglers (3) and bending magnets (4). The magnets act to keep the electrons in a circular orbit, thereby allowing the emission of collimated beams of electromagnetic radiation. Beamlines are constructed tangential to the storage ring to harness the radiation for scientific experiments. As the beam enters the beamline, the beam itself is comprised of a broad range of energies, and is often referred to as the 'white beam'. This 'white' beam first passes through an optics hutch, (5) which selects the wavelength, or range of wavelengths used, before ending up in the main experimental area, (6).

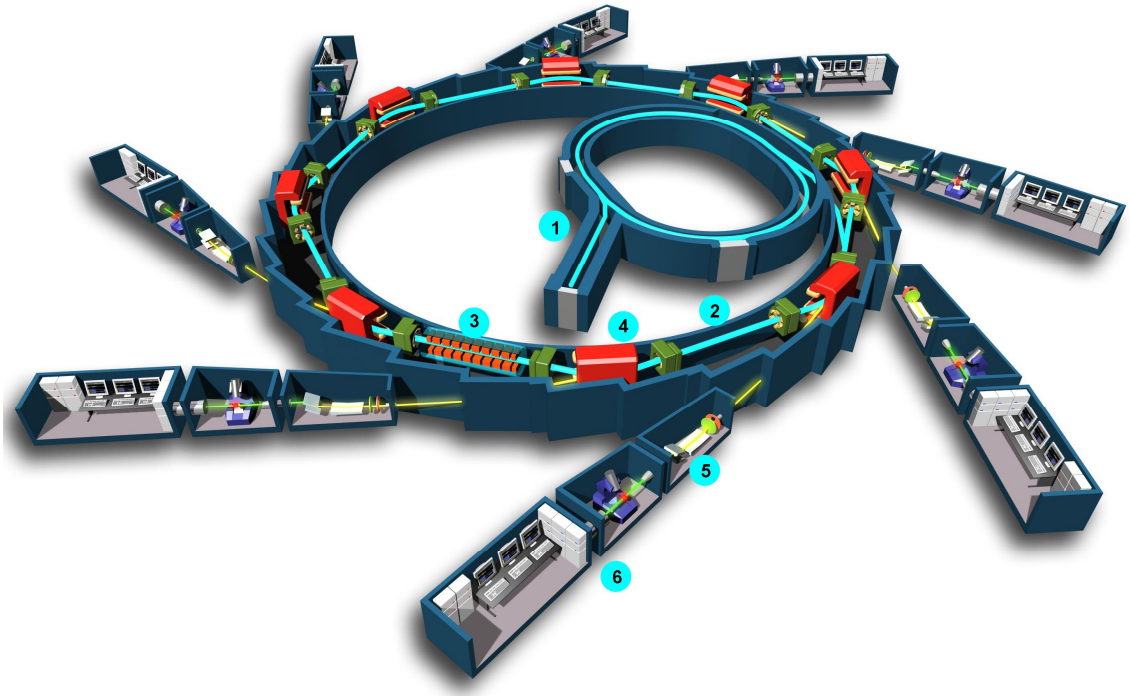

Figure 2.1*: A basic design of a synchrotron facility. 1: the linac and booster ring. 2: storage ring. 3: undulator or wiggler. 4 is the bending magnet for producing collimated beams of electromagnetic radiation. 5 and 6: the beamline where scientific investigations are carried out. (image courtesy French National Synchrotron Facility (Soleil)).*

In modern synchrotron facilities undulators are often installed.[38] An undulator comprises of a series of equidistant magnets through which the electron beam passes. The magnets force the beam to oscillate in a sinusoidal manner emitting radiation as it does so. Radiation produced from an undulator is of a much narrower energy band and much more intense than that produced by a conventional bending magnet. The undulator properties are governed by the dimensionless parameter given in equation 2.3.[16]

$$K = \frac{deB}{\pi m_e c} \quad \ldots\ldots (2.3)$$

The length scale, d, is the distance between the centres of two adjacent magnets of field strength B. e, m_e and c have their usual meanings as the electron charge, rest mass and velocity of light.

Figure 2.2 shows how an electron path is changed when passing through an undulator. Magnets of alternating field alignment cause the electrons to oscillate in the direction of the magnetic field (plane of the magnets) at wavelength $2d$, emitting linearly polarised radiation tangentially to the electron motion. Changing the parameter d will alter the value of K. For an undulator to produce beams across narrow energy band, K must be much less than 1. As K increases, the energy bandwidth also increases until a broad spectrum is obtained for $K>>1$. The resultant set up is then a wiggler rather than an undulator. [39] The typical spectra obtained from an undulator and a wiggler is represented in figure 2.3.

Modern facilities using undulators and wigglers are often referred to as third generation synchrotron sources. Before the advent of these devices, beams were channelled towards beamlines using bending magnets. These dedicated facilities are often termed second generation. Today, a good number of synchrotron facilities will have beamlines that are placed after an undulator or wiggler, or after a bending magnet. A prime example is Diamond Light Source, Oxford. Beamlines are numbered and given the prefix 'I' or 'B' depending on the device used to channel the beam. 'I' implies the beamline uses an insertion device, such as an undulator. 'B' indicates a bending magnet has been installed to channel the beam into the beamline area.

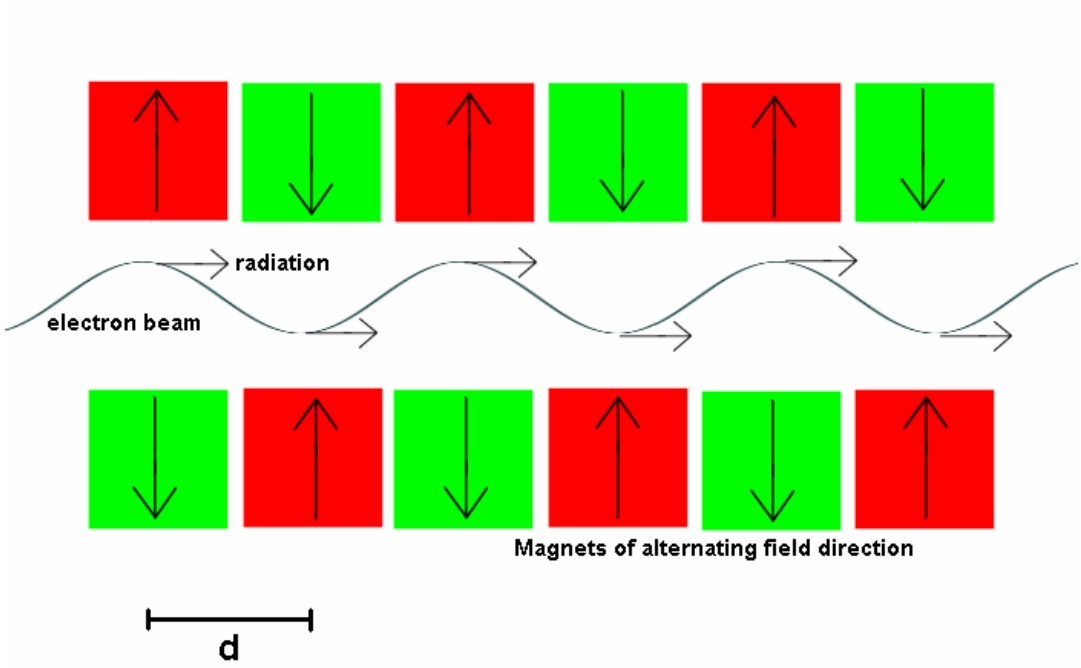

Figure 2.2. *The function of an undulator. Alternating magnetic fields of distance d apart cause the electron beam to oscillate at wavelength 2d, emitting electromagnetic radiation with a narrow energy band. The oscillation occurs in the plane of the magnets, so in this schematic, the electron beam oscillates vertically.*

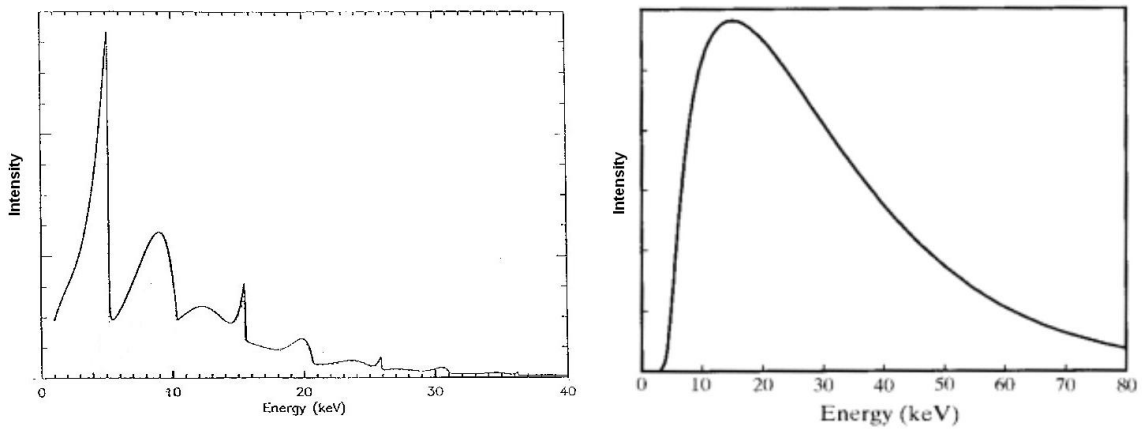

Figure 2.3: *Schematic representation of typical spectra from an undulator (left) and a wiggler (right) as energy vs Intensity (arbitrary units). An undulator has intensity concentrated into narrow bands, whereas a wiggler has a broader spectrum. The undulator can therefore give a greater photon count (intensity) for a given energy.*

2.2 The SAXS beamline

As previously mentioned, most small angle scattering experiments utilise X-ray energies of between 5keV and 20keV. After creation in the undulator, the photon beam enters the first part of the beamline where energies are selected by a monochromator. The resultant monochromatic beam is then focussed by a series of mirrors and slits before it is scattered by the sample. The scattering pattern is then observed with an X-ray detector.

A SAXS beamline will typically be composed of three sections, the optics hutch, the experimental hutch and a separate region for data collection.

2.2.1 The optics hutch

The first section the beam encounters after being produced by the bending magnets or undulator. As figure 2.4 shows, the beam first encounters an aperture and primary slit, which aim to provide an initial beam shape.

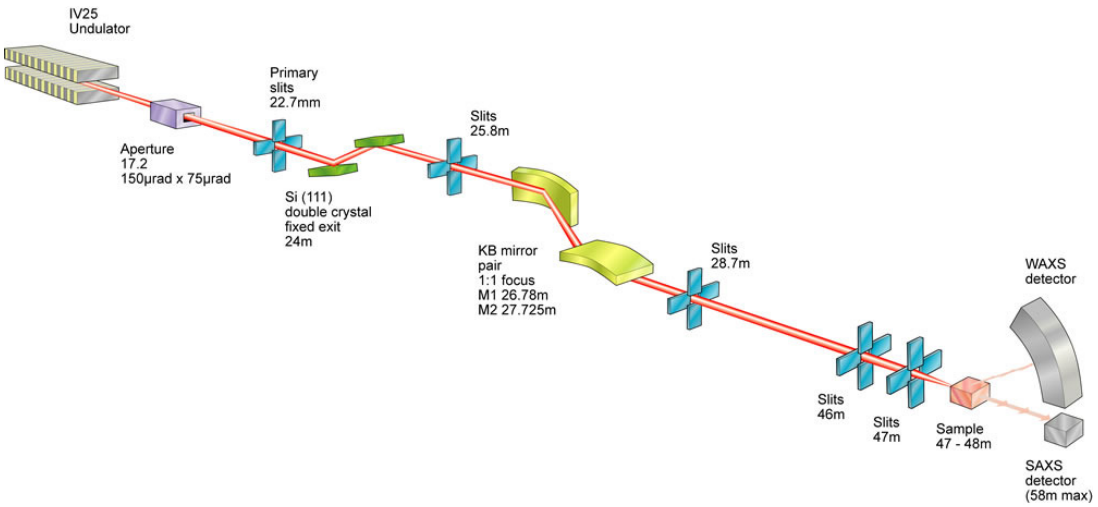

Figure 2.4*: Schematic of beamline I22 at Diamond Light Source, Oxford. (Image courtesy of Diamond Light Source Ltd)*

Once an initial profile has been shaped by the primary slits, the beam then enters a section of the optics hutch known as the monochromator. An X-ray monochromator typically consists of 2 ultra pure silicon crystals aligned to the Si (111) plane. The Si(111) has a 'd' spacing of 1.135 Angstroms, which serve to act as a diffraction grating to produce an angle dependent monochromatic beam in compliance with Bragg's law,

$$n\lambda = 2d\sin(\theta) \quad \ldots\ldots (2.4)$$

Thus by varying the angle of incidence of the crystal, different beam wavelengths can be filtered. In addition to the primary wavelength, additional energies from the 333 and 555 plane resonances will also be produced – their intensities depending on the energy profile of the original undulated beam. A Si(111) crystal monochromator will produce a monochromatic beam with an energy resolution, ($\Delta E/E$) of $1.2\text{x}10^{-4}$. [36,42]

Having passed through the monochromator, the beam is then further focussed by a series of slits and mirrors. The beam is reflected from a pair of Kirkpatrick-Baez (KB) mirrors at an angle less than the critical angle of the mirror material. In the case of beamline I22 at Diamond Light Source, Oxford,[40] the mirrors are coated with Rhodium, which has absorption edges of 23.2keV (K) and 3.4keV (L1), and sets an upper and lower limit on the potential X-ray photon energies that can be used in an experiment. With the beam now highly focussed, it is channelled through another array of slits before emerging from the beam-tube to be scattered by the sample. With KB mirrors, the beam width at the

sample is 320μm x 70μm. With additional micro-focussing, the beam width can be reduced to 2.7μm x 0.9μm.

Other beamlines, such as 7T-MPW SAXS at BESSY, Berlin,[41] have the option of removing the Kirkpatrick-Baez mirrors, so can technically allow the tuning of energies greater than 23keV. However, photon flux is significantly reduced at the higher energies and at energies lower than 4keV; and the resultant beam – which is shaped by only the slits, is less focused, particularly in the vertical direction, and so has much larger dimensions, typically of the order of 1mm in width.

2.2.2 The Experimental Hutch

This section of the beamline comprises of the end of the beamtube, the sample environment and detector system. Figures 2.5 and 2.6 show typical experimental set ups. Small angle scattering requires the high resolution detection of X-rays of angles less than 5°, and so are placed some distance away from the sample. There are a number of detectors available for SAXS. Typical examples include a 2 dimensional CCD, or a HOTSAX quadrant detector[42] – which are the two detectors used for experiments in this thesis. For scattering at angles less than 5° at a wavelength λ, and detector radius *h*, equation 2.4 can be inserted into a trigonometric relation to give,

$$l = \frac{h}{\tan\left[\sin^{-1}\left(\frac{q_{\max}\lambda}{4\pi}\right)\right]} \quad \ldots. 2.5$$

The value, q_{max}, is taken as the maximum value of q visible in the detector 'window'. The scattering vector q can be inverse transformed to give real-space length scale, setting the minimum length scale that can be probed for a given X-ray energy and sample-detector distance (l).

$$l = \frac{h}{\tan\left[\sin^{-1}\left(\frac{\lambda}{2d_{\min}}\right)\right]} \quad \ldots\ldots 2.6$$

Where d_{min} is the minimum length scale to be probed, and is equal to $2\pi/q_{max}$.

For a scattered photon energy of 12keV, a minimum length scale of 1nm (q_{mas}=*6.28nm*$^{-1}$), and a detector radius of 20cm, the detector needs to be placed at a distance of 4m from the sample.

Such distances require an additional vacuum tube to be placed between the sample and detector (*see figure 2.6*). A vacuum is required since X-rays are readily scattered by air, which would otherwise greatly reduce the scattered intensity. Typical pressure inside the camera tube is 100*m*Pa. The vacuum tube is extendible, which requires it to be constructed either of air tight units (I22, Diamond and 6.2 Daresbury), or from bellows (7T-MPW SAXS, BESSY). For the case of I22, Diamond, the air tight units (camera tubes) come in 0.5m and 1m lengths. The chamber is sealed both ends with kapton, which is transparent to X-rays.

For a more detailed view of experimental setups for SAXS beamlines, the reader is directed to chapter 5 of this thesis.

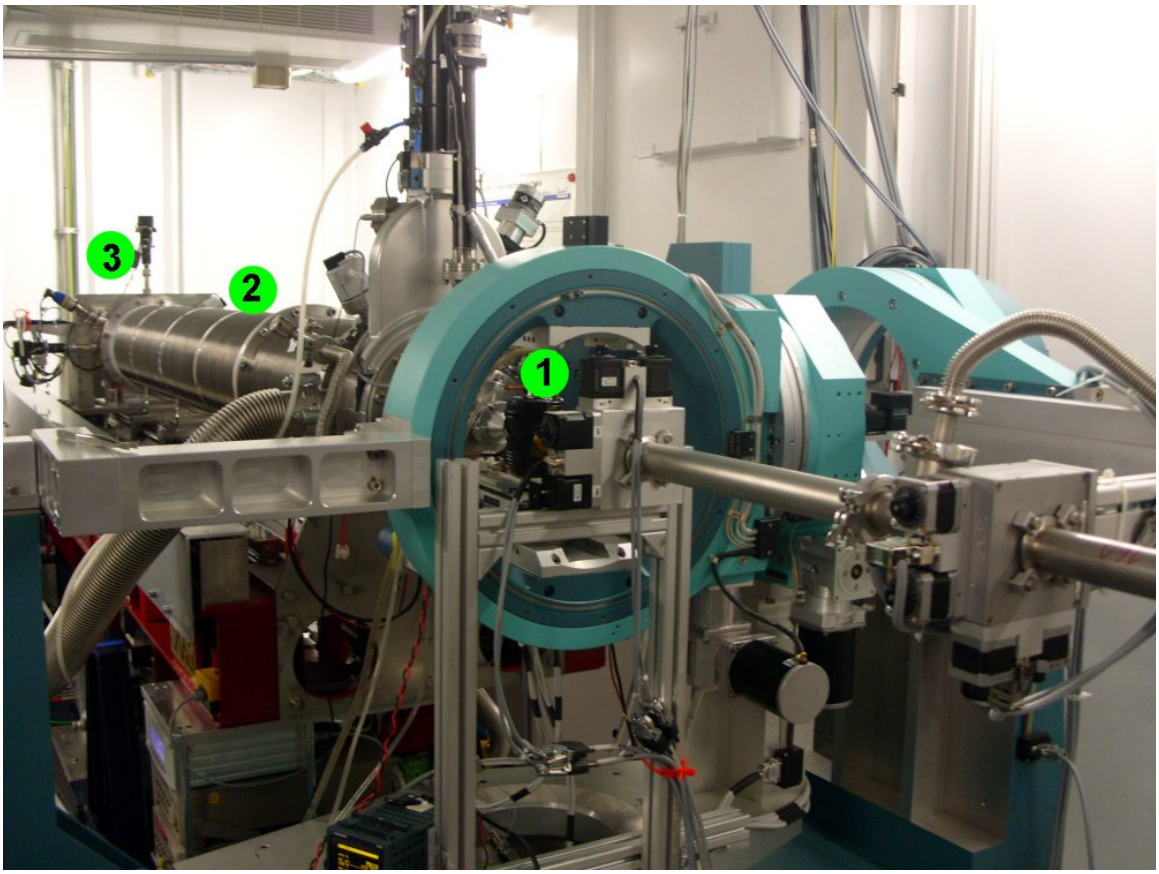

Figure 2.5, *A SAXS beamline. Shown here is a photo of beamline 7T-MPW at BESSY, Berlin. After exiting the beam-pipe, the monochromatic beam is scattered by the sample and sample environment (1). Scattered photons travel down a long vacuum chamber (2) before being read by the detector (3).*

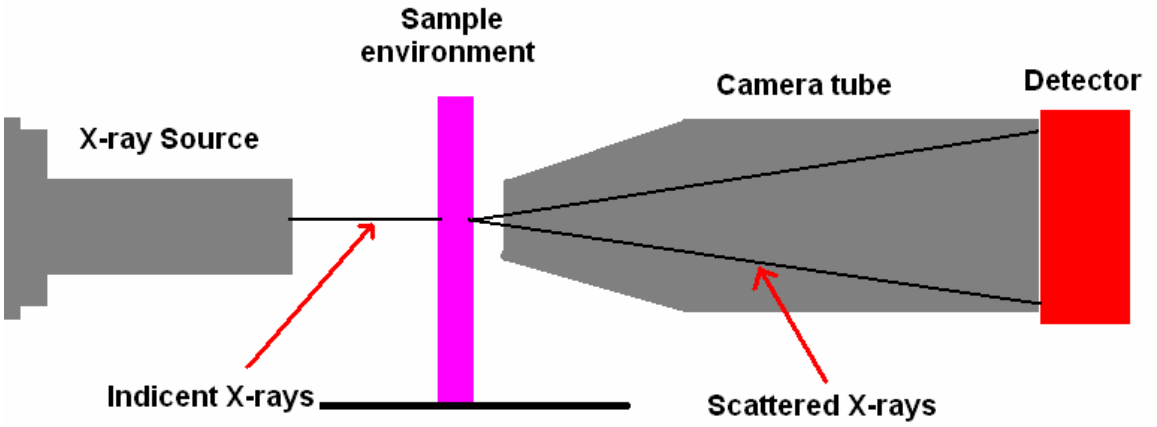

Figure 2.6: *Schematic of a beamline set up. Incident X-rays (emerging from the left) are scattered from the sample and sample environment. A detector (far right) is positioned some distance away. Scattered photons traverse this distance along an evacuated camera tube to preserve as much intensity as possible since X-rays are readily scattered by air.*

2.2.3 The Control Room

When an experiment is taking place, and scattered photons are being detected, the intensity and energy of the X-rays require the optics and experimental components to be in a lead room to prevent harmful radiation from escaping. Investigators therefore need an extra space, outside of the sealed environment, in which to collect data and work. In the case of I22 at Diamond, this is an extra closed room from which the beamline can be controlled remotely by computer. For 7T-MPW, the workspace is set in an open space just outside the beamline containment area.

2.3 An ideal ASAXS Beamline

Small angle X-ray Scattering beamlines have monochromators with tuneable energies, making them ideal for anomalous scattering experiments. Unlike SAXS, however,

additional factors need to be considered when accumulating data. Conventional SAXS would use a single energy set well away from any absorption edges of the sample. ASAXS requires a successive cycling of energies close to and at the edge of interest.

As energies go beyond the absorption edge, the sample will begin to fluoresce [36,57], and this fluorescence will be detected as part of the scattered signal. Fluorescence contributions need to be accurately measured and removed from the scattering data.

A much more realistic approach can be taken by using a separate point detector set at a wide angle, outside of any scattered signal, since fluorescence is generally distributed uniformly over all angles. The fluorescence detector would be calibrated against the beam intensity and scattering detector to obtain a value, which can then be subtracted from the accumulating data to deduce the scattering profile.

If the beamline has an additional wide-angle detector, then the intensities from the largest angles can be taken as a measure of fluorescence contributions.

Energy resolution from the monochromator can also pose a problem for the higher energies. Absorption edges tend to be fairly narrow, meaning there is a limited range over which energies can be cycled to give the greatest contrast. At the Niobium K edge at 19keV [36], for instance, the energy resolution from a Si(111) crystal is 2.28eV. This will result in a scattered signal that is the average for this energy resolution, which can smear contrast and reduce visible anomalous effects. Any chosen energy whose distance from the edge is less than the energy resolution will also give additional fluorescence contributions. It can be that in some materials, the absorption edge is so narrow that its width is less than the energy resolution of the monochromator.

Better resolution can be obtained by using a silicon crystal of higher order, such as a Si(311), and by using four crystals instead of two. Amongst the greatest resolution ever obtained was by *M. Yabashi et al*, in 2001. Using an array of four Si(11 5 3) crystals the team managed to get a resolution, $\Delta E/E$ of 8×10^{-9}.[42] The cost for such resolution is a much lower photon count in the monochromatic beam, which reduces time resolution for *in situ* experiments. For comparison, if the photon flux from a pair of Si(111) crystals is $10^{11} s^{-1}$, the flux from an array of four Si(11 5 3) crystal reflections is $10^{7} s^{-1}$.

Chapter 3

Small Angle Scattering

As a natural occurrence, small angle scattering of light can be seen everywhere. A ring can appear around the sun or moon. When the moon itself passes behind a thin, high altitude cloud, a glowing hazy disk appears. Such sights are caused by tiny particles of ice and water in the atmosphere which scatter visible light. If one was to measure the angular distance of the ring, or the intensity gradient of the glowing haze, information about the size and even the shape of these particles can be gathered. If the particles were close enough together, extra features may appear in the intensity map, providing additional information about the distances between the particles and how they interact.

Figure 3.1 *Small angle scattering of visible light occurs in nature. Shown here, a hazy disk around the moon is created from the scattering of tiny particles of water and ice in the atmosphere.*

Experimental observation of light scattering first began in the early nineteenth century, when Young and Fresnel observed scattering maxima and minima in the shadow space of a hair.[43,44,45] They deduced the patterns were caused by interference of waves from either side of the hair. Later, the findings of Young and Fresnel provided a template for Robert Maxwell to develop his famous Maxwell equations – a fundamental law in electromagnetism.[46]

With the discovery of X-rays in 1895, Sir William Lawrence Bragg first published his experiments on X-ray diffraction from crystals to the Cambridge Philosophical Society in 1912.[47] He showed peaks in diffraction patterns which were a measure of inter-atomic distances in reciprocal space. An inverse Fourier transform of these patterns would result in real-space distances from which information on crystal lattice structures could be obtained.

Though Sir William Bragg dealt mainly with larger angle scattering from crystals, it soon became apparent from his devised relations that at smaller angles, larger features could be measured. Guinier and Porod developed the first theories and experimental techniques in Small Angle X-ray Scattering in the 1930's.[48,49,50] They showed that at small angles, X-rays scatter at angles depending on the curvature of the particle; the smaller the curvature (and hence larger the particle) the smaller the scattering angle. The scattering angle would be zero on non-curved (flat) surfaces.

3.1 Small Angle Scattering Theory

Diffraction occurs due to interference of waves scattered by an object which, in the case of X-rays, are electrons. In this regime, electrons behave as if they were free since the X-ray energy is larger than the atomic binding energy. Scattered waves are also elastic at small angles, meaning that Compton scattering (inelastic scattering) can be neglected.

It has already been mentioned that small angle scattering occurs from particles with small curvature, and are very much larger than the scattered wavelength. X-rays typically have a wavelength of the order of an angstrom and will scatter at small angles in the presence of electron densities in the nano-meter length scales. This makes SAXS an ideal tool for exploring nano-structures such as colloids and proteins.

In the most simple of cases, a nano-structure such as a mono-disperse colloid can be considered to be an arrangement of spheres of radius, *r*, dispersed in a medium of different electron density to that of the colloidal particles. The scattering intensity *(I(q))* can be given by[52]:

$$I(q) = Nr_e^2 \Delta\rho^2 V^2 \left|F(q)\right|^2 S(q) \qquad (3.1)$$

Where *N* is the particle number density, Δρ is the difference in electron density between the primary particles and the surrounding medium, r_e is the classical electron radius, and V is the average particle volume. The term *F(q)* is the particle form factor, and contains information on the size and shape of the particle. *S(q)*, commonly termed the structure

factor, provides information on interactions between particles, and the distances between them. The momentum transfer, q, has units of inverse length *(r)*, and is given by,

$$q = \frac{4\pi \sin(\theta)}{\lambda} \qquad (3.2)$$

For the case of a simple colloid of spheres separated by a distance far greater than their diameters, the structure factor (S(q)) can be neglected, resulting in a scattering intensity that is related to the particle shape only. In the case of identical spheres of radius r and uniform density, the particle form factor has been calculated explicitly. [51]

$$F(q) = 3\left(\frac{\sin(qr) - qr\cos(qr)}{q^3 r^3}\right) \qquad (3.3)$$

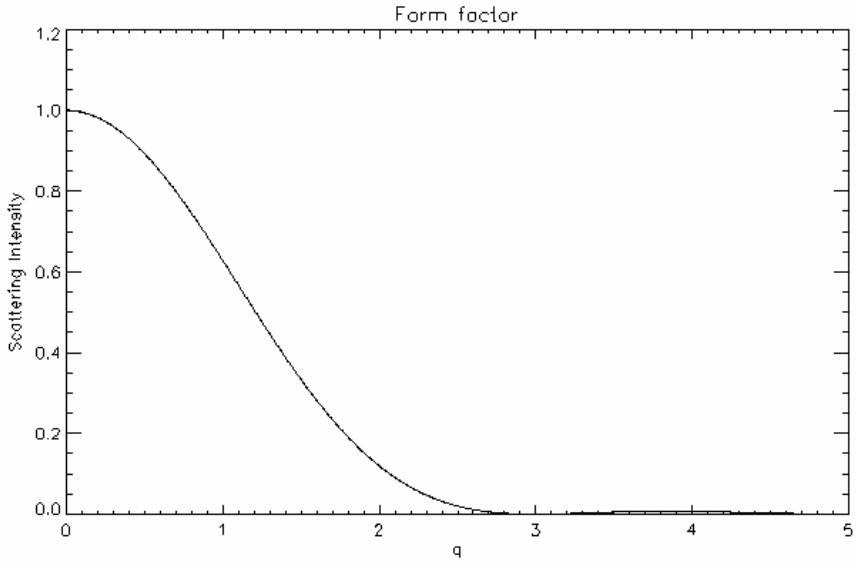

Figure 3.2: *The scattering intensity from a sphere, which is the square of the form factor (equation 3.3).*

Figure 3.2 shows the scattering intensity resulting from equation (3.3). Though a special case, the assumption already provides a greater insight into the colloidal structure. Taylor Expansion of the trigonometric terms

$$\sin(qr) = qr - \frac{(qr)^3}{3!} + \frac{(qr)^5}{5!} - \ldots$$

$$\cos(qr) = 1 - \frac{(qr)^2}{2!} + \frac{(qr)^4}{4!} - \ldots$$

And re-inserting into equation 3.3 gives,

$$F(q) \approx 3\frac{\left(\frac{(qr)^3}{3} - \frac{(qr)^5}{30}\right)}{(qr)^3}$$

$$\approx 1 - \frac{(qr)^2}{10} \quad \ldots\ldots (3.4)$$

The scattering intensity is proportional to the form factor squared, inserting equation 3.4 into equation 3.1 and assuming the spheres are far apart so the structure factor can be neglected, gives,

$$I(q) \approx N r_e^2 \Delta\rho^2 V^2 \left(1 - \frac{(qr)^2}{10}\right)^2$$

$$\approx Nr_e^2 \Delta\rho^2 V^2 \left(1 - \frac{(qr)^2}{5} + \frac{(qr)^4}{100}\right)$$

The $(qr)^4$ term is very much smaller than the others so can be dropped, this results in

$$I(q) \approx Nr_e^2 \Delta\rho^2 V^2 \exp\left[\frac{q^2 r^2}{5}\right] \quad \ldots\ldots (3.5)$$

As X-rays scatter from electrons, it is common practice to replace the particle radius with the radius of gyration R_g, which is effectively proportional to the root mean square distance between scatterers, and is given by the relation:

$$R_g = \frac{3r^2}{5} \quad \ldots.. (3.6)$$

From this it can be seen that by using this approximation, estimates of the particle radii can be measured from Gaussian fitting to the scattering intensity curve, or by a linear plot of *log Intensity versus* q^2. In small angle scattering, such analysis is known as the Guinier Radius – named after the scientist to first derive the relation.

An additional and valuable piece of information that is easily extracted from a scattering intensity is the Porod relation. From equation 3.3, it can be seen that as *qr* becomes large and approaches 2π, *sin(qr)* tends to zero and *cos(qr)* tends to one. Under these conditions,

$$F(q) \approx 3\left(\frac{-qr}{q^3 r^3}\right) \ldots\ldots (3.7)$$

Which, when squared for the scattering intensity gives,

$$I(q) \propto \frac{1}{q^4 r^4} \ldots.. (3.8)$$

This is an important result in small angle scattering. The Porod relation can be determined by measuring the gradient of a plot of *log I(q) versus log q.* In this case, a gradient of -4 implies a dispersion of smooth spheres.

The vast majority of materials analysed using small angle scattering do not consist of particles all of the same size and shape. This imposes additional complications in extracting information, so often some knowledge of the system being investigated is required before proper analysis can begin.

The following sections describe the scattering functions obtained from a number of simple objects such as disks, rods and ellipsoids. Following this, a further section describes theoretical scattering functions from fractal networks. Due to the similarities in Porod gradients for some of these systems – in particular between colloids (particle suspensions) and fractal networks – prior knowledge of what type of structure is being observed is essential in order to create an accurate model of a sample.

3.2 Scattering from non spherical particles

3.2.1 Ellipsoids of revolution

The scattering intensity (I(q)) for ellipsoids is given as[52]

$$I(q) = \int_0^{\frac{\pi}{2}} \Phi^2 \left(qr\sqrt{\cos^2\theta + v^2 \sin^2\theta} \right) \cos\theta d\theta \quad \text{..... (3.9)}$$

Where Φ^2 is the square of the spherical form factor given in equation 3.3, and v is the axis length factor given an ellipsoid of dimensions *2r, 2r, 2vr*.

Again, expansion of this equation results in a Guinier approximation similar to the result in equation 3.5, only the radius of gyration (Guinier radius) is

$$R_g = \frac{2r^2 + v^2}{5} \quad \text{..... (3.10)}$$

The Porod relation is effected by the additional *qr* in the integral. This is especially apparent with extreme ellipsoids where v>>r or v<<r. In such cases, the Porod relation is reduced to equation 3.11, giving a gradient of -3 for ellipsoids.

$$I(q) \propto \frac{1}{q^3 r^3} \quad \text{.... (3.11)}$$

3.2.2 Disk-shaped particles

The radius of gyration for cylinders of radius r and thickness H, is

$$R_g = \frac{r^2}{2} + \frac{H^2}{3} \quad \text{.... (3.12)}$$

Assuming negligible thickness, the particles can be considered to be two dimensional disk objects of radius r, and scattering intensity [52]

$$I(q) = \frac{2}{q^2 r^2}\left[1 - \frac{J_1(2qr)}{qr}\right] \quad \text{..... (3.13)}$$

Where $J_1(2qr)$ is a Bessel function. It can be seen that as qr becomes large, the first term begins to dominate as the second term shrinks to zero. At high q, the scattering intensity tends to

$$I(q) \propto \frac{1}{q^2 r^2} \quad \text{.... (3.14)}$$

Giving a gradient of -2 for disks.

3.2.3 Long rods of negligible radius

Assuming random orientation of long rods with a length, H, the scattering intensity becomes [52]

$$I(q) = \frac{Si(2qH)}{qH} - \frac{\sin^2(qH)}{q^2H^2} \quad \ldots. (3.15)$$

Where, $Si(2qH) = \int_0^{2qH} \frac{\sin(x)}{x} dx$ ….. (3.16)

As qr tends to infinity (ie, qr>>1), the integral converges towards $\frac{\pi}{2}$ and the squared terms reduce to zero. This leaves the Porod relation for long rods,

$$I(q) \propto \frac{1}{qH} \quad \ldots. (3.17)$$

A log-log plot of the scattering intensity will thus show a gradient of -1 at large q.

3.3 Rough Surfaces and the Fractal Model

So far, only smooth surfaces from 1, 2 and 3 dimensional particles have been considered. One might assume that it is sufficient to measure the Porod gradient in order to obtain the particle shape, from which a suitable fitting can be derived to extract the size distributions. The assumptions immediately break down when network and agglomerate forming materials such as sol-gel are analysed using SAXS.

As already discussed in chapter one, sols consist of primary particles which can bind together to form tree-like structures (gel networks), and larger particle agglomerates. Scattering profiles obtained from such networks exhibit Porod gradients of magnitudes less than four. In these cases, the Porod gradient can be used as a measure of surface roughness (on the nano-scale for X-ray scattering). The closer the gradient tends to four, the smoother and more spherical the scattering particles. Mathematically, such structures can be modelled as fractals. Where rough surfaces are known to be present, the Porod gradient provides information on the fractal dimension of the material.

Generally there are two types of structural fractals, each with their separate scattering functions at small angles. The surface fractal, which can be visualised as resembling a screwed up piece of paper, is described by [53]

$$I(q) = \frac{\pi(\Delta\rho)^2 S_2 l_2^{D-2} \Gamma(5-D) \sin\left(\frac{\pi(3-D)}{2}\right)}{(3-D) q^{6-D}} \quad \ldots\ldots (3.18)$$

Where S_2 is the smooth surface area of length scale l_s, and D is the fractal dimension. For a mass fractal, which is more tree-like in structure, the following function applies:

$$I(q) = NA(q)(\Delta\rho)^2 \left[1 + \frac{1}{(qr)^D} \frac{D\Gamma(D-1)}{1 + \left(\frac{1}{q^2\xi^2} \right)^{\frac{D-1}{2}}} \times \sin[D-1] \tan^{-1}(q\xi) \right] \quad \text{..... (3.19)}$$

The function A(q) is the square of the average form factor of the particles making up the fractal-like structure. In the case of sol-gel, these particles (termed primary particles) are the oxide and hydroxide monomers forming the network. The term ξ is the fractal correlation length – that is, the length scale of the 'fractal particles' in the material.

It is clear from both cases that the Porod exponent differs. For the surface and mass fractal respectively, where D is the fractal dimension.

$$I(q) \propto \frac{1}{q^{6-D}} \quad \text{... (3.20)}$$

$$I(q) \propto \frac{1}{q^{D}} \quad \text{.... (3.21)}$$

From the above relations, it is clear the only difference between them is surface fractals have *'6-D'* and mass fractals *'D'* in their power terms. The numerical differences in fractal dimension of surface and mass fractals may be slight if the fractal dimension, *D,* has a value close to 3. In general, surface fractals have a fractal dimension greater than 3 – this is evident from the screwed up paper model described earlier. A sphere is a three

dimensional body enclosed by a surface of area $A=4\pi r^2$. Visually, it is clear that a surface fractal has a surface area greater than A, whilst enclosing the same 'Volume', so the fractal dimension can be described as being greater than 3 in this case. Similarly, the same volume enclosed by a tree-like structure will have porous regions, so the actual volume of material comprising the fractal will be less than the volume of the sphere. For this reason, mass fractals generally have a dimension less than 3.

This subtle difference in fractal dimension (D) will generally give comparable Porod gradients if D is close to 3, so the slope of the high *q* region on a *log-log* plot itself cannot be used to determine the fractal type of the system. For this reason, especially where the fractal type is uncertain or not known, the gradient is taken as a measure of surface roughness, which is described in terms of a Porod exponent α; resulting in the relation given in equation 3.22.

$$I(q) \propto \frac{1}{q^{\alpha}} \quad \ldots. (3.22)$$

3.4 High Particle Concentrations

In systems comprising of high concentrations of scatterers, or randomly ordered close packed particles, the distance between particles becomes comparable to their diameters. Scattered rays will 'see' those spaces as regions of different electron density in much the same way X-ray photons 'see' the electron density of the individual particles, and so these regions will have an additional contribution to the scattering function. The scattering information from this contribution provides details of how the particles are

distributed within the sample, and how they interact. So it is possible to calculate the structure of the material. This contribution is described by the structure factor, *S(q)*.

In much the same way the Form factor depends on particle shape, the function of the structure factor differs depending on whether there is any ordered structures present, and the concentration of the particles in the surrounding medium. For the case of fluids with a large concentration of scatterers, the amplitude of the structure factor increases with concentration, and hence the closer the particles are to each other. In such fluids, the structure factor can be described in terms of a particle interference function of the form[48]

$$S(q) = \frac{V_P}{V_P - (2\pi)^{\frac{3}{2}} \varepsilon \beta(q)} \quad \ldots\ldots (3.23)$$

V_p is the volume offered to each particle, and ε is a constant which is generally considered to be unity. The function *β(q)* has the form

$$\beta(q) = \frac{2}{q\sqrt{\pi}} \int_0^\infty r(e^{-\frac{\Phi(r)}{kT}} - 1)\sin(qr)dr \quad \ldots (3.24)$$

Φ(r) is a potential energy function, k is the Boltzmann constant and T is the temperature of the sample.

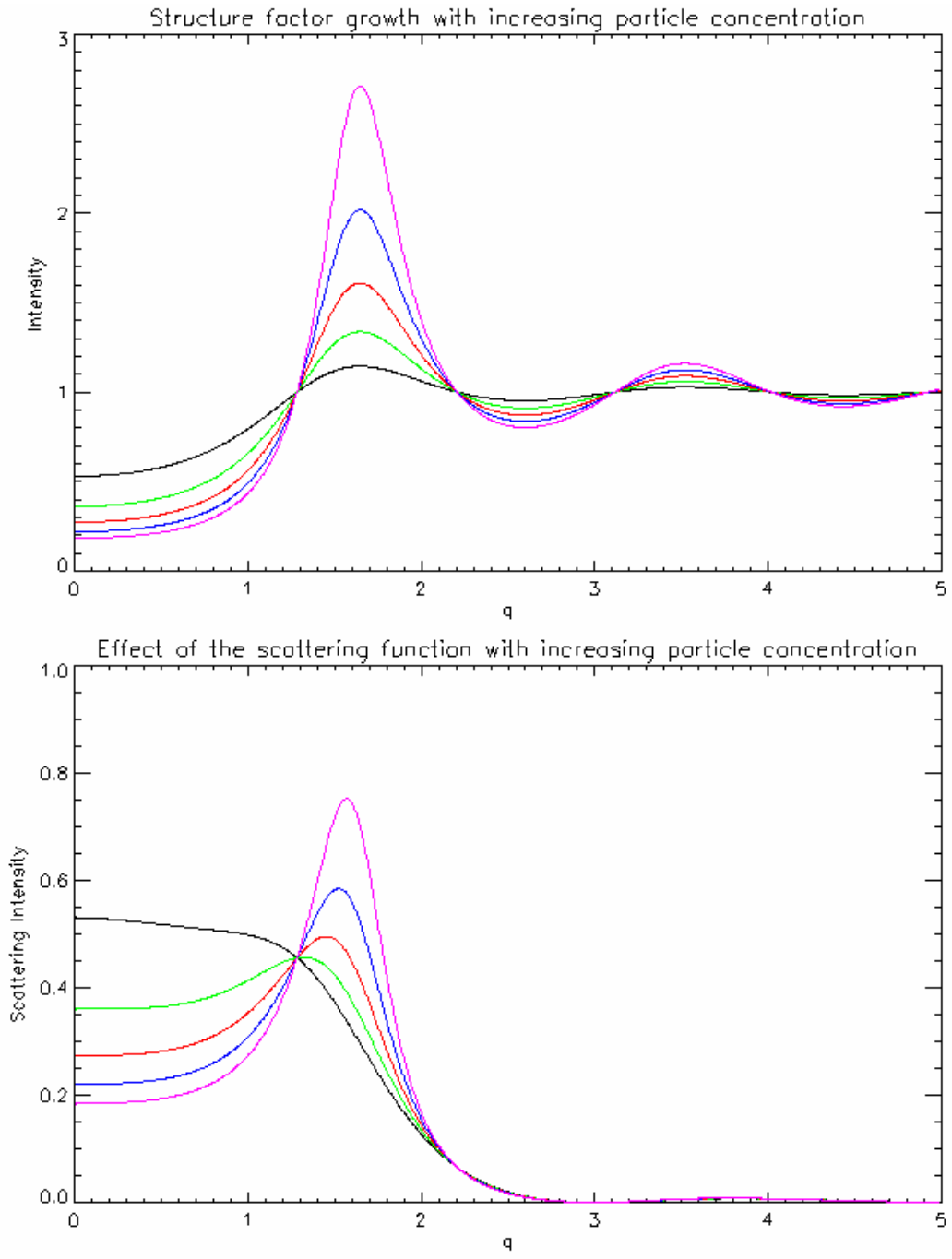

Figure 3.3: *Plot of structure factor and the effect on the scattering intensity profile for hard spheres, given in figure 3.2. For clarity, the temperature is taken to be constant. Top shows the structure factor of a system with increasing particle concentration. As the particle concentration is increased (and hence get closer together) the amplitude of the function increases. Bottom: the result of the scattering function for a distribution of hard spheres when the structure factors are applied.*

When the structure factor (equation 3.23), is inserted into equation 3.1, the resultant scattering function displays a Gaussian shaped 'hump' spanning a range of q. (see figure 3.3 bottom) The hump amplitude intensifies with increasing concentration.

As can be seen from the exponential in equation 3.24, this particular structure factor is also dependent on temperature. In the extreme cases, when T approaches 0 degrees Kelvin, the exponential also approaches zero, leaving the integral as a sinusoidal function which, when integrated over infinity, will also tend to zero. Thus, at very low temperatures, equation 3.24 will become small and the structure factor approaches unity. For high temperatures, where $kT>>\Phi(r)$, the exponential reduces to one, and equation 3.24 becomes proportional to the inverse of q. When applied to a scattering function, such a structure factor would have the greatest intensity contribution at very low q.

Chapter 4

Anomalous Small Angle Scattering (ASAXS)

4.1 The ASAXS Concept

X-ray scattering experiments are typically done with photon energies of between 5 and 20keV. Conventional SAXS does not take into account the effect these energies have on the individual atoms within a sample. It is possible to visualise atoms as comprised of a spherical volume of protons and neutrons surrounded by an orbiting cloud of electrons.

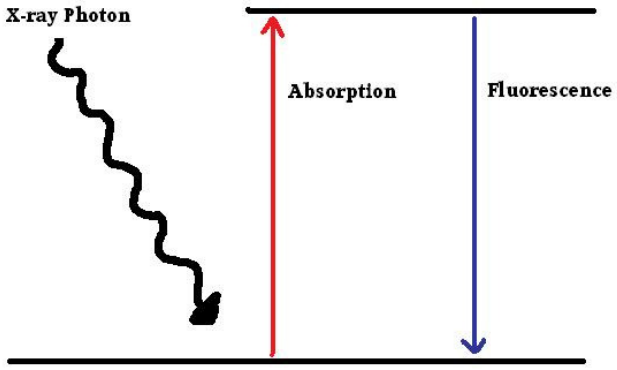

Figure 4.1: *Schematic of the absorption process. An incident photon excites an electron, sending the electron to a higher energy level. The energy is then released (as photons) giving fluorescence.*

Figure 4.1 shows a schematic of the absorption process. Quantum mechanics dictates these electrons to occupy certain energy levels, and if they are struck by a photon of at least matching energy, then the electron will absorb that photon, placing it in an excitation state, which - in the case where the original photon energy is greater than the

energy level - results in the electron emitting a second photon. This is referred to as X-ray absorption, with the electron energy level depicting the absorption edge for a given element.

It so happens that the X-ray photon energies are within range of many transition metal K, L and M absorption edges. These edges correspond to excitation states of the inner electron orbitals; the n=1, 2 and 3 levels respectively. The K-edges correspond to the orbital energy levels of the inner most electrons of an atom. Atoms with absorption edges in range of X-ray scattering experiments typically extend from titanium to molybenum. As the atomic proton number increases, so does the energy required to excite the inner electrons. For larger atoms, such as the rare earths and actinides, the photon energies are within range of their L and M edges. M edges begin to dominate for atomic proton numbers over 90.

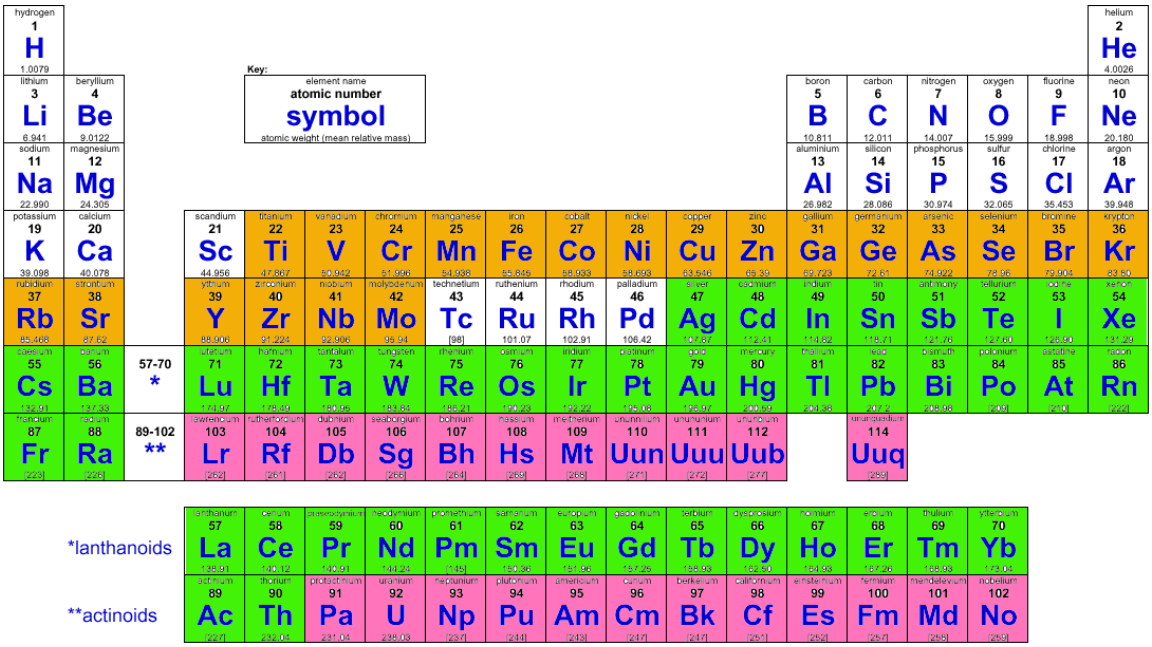

Figure 4.2: *atomic absorption edges within range of photon energies used in a typical X-ray scattering experiment. Orange, K edges, Green, L edges, Pink, M edges.*

The effect of this is that the absorption edge adds a complex correction to the atomic scattering function. The closer the X-ray energy is to the absorption edge, the larger this additional correction becomes.

In general, the correction to the scattering function is described as

$$f = (f_0 + f' + if'') \quad \ldots\ldots (4.1)$$

Since the scattered intensity is proportional to the square of the scattering function, equation 4.1 is multiplied with its complex conjugate to obtain [54]

$$I(q) = f_0^2 I_n(q) + 2 f_0 f' I_c(q) + \left(f'^2 + f''^2\right) I_r(q) \quad \ldots. (4.2)$$

The term f_0 is defined by the proton number of the absorbing atom. The additional two energy dependant terms, *f'* and *f''*, show *I(q)* is composed of three separate scattering intensities known collectively as the normal, cross and resonant terms. From equation 4.2 it is evident that in the event of no scattering correction contributions, the terms *f'* and *f''* become zero, leaving only the normal term multiplied by the square of the atomic proton number. Such approximation is valid when the X-ray energy is far below the absorption edge of the sample, and so is the 'ideal' scattering pattern obtained in the event of zero atomic absorption.

Corrections to the atomic scattering functions are derived from the Kramer-Kronig relations [55,56,57] given in equation 4.3

$$f'(E) = \frac{2}{\pi}\int_0^{\infty} \frac{Ef''(E)dE}{E_0^2 - E^2} \quad \ldots (4.3)$$

With E_0 being the energy of the X-ray photon and *f''(E)* being determined from the sample absorption spectrum, which is essentially a 'step' function at the absorption edge. Figure 4.3 shows the theoretical values of *f'* and *f''* for the element zirconium. The shapes of the functions are typical for all elements (and hence all absorption edges). Far below the edge, the values are close to zero, but as X-ray energies come within range of the absorption edge, *f'* begins to approach a minimum (and therefore increase in magnitude) towards a singularity on the exact point of the absorption edge. The position of the edge, in terms of absorption energy, is unique for each element.

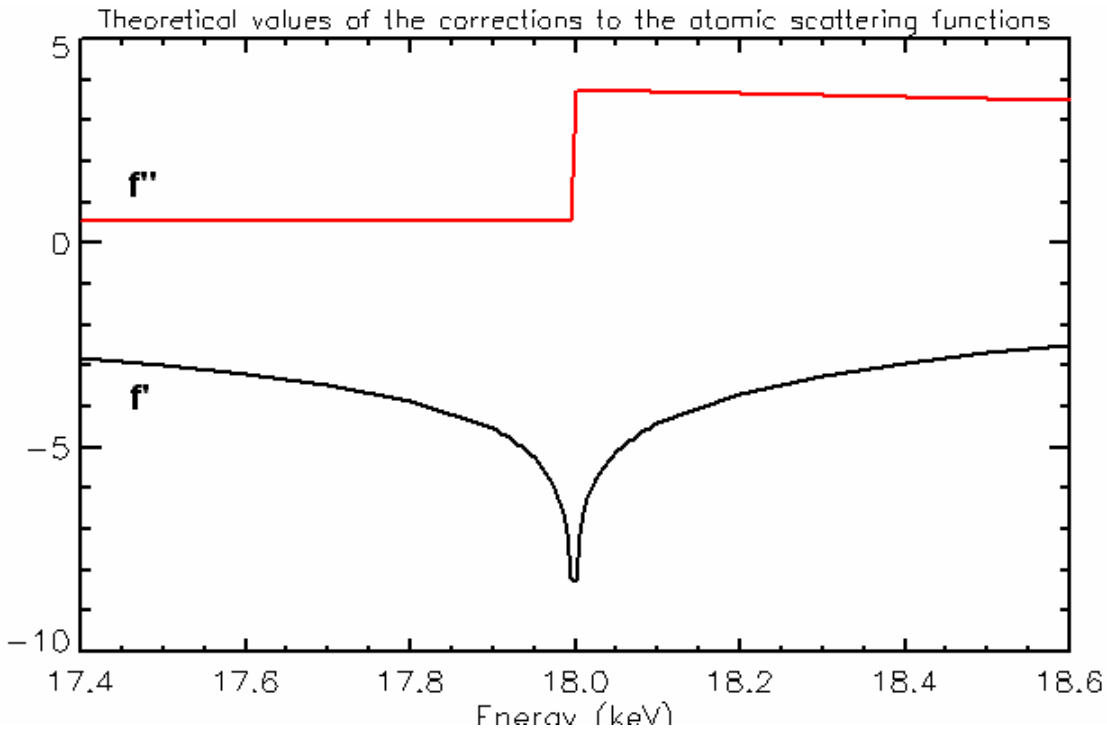

Figure 4.3: *Theoretical 'ideal' values for Zirconia of the corrections to the atomic scattering functions as calculated using the Kramer-Kronig relation.*[57] *The values of f' intensify close to the absorption edge (at 18keV). Such patterns are typical for all elements, though the position of the absorption edge is unique for each.*

By placing this trend into equation 4.2, it becomes apparent that the terms $I_c(q)$ and $I_r(q)$ will have a greater contribution close to the absorption edge. $I_r(q)$, the resonant term, which is dependent on the square of both terms will show the most significant change. The resonant term thus describes the scattering function of the absorbers in the sample. From equation 4.2 and figure 4.3, it is clear the cross term is dominated by the atomic proton number and a negative *f'*. As one draws closer to the edge, the magnitude of this negativity increases as the resonant scatterers become more absorbing, and hence reducing the overall intensity of $I(q)$. In general, the cross term provides information on the scattering function of 'unlike' particles – that is, the interaction between the resonant

scatterers and the remaining sample. An increasingly negative pre-factor also forces the cross term to become a negative scattering function which acts to reduce the intensity of *I(q)* – thus, the term can also be used as a measure of absorption over *q* space.

The ability to extract three partial scattering functions make ASAXS an ideal tool for examining composite materials.

4.2 Techniques in Anomalous Scattering

With a scattering contrast which changes as X-ray energies approach an absorption edge, a number of different approaches can be taken in performing a successful ASAXS experiment. Modern synchrotron sources also provide the additional advantage of higher beam intensities over a range of energies, allowing ASAXS experiments to be done *in-situ* where chemical properties change over time.

There are three distinct approaches that can be taken in an experiment, each with their own unique advantages.

4.2.1 Comparing two scattering functions taken far below and above the absorption edge

This technique, which is the simplest type of ASAXS experiment to perform on a beamline [58], relies on the value *f'* being relatively constant, and *f''* to exhibit variability; avoiding the often narrow edge region completely. As the resonant scatterers are

absorbing just above the edge, the resultant scattering function is the profile of the remaining sample.

The scattering function taken above the edge is then subtracted from the SAXS pattern obtained far below, resulting in the scattering contribution from the resonant particles, together with a contribution from the cross term.

In principle such an experiment should be fairly straightforward, however once energies pass the absorption edge, the resonant material begins to exhibit fluorescence as excited electrons release photons of differing energies. Often the fluorescence contribution is hard to deduce, particularly when the particles surrounding the absorbers have a much lower scattering intensity. Current 2d X-ray detectors are also non-energy discriminating, meaning they will count X-ray photons regardless of their incident energy.

The excited, fluorescing electrons will emit photons uniformly over all angles. To account for the fluorescence contribution, it is necessary to place an addition detector at a very wide angle where no scattering occurs. This additional detector can be calibrated with the main detector and incident beam to obtain a value for the fluorescence.

Though simple in principle, the fluorescence contribution can be very large if there is a high percentage of absorbing particles, or when the proton-number of the absorbers is much larger than the others. This has the effect of drowning out the often weaker signal from the non-resonant scatterers.

4.2.2 Multiple scattering intensities taken at a range of energies across the absorption edge

Perhaps the most widely used technique in ASAXS, this method offers a succession of scattering intensities at set intervals across an absorption edge. [59,60,61,62] Comparisons can be made to see changes in various regions of *q*-space as a function of energy. Fluorescence also does not become a major contributing factor so long as all the photon energies are kept below the singularity in *f'*.

The employment of this method can only be used for a comparative analysis. Information on the scattering profiles of the resonant scatterers can only be obtained with knowledge of the values for the complex corrections *f'* and *f''*.

4.2.3 The ASAXS Deconvolution Method

If the values for the atomic scattering corrections are known, or can be measured, then the most accurate and informative method in ASAXS is to solve equation 4.2 for the normal, cross and resonant terms. For this to work, 3 scattering profiles, *I(q)*, need to be measured at different energies, and hence different values of *f'* and *f''*, which can be solved as a simultaneous equation.

Figure 4.4 shows a typical choice of energies for an ASAXS experiment that utilises the deconvolution method. The two taken just below the *f'* singularity serve to provide the greatest possible contrast for the complex corrections. A third, taken far below the edge, has minimal values of *f'* and *f''*. [63,64]

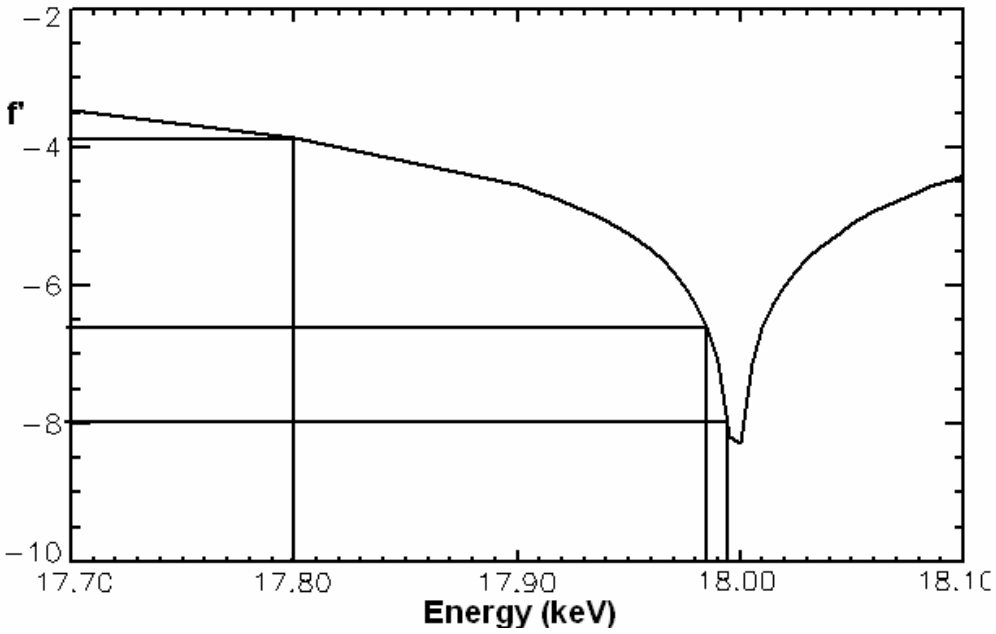

Figure 4.4 *ASAXS using the deconvolution method, showing the typical energy choices along the profile of f'. The energies are chosen to provide the greatest contrast between scattering intensities, whilst remaining below the singularity. Shown here are the energies an investigator may choose if performing ASAXS over the zirconium K-edge.*

The corrections themselves are measured by means of an X-ray absorption spectrum – often referred to as the Extended X-ray Absorption Fine Structure (EXAFS) by ASAXS communities, which is taken in conjunction with the three scattering profiles, and appears in the form of a step function similar to *f''*. The Absorption spectrum is the subject of the next section.

4.2.3.1 The X-ray Absorption Spectrum

Figure 4.5 shows the absorption spectrum for a sample of yttria stabilised zirconia, spanning the absorption edges of both yttria and zirconia.

An X-ray absorption spectrum is taken by measuring the incident and transmitted beam intensities just before and after passing through the sample. In an ideal situation, the absorption spectrum would cover all energies – however, since beamline constraints make this impossible (such as limits set by monochromator resolution and KB mirrors), it is sufficient to measure the spectrum over the absorption edge being investigated. High resolution spectra spanning all energies (attainable by the beamline) are often referred to as Extended X-ray Absorption Fine Structure (EXAFS for short).

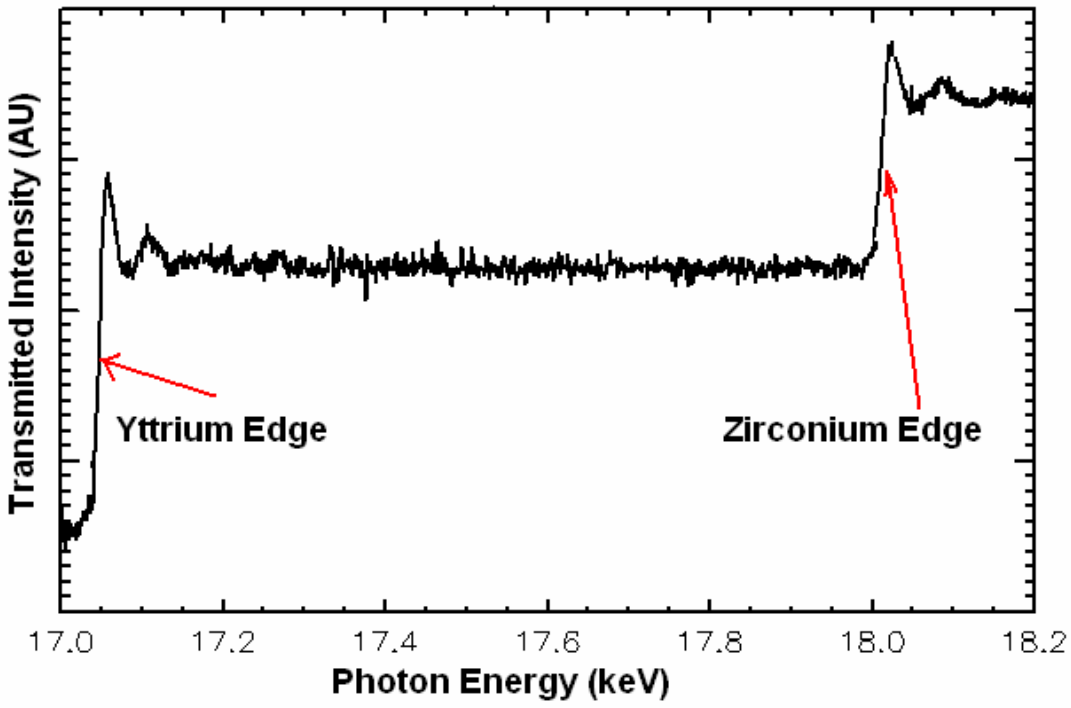

Figure 4.5: *An X-ray absorption spectrum (taken at beamline 6.2, SRS Daresbury). The sample shown here is yttria stabilised zirconia. The absorption edges (here, yttrium and zirconium) are highlighted by the step functions shown.*

The EXAFS spectrum taken over a wide range of X-ray energies, provides a diagram of excitation states for electrons within a sample – giving chemical and structural information. In the scope of ASAXS, only the region close to the absorption edge of the resonant scatterers is taken since the absorption spectrum is used to derive the corrections to the atomic scattering factors. In the scope of this thesis, the EXAFS spectrum is taken as the absorption spectrum close the absorption edge.

The absorption spectrum can be integrated using equation 4.3. Or alternatively if only the position of the singularity and approximate width of the resonance is required, the function obtained from EXAFS can be differentiated, and the result can be used as a reference plot for choosing suitable energies for the experiment.

4.3 ASAXS across multiple absorption edges

Many composite materials of interest contain more than two elements, some of which will also be in range of X-ray photon energies available at most synchrotron sources. In such cases, multiple edge ASAXS experiments can give the resonant terms for each edge element.

In the case of double ASAXS, equation 4.1 can be expanded to include the scattering contributions for each edge element.

$$f = (f_{01} + f_1' + if_1'' + f_{02} + f_2' + f_2'') \ldots\ldots (4.4)$$

Squaring equation 4.4, and taking the real parts, gives three components which can be compared to equation 4.2.

$$I(q) = f_{01}^2 I_n(q) + 2f_{01}f_1' I_{c1}(q) + \left(f_1^{\prime 2} + f_1^{\prime\prime 2}\right) I_{r1}(q)$$
$$+ 2\left[f_{01}f_{02} I_n(q) + \left(f_{01}f_{02}' + f_{02}f_{01}'\right) I_{c(1,2)}(q) + \left(f_1' f_2' + f_1'' f_2''\right) I_{r(1,2)}(q)\right] \quad \ldots\ldots (4.5)$$
$$+ f_{02}^2 I_n(q) + 2f_{02}f_2' I_{c2}(q) + \left(f_2^{\prime 2} + f_2^{\prime\prime 2}\right) I_{r2}(q)$$

The additional correlation terms in equation 4.5, provides scattering information on the interactions between the two edge elements under investigation. Expanded for a general formula of n number of edges, the additional terms give a matrix form of equation 4.2, of dimensions *n*x*m* where *n*=*m*.

$$I(q) = \sum_n \sum_m f_{0(n,m)}^2 I_x(q) + \left(f_{0n}f_{0m}' + f_{0m}f_{0n}'\right) I_{c(n,m)}(q) + \left(f_n' f_m'' + f_m' f_n''\right) I_{r(n,m)}(q) \ \ldots (4.6)$$

Equation 4.6 shows that the number of SAXS patterns that have to be taken per cycle increases as 3^n, reducing time resolution drastically with in-situ measurements, especially in ASAXS experiments with three or more edges. However, this is also an ideal situation. The scattering correction terms, *f'* and *f''* are the contributions for each edge element. Experimentally, it is not possible to extract these partial contributions from an X-ray absorption scan with the required accuracy. This simplifies equation 4.6 so that:

$$f'(E) = \sum_n f'_n(E) \quad \ldots\ldots (4.7)$$

$$f''(E) = \sum_n f''_n(E) \quad \ldots\ldots (4.8)$$

Therefore eliminating the additional cross correlation terms pertaining to the interaction between different edge scatterers, giving:

$$I(q) = \sum_n f_{0n}^2 I_x(q) + 2 f_{0n} f' I_{cn}(q) + \left(f'^2 + f''^2\right) I_{rn}(q) \quad \ldots\ldots (4.9)$$

Multiple edge ASAXS can then be considered to be a series of single edge ASAXS experiments cycled over each absorption edge of interest. This lessens the quantity of SAXS scans needed for full deconvolution to *3n*.

Time resolution can be further increased by considering the normal term to be the ideal SAXS pattern obtained in a zero absorption environment. The function will be identical for each deconvoluted edge. Provided the edges are close so the *q*-ranges do not change too significantly, one pattern may be taken below all edges, with just two per edge of interest. That is, *1+2n* SAXS frames per ASAXS cycle.

Chapter 5

Experimental Methods

Three sol-gel systems are analysed and presented in this thesis: Yttria stablised zirconia (YSZ) and YSZ in a silica matrix; where the whole process from gelation to calcination is studied. The gelation of zinc-silica sols is also investigated. Time resolved (double) ASAXS of YSZ and YSZ in silica experiments across two absorption edges were conducted at beamline 6.1, SRS Daresbury. Single edge time resolved ASAXS of Zinc-silica gelation was investigated using beamline I22, Diamond Light Source.

Sol gel preparation, be it in situ or ex situ, requires the controlled hydrolysis of alkoxide precursor materials that are often doped with metal nitrates or acetates. For the analysis of their bulk properties, the sols were prepared in such a way as to allow gelation over a time period of 3-5 hours, which allows a proper time resolved study of the reaction mechanisms. For calcination studies, the bulk gels were dried before placing in a furnace so the residual volatiles such as alcohols could evaporate.

5.1 Sol-gels

5.1.1 Zirconia Sol gel

Zirconia sols are prepared for comparative analysis, and for the preparation of YSZ, which follow the same methodology. The recipes and detailed preparation methods are provided below.

12ml 70%wt Zirconium n-propoxide solution was mixed with 6ml Isopropanol and stirred in an airtight container. 2.25ml of Acetylacetone (Acac) was then added as a chelating agent, together with 0.1ml glacial acetic acid. The volumes were chosen so that the molar ratio or Zirconium to Acetylacetone was close to 1:1, and the pH of the precursor solution was 3.

In a separate vessel, 2ml distilled water was added to 3ml isopropanol. The mixture was then stirred into the zirconium n-propoxide solution, sealed and kept at a constant temperature of 50 degrees Celsius. Gelation occurred after 3 hours.

Figure 5.1 shows the sample environment used to study gelation reactions *in situ*. With time resolved ASAXS, the zirconia n-propoxide, acac and acetic acid solution was poured into the main vessel. A water/isopropanol mix was introduced by remote injection by syringe. The force of injection and shape of the sample container ensured proper mixing occurred through fluid flow. The sample was kept at a constant 50°C throughout the investigation.

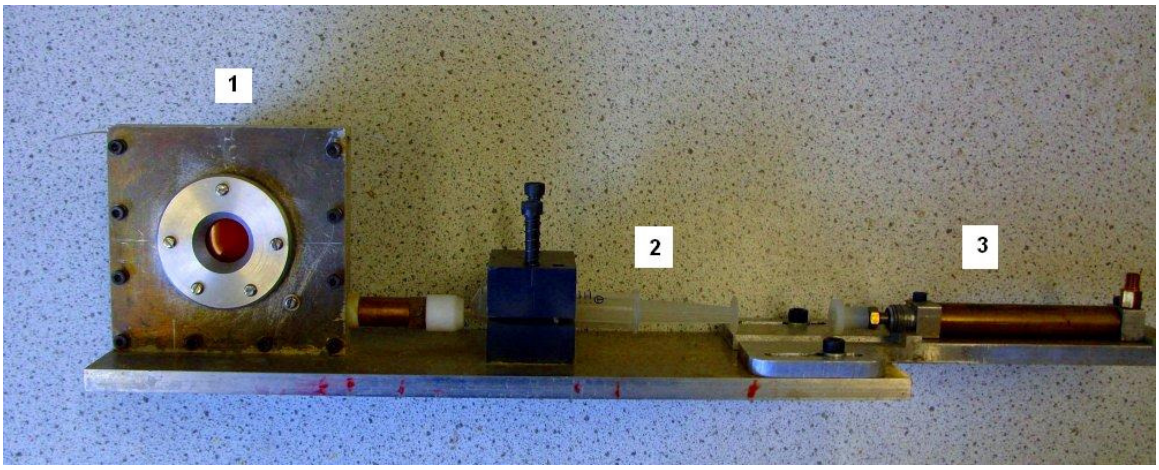

Figure 5.1 *The sample environment used for time resolved ASAXS studies of the gelation process. The precursor materials are placed inside the main gelation cell (1), and a second mixture containing water and alcohol is drawn into a syringe (2). Gelation reactions are induced by injection of the alcohol-water mixture into the alkoxide precursors by means of a remote syringe pump (3).*

5.1.2 YSZ sol gels

Yttrium isopropoxide solution was prepared by dissolving 1.5g anhydrous yttrium (III) chloride in 25ml isopropanol (IPA) in a dry nitrogen atmosphere. An additional 25ml isopropanol was reacted with 1.46g clean potassium metal. The environment was kept oxygen free in a glove box with a nitrogen atmosphere to prevent oxidation of the potassium alkoxide precursor. Emitted hydrogen gas was allowed to escape under controlled conditions in a fume cupboard.

The potassium isopropoxide and alcoholic yttrium (III) chloride solutions were then mixed and vigorously stirred under reflux at 80°C for 3 h. The potassium chloride precipitate was removed by placing the sealed containers in a centrifuge set at 3000 rpm, a clear solution of yttrium isopropoxide was siphoned off into a clean, air tight, dark glass container in a dry nitrogen atmosphere to preserve the compound for future use.

As shown by table 5.1, yttria stabilised zirconia samples were prepared using a variety of yttria-zirconia molar ratios. The sol gels were prepared in much the same way as pure zirconia gels, only the yttrium isopropoxide was added to the zirconia precursor solution before hydrolysis.

Sol 1 (ml)							Sol 2 (ml)	
Zr prop	**Y prop**	**TEOS**	**Acetylacetone**	**Acetic**	**IPA**	**Mol%Y/Zr**	**IPA**	**Water**
12	0	0	2.25	0.1	6	0	3	2
12	3	0	2.25	0.1	6	2.8	3	2
12	6	0	2.25	0.1	6	5.6	3	2
12	9	0	2.25	0.1	6	8.7	3	2
12	15	0	2.25	0.1	6	14	3	2
12	0	4	2.25	0.1	6	0	3	2
12	3	4	2.25	0.1	6	2.8	3	2
12	6	4	2.25	0.1	6	5.6	3	2
12	9	4	2.25	0.1	6	8.7	3	2
2.21	6	6	0.66	0.01	6	50	3	2

Table 5.1: *Sol-gel recipes. Quantities are given in ml. Zr prop – Zirconium n-propoxide; Y prop – yttrium isopropoxide solution; TEOS – the silica precursor tetra-ethylothosilicate. IPA – isopropyl alcohol; Mol% Y/Zr – the molar ratio of yttrium and zirconium ions displayed as a percentage. Sol 1 indicates the initial mixture placed in the sample environment, Sol 2 the mixture injected into Sol 1 to commence gelation.*

5.1.3 Silica-Zirconia and Silica-YSZ sol gels

Preparation for zirconia and YSZ in a silica matrix follows similar methods to pure YSZ synthesis. For both in-situ and ex-situ experiments, 4ml Tetraethylorthosilicate is added to zirconium n-propoxide, and the two alkoxides are stirred to ensure complete

miscibility. A volume of yttrium isopropoxide solution is also added at this stage for the preparation of YSZ-Si systems. 2.25ml Acetyl acetone, 0.1ml acetic acid were then immediately stirred into the alkoxide blendes to chellate the precursors and stabilize pH. Hydrolysis was induced by injection of 5ml of an isopropanol:water solution in a volume ration 3:2 in a similar manner to the preparation of pure zirconia gels. The recipes, along with the volumes of yttrium isopropoxide used for the investigations, are show in the lower half of table 5.1.

5.1.4 Silica-Zinc sol gels

5.1.4.1 Preparation of the silica matrix

Silica solgel is made by first dissolving 4ml Tetraethylorthosilicate (TEOS) with 4ml Isopropanol. Hydrolysis is achieved by adding a further 1ml of 1Molar solution nitric acid.

For in situ experiments, the silica sol is then placed in an aluminium sample cell with kapton windows (figure 5.2), separated by 2mm and maintained at a temperature of 70°C. Zinc sols were remotely injected into the silica as the gel network began to form

5.1.4.2 Zinc sols

The recipe used to make a Zinc sol is similar to that used to coat substrates with orientated Zinc Oxide nanocrystals for use in detector systems. [67,68,69,70] Zinc Acetate is

first dissolved in Methoxyethanol (MEA) with an equal quantity of Ethanolamine. The mixture is kept at a constant 70°C to ensure complete solubility of the zinc acetate.

The silica and zinc sols are then mixed whilst maintaining a constant temperature of 70°C. Different volumes of zinc sol and silica sol were mixed to produce different concentrations of zinc. (See table 5.2)

Zinc Sol (ml)	**Silica Sol (ml)**
8	0
7	1
6	2
5	3
4	4
3	5
2	6
1	7

Table 5.2: *The volumes of zinc and silica sols mixed for the silica-zinc gelation experiments.*

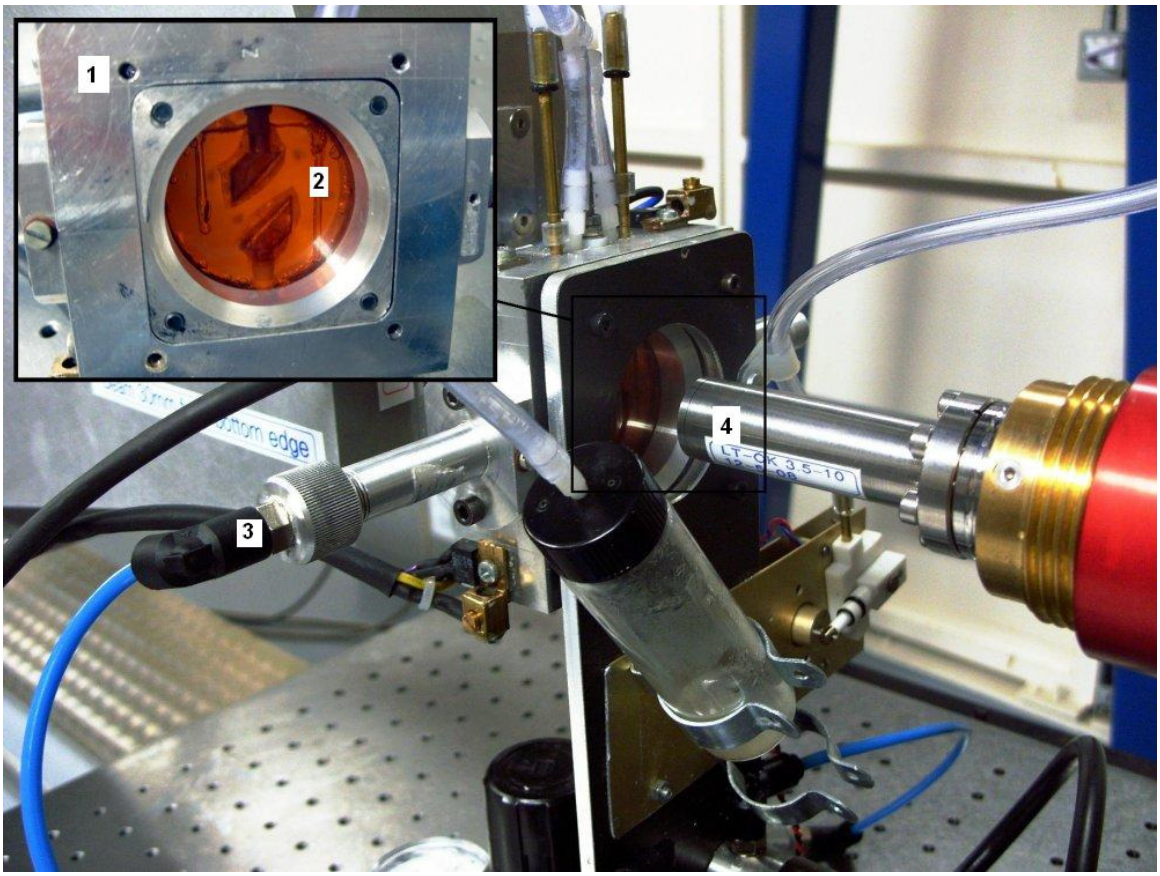

Figure 5.2: *The sample environment used for time resolved ASAXS investigations of zinc-silica systems. Shown here is the sample environment set up on beamline I22 at Diamond Light Source Ltd. An initial silica gel precursor material is contained within the main cell (insert, 1) which is visible through the kapton window (2). Zinc ions and hydrolysis is induced by injection from a pneumatic pump (3), into the main cell which forces mixing. An incident X-ray beam emerges from the beamline end pipe (4) where it is scattered by the sample.*
.

5.2 Xerogels

Preprepared gels were left for 24 hours in a sealed vessel to densify, and the excess solvent drained. Before placing in a furnace, the dried gels were left in open air to allow evaporation of any remaining volatiles.

For Ex-situ (X-ray diffraction) experiments, the xerogels were placed in a furnace, and heated in 50°C steps up to 1000°C, and after each step, the xerogel was allowed to cool, and then crushed into a fine powder with a mortar and pestle for powder diffraction.
Xerogels for in situ experiments were dried in open air, and then pressed into pellets 13mm in diameter and 0.3mm thick, using an applied pressure of 10 tonnes.

5.3 Beamline Methods

In situ ASAXS investigations require the use of synchrotron radiation facilities such as Diamond Light Source Ltd, Oxford, and BESSY, Berlin. As previously mentioned in chapter 4, a small angle scattering beamline consists of a series of slits and mirrors designed to focus highly collimated monochromatic X-ray beams of high intensity. The beam intensity must be sufficient to ensure the photon count is large enough to allow a scattering pattern to be detected in as small a time-scale as possible. The beam width in energy space must also be small enough to accommodate cycling energies across the absorption resonance. The spatial dimensions of the beam must also be small, of the order of less than a millimeter in width, so blurred scattering effects are minimised.

5.3.1 Sample Environments

For in situ gelation experiments, a sample environment was custom built from an aluminium frame with kapton windows to allow passage of the X-ray beam through the sample (see figures. 5.1 and 5.2). Sol gel reactions were initiated by placing one mixture

in the sample cell where the beam passes, and another in a syringe. The second solution is then be injected remotely in order to observe the reactions at the onset of hydrolysis. The entire cell is placed on a hotplate and set in order to maintain a constant temperature of 50°C across the sample for the case of YSZ, and 70°C across the sample for the zinc based systems. An aluminium sample cell ensured proper heat conduction. A completely full sample cell had maximum temperature gradient of 2°C from top to bottom. The beamline sample area was arranged in order to facilitate the hotplate and sample environment.

5.3.2 The Furnace

Figure 5.3 is a photograph of the furnace used during in situ sintering experiments at beamline 6.2, SRS Daresbury. The furnace was custom built for the beamline by the Workshop of the Royal Institution of Great Britain, London.

The ceramic furnace has an internal heating element made from platinum wire, and is capable of sustaining temperatures up to 1000°C. Temperatures are controlled by means of a remote interface plugged into a computer in the control room using the LabView software package. The package allows for the construction of complex temperature profiles which can be sent to the furnace during an experiment.

For the sintering experiments, temperatures were ramped up at a rate of 10°C per minute to 1000°C, giving a total duration for each experimental run of 1 hour 40 minutes.

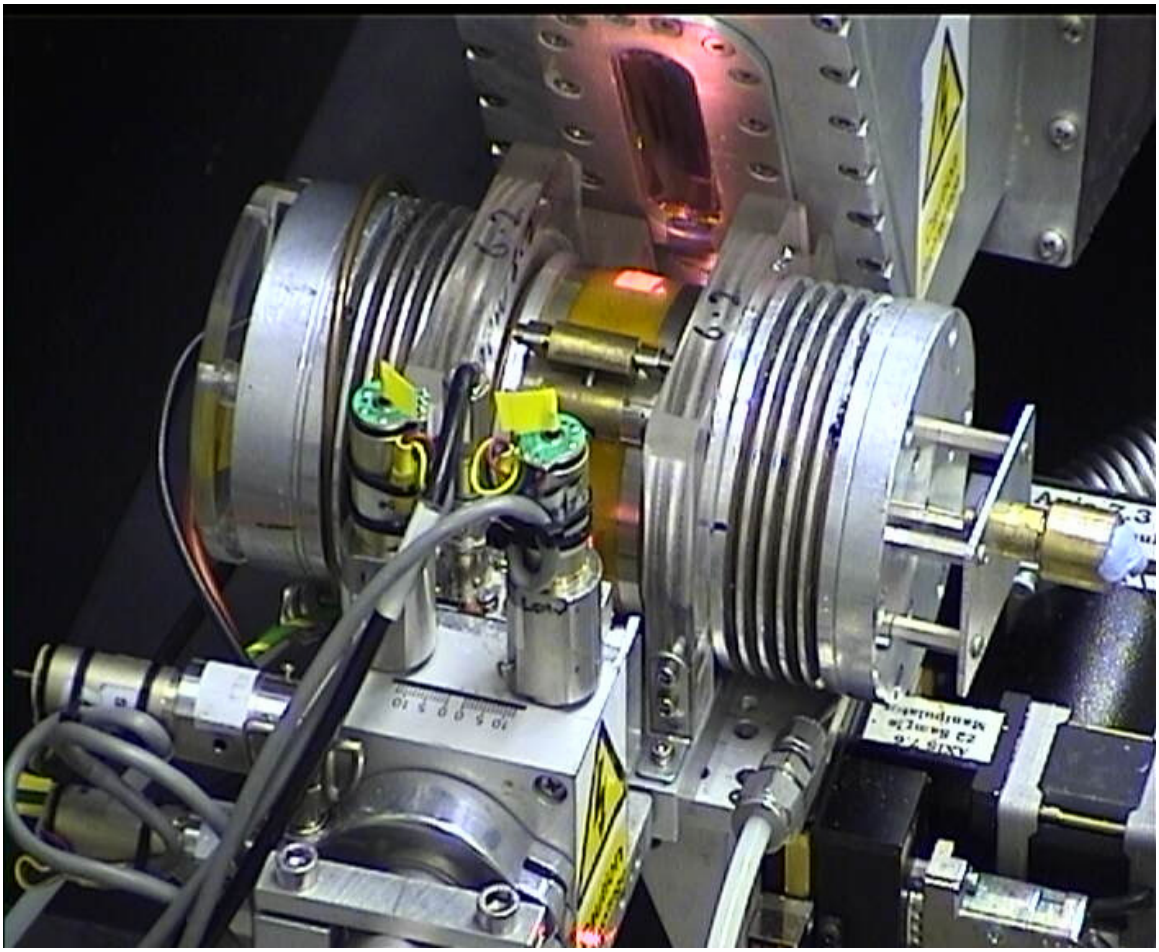

Figure 5.3: *The calcinations furnace used for in situ ASAXS experiments. Shown here is the set up for SAXS Beamline 6.2 at SRS Daresbury Laboratory. The reddish glow of the heated sample is visible through the kapton window.*

5.3.3 Monitoring the transmitted and reflected beam

Measurements of the empty sample environments are taken for each of the energies used in the experiments. For the case of experiments conducted at Daresbury Laboratory, normalisation is achieved through continuous measurements of the X-ray photon counts of the transmitted and reflected beam using two ion chambers, positioned both before and after the beam passes through the sample, during each SAXS measurement. At Beamline

I22, Diamond Light Source, incident and transmitted beam intensities are measured using a photosensitive diode placed on the beam stop close to the detector. A second diode, positioned between the monochromator and sample, could be moved in and out of the beam path to measure the incident beam intensity at different energies.

5.3.4 Detectors and Camera Lengths

Using the 1d quadrant detector at Daresbury, zirconia and YSZ experiments are performed using a camera length of 3.75m, and a detector channel resolution of 1024. The maximum value of q attainable on the zirconium edge at 18keV was 4.95nm^{-1}.

Zinc-silica sol-gel experiments on beamline I22, Diamond Light Source, are measured using a 2d CCD detector with a 512x512 pixel (channel) resolution and a camera length of 4m. The maximum value of q attained is 3.0nm^{-1} at the zinc absorption edge.

5.3.5 Beamtime

In any ASAXS experiment, it is crucial to know what energies are used in relation to the distance from the absorption edge. A typical experiment will consist of the following preparations:

- Tuning the monochromator
- Scattering from Silver Behanate
- Scattering from the sample environment

- Calibrating the monochromator
- Ex-situ EXAFS of the initial sample
- Writing a script to continuously cycle beam energies
- In situ ASAXS and In situ EXAFS

5.3.6 Tuning the Monochromator

Monochromators used are those already provided on the beamline.

The energy is chosen by changing the angle of a Si(111) crystal to the incident white beam, which is done remotely via a software interface custom programmed for the specific beamline. The collimated monochromatic beam is then focused onto the detector or sample environment for data collection. The energy is chosen to be one close to, or just below the absorption edge of interest, or in the case of two adjacent absorption edges (double ASAXS), the monochromator is tuned to a value exactly between the two edges. The beamline is then optimized for this particular energy, and can cycle through a range of energies within ±1keV without the need to further adjust slits and mirrors to prevent beam migration. The double ASAXS experiments were performed at beamline 6.2, Daresbury, which uses a wiggler.

5.3.7 Scattering from Silver Behenate or Collagen

These are standard calibrants for determining the q-scaling of the scattering function. Silver Behenate has a diffraction peak (001) at 5.838 nm, and further resonances, (002, 003 etc) are clearly visible, corresponding to q values of 0.93nm^{-1}, 1.86 nm^{-1}, 2.79 nm^{-1}, ... , It is a suitable calibrant for higher energies, or shorter camera lengths, where the q-range (maximum value of q 'visible' in the scattering pattern) is relatively large.

For larger particle sizes, lower energies and very long camera lengths, where the q-range is less than 1nm^{-1} an alternative calibrant is collagen. This is a biological material extracted from rats tail, and has a typical Bragg peak at 66.8nm (q=0.094nm^{-1})

Both calibrants also serve as a means to accurately determine the central beam position relative to the detector, since both will scatter X-rays to create 'rings' from which the centers can be calculated (and hence the beam position). The beam position is also located by means of a diode placed on a beamstop immediately before the detector. (A lead beamstop is required in order to prevent unscattered beam intensity from damaging the detector.) For this reason, scans are normally carried out over a range of energies both far below and close to the absorption edge to track any potential beam migration.

5.3.8 Scattering from the Sample Environment

The sample container will always have a scattering contribution in the data which needs to be accurately known and removed (see chapter 6, section 1). The SAXS pattern is

measured over a longer time period (typically several minutes) across a range of energies to obtain an accurate function. Further SAXS patterns, taken at a range of energies, are taken of the sample cell and principle solvents to deduce their additional scattering contributions. For both gelation and sintering experiments, the main contribution is from the kapton windows.

5.3.9 Calibrating the monochromator

Absorption edges for pure metals are accurately known for most elements - and in particular those of interest and in the range of ASAXS investigations. If the exact energies are required, instead of a relative distance from an edge, the values can be calculated by taking an X-ray absorption spectrum of a metallic foil of the edge of interest.

Figure 5.4 shows the absorption spectrum for Zirconium foil. Differentiation of the spectrum (5.4 top) reveals a sharp minimum (shown by the 'valley' shape 5.4 bottom) at 17.8keV. Since the exact value of the zirconium K-edge is known, the scale on the monochromator is calibrated to this value. In this case, the measured uncalibrated value 17.8keV is reset as 17.9975keV – the value of the zirconium absorption edge. However, since ASAXS only deals with *relative* distances from an absorption edge, the calibration is not always necessary unless comparing between experiments performed on different beamlines. The foils are then compared to the sample to determine the chemical shift (motion of the absorption edge).

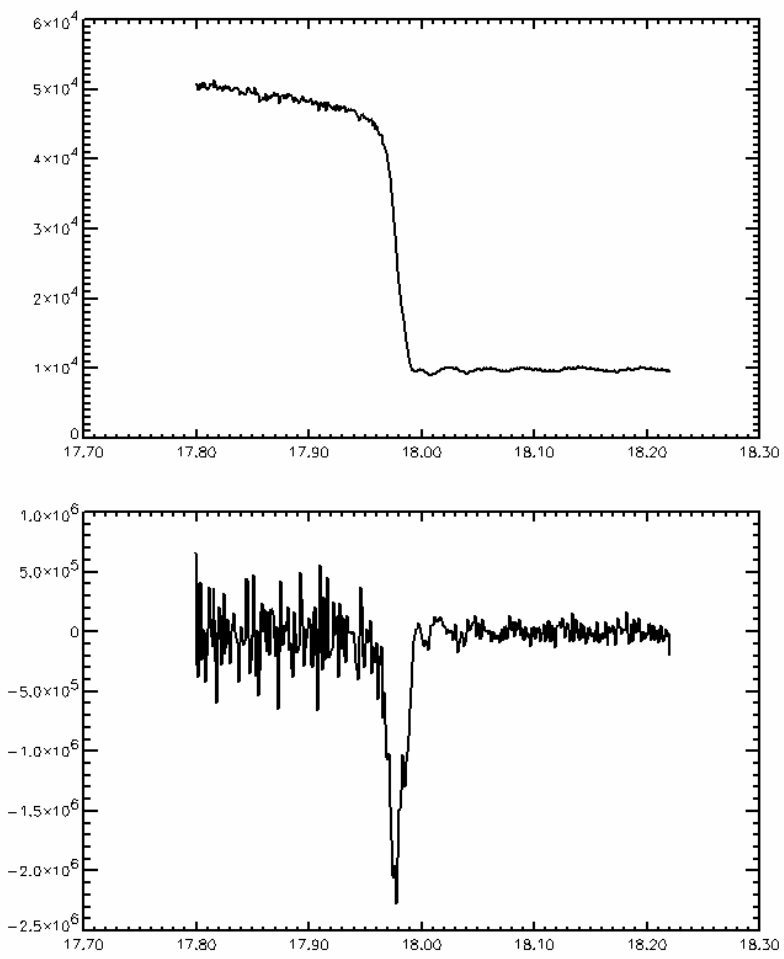

Figure 5.4: *A Zirconium Foil absorption scan across the K edge (top) is differentiated to reveal a minimum (shown by the sharp 'V' at 17.98 keV). Since the Zirconium edge is known to be exactly 17.9975keV, the monochromator can be tuned to the minimum, and the scale reset to the true value of the zirconium edge.*

5.3.10 Absorption spectrum of the sample

In order to choose correct values for the energies, in particular to ensure at least two will lie within the resonance, (see figure 4.3) a similar X-ray absorption spectrum of the sample is carried out, and differentiated to properly obtain the edge position. As shown by figure 5.5, there will be a difference in the value of the absorption edge from that of

the native metal. This is caused by interactions between zirconium ions and the immediately surrounding atoms (for sol-gel ceramics, these are oxygen) and is generally known as a chemical shift.

Chemical evolution of the sample, such as structural or compound changes, will also create additional shifts in the edge position. To ensure energies are kept within the resonance minimum, a second absorption spectrum of a pre-prepared sample as it would be at the end of the experiment is done. The two edges can then be compared and accurate energies chosen.

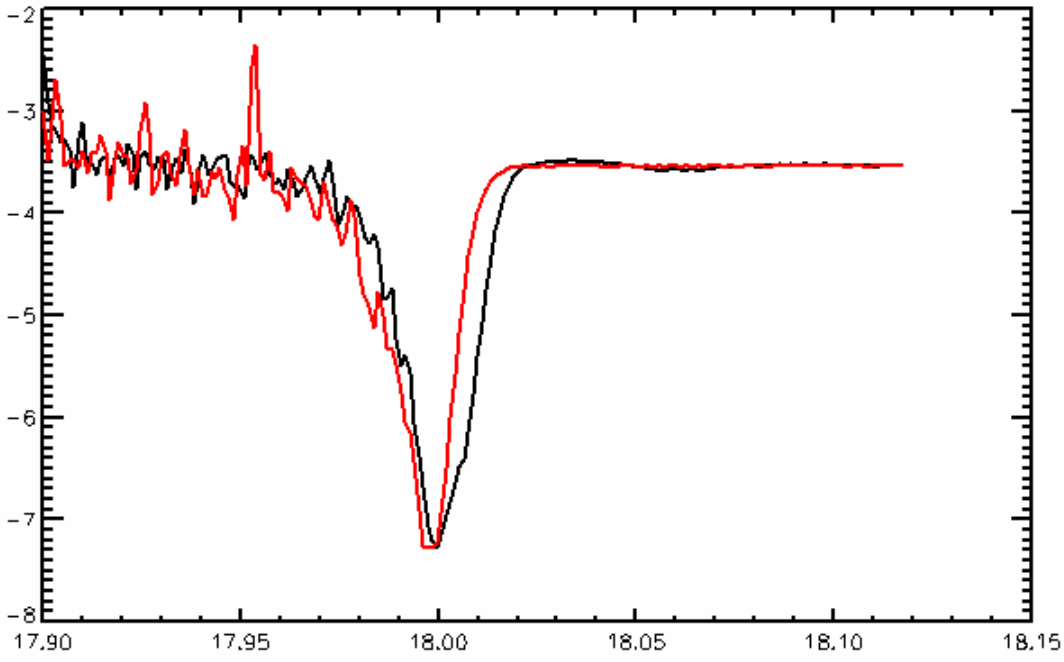

Figure 5.5 *Differentials of the absoption spectrum of a sample. Shown here is the chemical shift experienced by a zirconia xerogel (black) is heated to 1000°C to become a dense ceramic (red). The edge position has changed by -3eV.*

5.3.11 Scripting the energies

In situ ASAXS experiments will ultimately consist of many cycled scattering patterns taken at different energies. To avoid having to manually type the energies each time, a script can be written into the beamline software to cycle the energies, and output the scattering data. Beamline I22 at Diamond Light Source, and 6.2 at Daresbury both use GDA as an interface. GDA is a jython based data acquisition software platform.

Figure 5.6 shows a screen shot of a typical GDA script used for in situ ASAXS experiments. The energies listed are chosen to cycle across the resonance of a zirconia sol gel.

```
#
from time import sleep
#
#
# This is the object that controls access to jython
#
#jsf = gda.jython.JythonServerFacade.getInstance()
#
import time
while (carryOn):
#
        energies = [17.8,18.000,18.003,18.006,18.038]
#
        for e in energies:
#
# This moves the mono to the required energy
#
                energy.moveTo(e)
#
# This does whatever SAX/WAXS is set up
#
                ncddetectors.collectData()
                while(ncddetectors.getStatus() == 1):
                        sleep(0.1)
                ncddetectors.readout()
                ncddetectors.clear()
#
#
        time.sleep(1)
print "done"
```

Figure 5.6 *The jython script for cycling energies. An energies array is determined, where the user can enter their chosen energies for the experiment. Once declared, an infinite loop is set which tells the monochromator to move to each energy in turn and take a reading from the detector, which will cycle continuously. The loop is terminated by entering 'carryOn=0' (false) on the GDA command window. The energies will complete the current cycle before exiting. To start a new experiment, CarryOn must be set to '1' (true) to initiate a new continuous loop.*

5.3.12 Performing the Experiment

With the monochromator and detectors properly calibrated, each sample is investigated first by using a succession of cycled energies, and then repeated with continuous X-ray absorption scans (EXAFS). In an ideal experiment, the EXAFS would be carried out after each cycle - however the longer data acquisition time makes such a set up unfeasible. Separate in-situ EXAFS experiments using identical samples are required when chemical shifts occur. The scans monitor how the edge moves, and hence changes in the scattering corrections *f'* and *f''* with time

For the YSZ gelation and calcinations experiments, using a quadrant detector, each SAXS frame is acquired over 2 second intervals. The zinc ASAXS experiments use a 2D CCD detector, and data acquired at a rate of 10 seconds per SAXS frame.

Chapter 6

Data Analysis

6.1 Data reduction

The scattered signal which would be collected from only the sample is calculated using the relation in equation 6.1

$$I_E = \frac{SI_{0S}}{\tau_s t_s} - \frac{BI_{0B}}{\tau_B t_B} \qquad (6.1)$$

Here, S and B are the raw data from the sample and its environment, and the empty sample environments respectively. I_{0S} and I_{0B} represent the intensities of the incident (non-scattered) beams, τ is the transmission measurements, and t is the data acquisition time. For the gelation experiments, the sample environment is the gelation cell. For sintering experiments, it is the furnace.

Uncertainties in I(q) are calculated by measuring the amplitude of the noise in the SAXS patterns to give a ratio ΔI/I. Similar calculations are performed to obtain a margin of error in the determined ASAXS normal and resonant terms.

Since neither I22, nor beamline 6.2 at Daresbury have a fluorescence detector, fluorescence contributions are subtracted using the measurements taken from the wide

angle (WAXS) detector. The higher angles are chosen to ensure no scattering features from the sample, such as Bragg peaks, are present. Photon counts from the high angle segment are averaged, and then normalised against the value obtained from a measurement taken far below the absorption edges of interest. It is assumed that Fluorescence contributions from small elements such as carbon, oxygen and silicon, are negligible.

Investigations performed at Daresbury laboratory use a 1d quadrant detector. As fluorescence is assumed to be uniform over all angles, the values obtained from the SAXS segment actually become the gradient of a function of the form $y=mx$ due to the SAXS detector shape. Fluorescence subtraction and radial averaging is achieved by dividing the linear function with the result obtained from equation 6.1.

Detector response and flat field corrections were determined by beam-line staff prior to the commencement of experiments.

6.2 Solving the terms

ASAXS deconvolution is performed using Interactive Data Language (IDL) programming software. A linear interpolation scheme is applied to the normalised scattering functions to ensure each data point matches with their appropriate value in q space. This results in scattering functions in a slightly larger q-window than others, since q is inversely proportional to X-ray wavelength (see equation 3.2) and hence proportional

to photon energy. The highest value of q for the lowest energy a measurement is taken is made the upper limit (cut off point) on which ASAXS algorithms are applied to the data.

6.2.1 Corrections to the atomic scattering functions

EXAFS measurements taken during the experiments are normalised to theoretical data tables provided for download on the internet by Ethan A Merrit [73]. The EXAFS plots are assumed to correspond to values of *f''*.

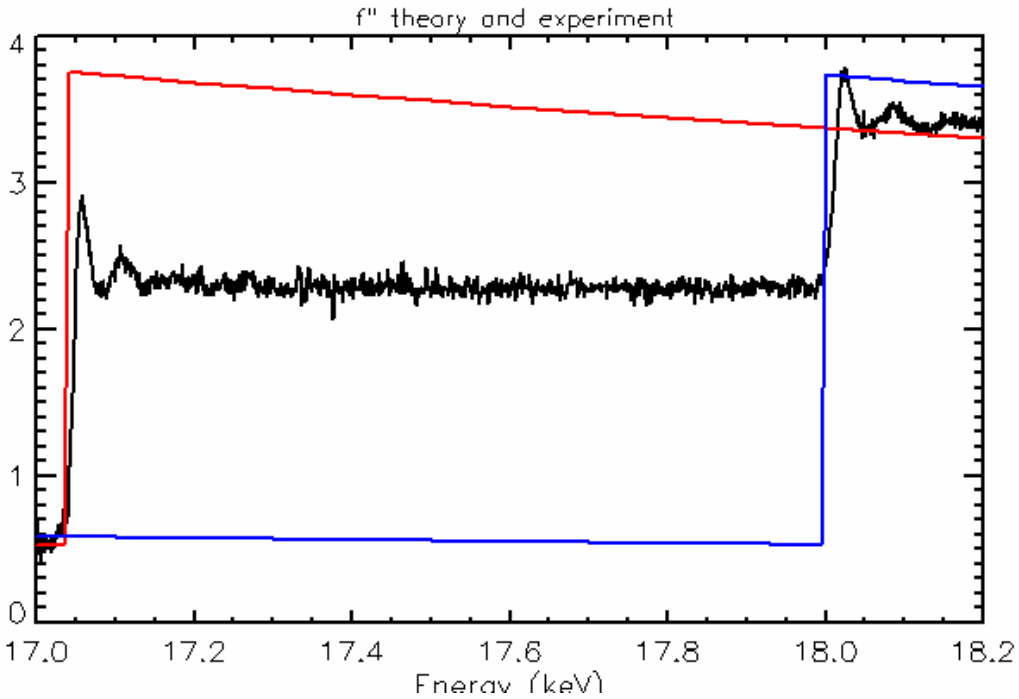

Figure 6.1. *Normalisation of the X-ray absorption spectra to theoretical values of f''. Shown here is the EXAFS spectrum for yttria stabilized zirconia spanning both edges (black) A higher percentage of yttria has been added for visual clarity. The red and blue step functions correspond to the theoretically calculated yttrium and the zirconium edges respectively.*

Figure 6.1 shows how the X-ray absorption spectra are normalised to theoretical values of *f''*. The function is the integrated using the Kramers-Kronig relation (equation 4.3), which is expanded to the following form [55]:

$$f'(E) = \frac{2}{\pi}\left[\int_0^x \frac{Ef''(E)dE}{E_0^2 - E^2} + \int_x^y \frac{Ef''(E)dE}{E_0^2 - E^2} + \int_y^\infty \frac{Ef''(E)dE}{E_0^2 - E^2}\right] \quad \ldots\ldots 6.2$$

The *x* and *y* terms in the integrals of equation 6.2 are the lowest and highest energies used in the EXAFS scan. Essentially, the middle term integrates the region covered by EXAFS scan, while the remaining two terms are derived from theoretical calculations.

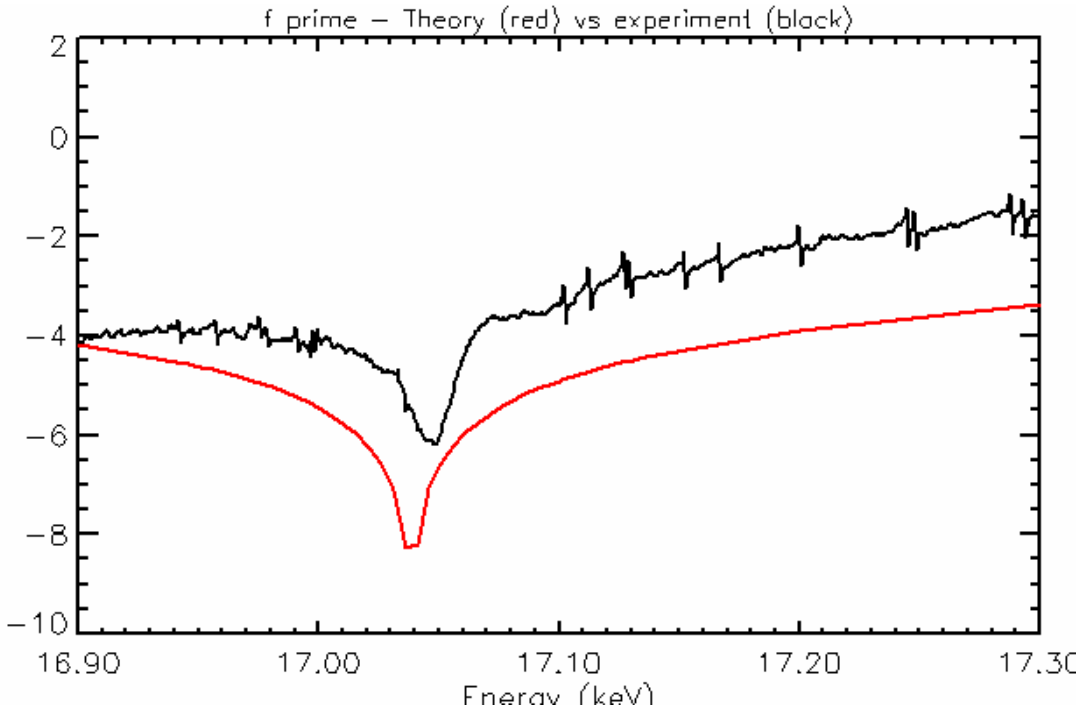

Figure 6.2: *A comparison between theoretically calculated values of f' against those determined from experiment. Shown here are the values of f' across the yttrium edge for yttria stabilised zirconia.*

As shown by figure 6.2, there is a difference between theoretical calculations and the values of f' derived from experimental data. Theoretical calculations are derived from solving the Kramers Kronig relation (equation 4.3) explicitly [57] and are assumed to be the spectra obtained from pure metals. The difference between theory and experiment observed is due to the absorbing ions (in this case yttrium and zirconium) being present as compounds rather than their pure metallic form. Better fits could be obtained by increasing the range in which an absorption spectrum is measured (but would reduce time resolution due to the increased data acquisition time), or by deriving theoretically derived values of the compounds. However, this would be a separate research project in its own right, and is therefore only mentioned as a subject for further work.

The figure describes the values of *f'* across the yttrium K edge for yttria stabilised zirconia. Intensity of the resonance minimum is also dependent on the concentration of yttria to zirconia - making derived *f'* values unique for a particular sample. The 'wiggles' visible in the experimental data are a result of noise in the original absorption spectrum that was integrated.

6.2.2 Deconvolution

Once the values of *f'* and *f''* are determined, the normal, cross and resonant terms are solved using the matrix form of equation 3.2.

$$\begin{pmatrix} f_0^2 & 2f_0f'_{E1} & f'^2_{E1}+f''^2_{E1} \\ f_0^2 & 2f_0f'_{E2} & f'^2_{E2}+f''^2_{E2} \\ f_0^2 & 2f_0f'_{E3} & f'^2_{E3}+f''^2_{E3} \end{pmatrix} \begin{pmatrix} I_n \\ I_c \\ I_r \end{pmatrix} = \begin{pmatrix} I_{E1} \\ I_{E2} \\ I_{E3} \end{pmatrix} \quad \ldots\ldots 6.3$$

Which for multiple edge ASAXS is the matrix form of equation 3.9.

$$\begin{pmatrix} A_1 & 0 & ... & 0 \\ 0 & A_2 & ... & 0 \\ ... & ... & ... & ... \\ 0 & 0 & ... & A_n \end{pmatrix} \begin{pmatrix} X_1 \\ X_2 \\ ... \\ X_n \end{pmatrix} = \begin{pmatrix} B_1 \\ B_2 \\ ... \\ B_n \end{pmatrix} \qquad \text{……. 6.4}$$

The terms I_{E1},I_{E2} and I_{E3} correspond to the SAXS scattering patterns taken at three energies in a consecutive cycle. In equation 6.4, A_n corresponds to the operator matrix containing the corrections to the atomic scattering functions, B_n is the three SAXS scattering functions and X_n is the normal, cross and resonant terms for edge element n.

Matrices are solved using Cramer's Rule. For a matrix equation $Ax=b$, the general case for solving x is,

$$x_m = \frac{\det(A_m)}{\det(A)} \quad \text{…. 6.5}$$

Where A_m is the matrix obtained by replacing the nth column in the operator matrix A with column vector b.

Chapter 7

Computational and Mathematical Models of Anomalous SAXS Results

Cumulative errors during experimental procedure place additional constraints on the range of potential anomalous scattering experiments in terms of time resolution and materials. The detector system will have its own noise which overlays the scattering function [74], and the resolution of the monochromator generates errors in determining accurate energies [75,76]. Of particular importance is the use of accurate values for the cross and resonant term pre-factors determined by the Kramers Kronig relation (see chapter 4, section 1 and equation 4.3). This chapter aims to tackle those issues using a combination of simulated and experimental data, and provide insight into how slight variations in the resonant term pre-factors can be used to extract the overall shape and form of the normal, cross and resonant terms.

7.1 Signal versus Noise

The ASAXS equation 4.2 is dominated by the normal term due to the pre-factor, f_0^2. For atoms with large proton numbers, such as zirconia, this number can be over 100 times the pre factors for the resonant term[64] when comparing the ratios of terms between the normal and resonant. It has already been discussed in chapters three and four that elements with proton numbers of between 20 and 41 have K-edges within range of most synchrotron sources, with the L and M edges coming into range for the heaviest elements.

This rapidly increases the dominance of the normal term at the expense of the resonant in all but the lightest elements.

Theoretical calculations of the corrections to the atomic scattering factors show *f'* varies from -0.5 far away from the edge, to -8 on the edge. For *f''*, the values vary from 0.5 below the edge, to 3.5 just above the edge (see figure 6.2). Even at maximum contrast, using values of *f'*=-8 and *f''*=2.0 (derived from theoretical calculations), the resonant term pre-factor is unlikely to reach a value greater than 70. The inherent problem of attempting to solve an equation for a small effect implies that any detector noise present in the scattering function is going to be amplified. The signal to noise ratio places an additional upper limit on what elements a successful ASAXS experiment can be performed.

In general comparing the ratios of the cross and resonant to the normal terms can be considered to give an upper limit for a detector with a known signal to noise ratio, which can be expressed as,

$$\frac{\Delta I}{I} = \frac{f'^2 + f''^2}{f_0^2} \quad \ldots\ldots. 7.1$$

Where ΔI is the average amplitude of the detector noise and I is the average intensity of the scattering function. The resonant term pre-factors, derived from the Kramers-Kronig relation, are taken as those of the energy closest to the edge position.

The 1d HOTSAXS quadrant detector used during experiments at beam-line 6.2 at Daresbury Laboratory [77] has an average noise-signal ratio, $\Delta I/I$ of 0.075. When inserted into equation 7.1, using the values of *f'* and *f''* at maximum contrast (ie, on the absorption

edge), reveals an upper limit for the proton number, f_0, to be 30. This is the proton number for zinc. The result has implications for potential ASAXS experiments of heavier elements using L and M edges, and those K-edge elements with proton numbers greater than 30. Zirconium, which has an absorption K-edge of 17.9975keV, is close to the upper limit of the range of most synchrotron SAXS beam-lines, and would have resonance effects that dwell within the detector noise.

Fortunately, the detector noise is fairly periodic, and the chosen energy closest to the edge is never going to be exactly on the edge due to the monochromator resolution. Smoothing and Fourier transforms can be performed to increase the signal-noise ratio, with negligible loss of the underlying subtle differences in scattering functions associated with ASAXS. For non ordered structures, such as glasses, ceramics and sol-gel, the features are generally a lot broader than the frequency of the noise, and any applied smoothing function will preserve the broader contrast features, provided the smoothing range is very much smaller than the width of the contrast variation.

Figure 7.1 shows the result of applying a smoothing algorithm on experimental data to increase the signal to noise ratio. The detector noise, shown by periodic oscillations in the raw data (black) has been minimised by smoothing, whilst preserving the broader features (red). After smoothing, the noise to signal ratio is reduced to a value of $2.4x10^{-3}$, which corresponds to an upper proton number limit of 170 after solving equation 7.1, and assuming a resonant term pre-factor of 70. Naturally occurring, stable elements, have proton numbers below 92 (Uranium).

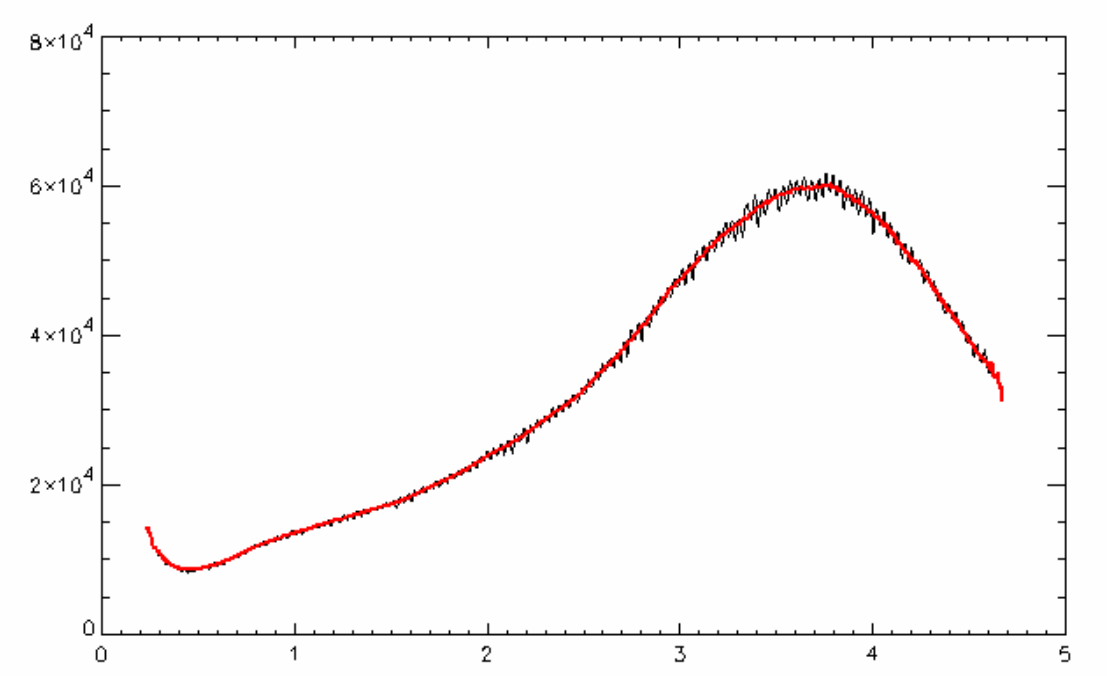

Figure 7.1 *Reducing the signal-noise ratio by applying smoothing functions. The periodic, higher frequency oscillations from the detector in the raw data (black) are minimised, giving a 'curve of best fit' shown by the red. The line thickness of the smoothed function has been increased for clarity.*

7.2 Monochromator Resolution

The vast majority of SAXS beamlines with the facility to do anomalous scattering, all use silicon crystals aligned to the (111) plane for monochromatic tuning. A Si(111) crystal has an energy resolution of 1.2×10^{-4}. The range of energies available at such beamlines is between 5keV and 20keV, which corresponds to energy resolutions of 0.6eV and 2.4eV respectively.

Figure 7.2 shows a typical edge minimum as a plot of energy versus *f'*. Unlike the relatively broad minimum present in theoretical data, experimentally determined values

have a much narrower resonance. Shown here the *f'* values, for zirconia, are typical for most oxide ceramic materials. The thin resonance limits the range of energies to a band within 20eV. At 18keV, the monochromator resolution is 2.16eV, which results in a broadening and an averaging of *f'* over that range. The number of energies that can be used is also limited. Additional energies may be required in the event of large chemical shifts which would otherwise move the original choices outside of the minimum. Any additional energy choices should be separated by at least the width of the monochromator resolution in order to provide the best possible contrast and minimise resolution error.

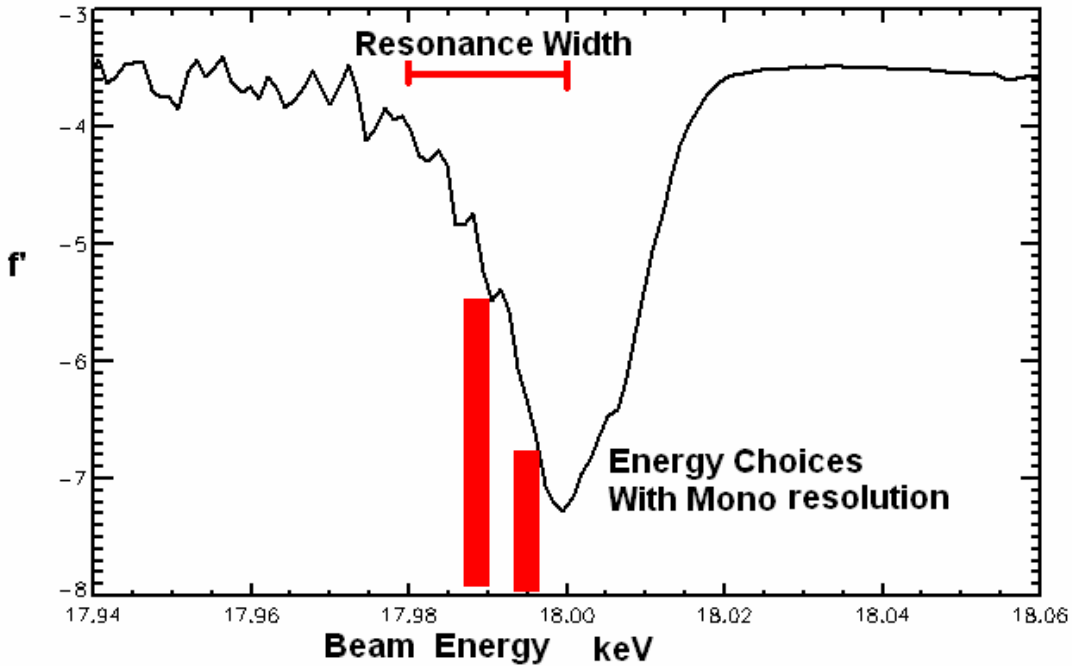

Figure 7.2*: The choices of energy are limited by the monochromator resolution and width of the resonance slope. The choices should be separated by at least the width of the monochromator resolution, while at the same time remaining inside the resonance for the duration of the experiment.*

The monochromator resolution limit automatically places an uncertainty on the values of *f'* and *f''*. Uncertainties in the motion of the mechanisms that orientate the monochromator crystal correspond to additional fluctuations in the actual centre of the beam width in energy space. As can be seen by figure 7.2, the possible variations in *f'* over the peak intensity of the resolution width can vary by as much as ±0.2. Though the broader beam in energy space will result in an averaging of *f'* over that range, the uncertainty associated with monochromator movement fluctuations can result in inaccurate measurements of *f'* for a given cycle. Such inaccuracies can lead to wrong conclusions and peculiar effects in the deconvoluted data; the subject of the following sections.

7.3 The Sensitivity Problem

Since the normal term is much larger than the resonant term, the problem arises into how sensitive is a solution with slight variations in the calculated values of *f'* and *f''*. The following sections describe the issues arising from the sensitivity, and offers methods to ensure a correct solution is obtained, as well as how to spot where things could go wrong.

As described in chapter 4, (equation 4.2,) the scattering function of a composite material comprises of partial contributions from each species of element. This leads to slight changes in the shape of the function as X-ray energies approach an absorption edge. The effect has led to equation 4.2, which describes a scattering function as being the sum of three terms; the normal, cross and resonant. The resonant term, which is the scattering

contribution from the absorbing element, increases in intensity at energies very close to the absorption edge due to the pre-factors *f'* and *f''*, which are derived from the Kramers-Kronig relation, (equation 4.3).

$$I(q) = f_0^2 I_n(q) + 2 f_0 f' I_c(q) + \left(f'^2 + f''^2\right) I_r(q) \quad \ldots. (4.2)$$

A cycle of three energies can be solved by considering equation 4.2 as a system of simultaneous equations.

$$Ax(q) + B_1 y(q) + C_1 z(q) = I_1(q) \quad \ldots.. (7.2a)$$

$$Ax(q) + B_2 y(q) + C_2 z(q) = I_2(q) \ldots.. (7.2b)$$

$$Ax(q) + B_3 y(q) + C_3 z(q) = I_3(q) \quad \ldots.. (7.2c)$$

Where,

$$A = f_0^2$$

$$B_n = 2 f_0 f_n'$$

$$C_n = \left(f_n'^2 + f_n''^2\right)$$

The functions *x(q), y(q)* and *z(q)* correspond to the normal, cross and resonant terms respectively.

Solving explicitly for the resonant term *z(q)* reveals,

$$z(q) = \frac{(B_2 - B_3)(I_1(q) - I_2(q)) - (B_1 - B_2)(I_2(q) - I_3(q))}{(B_2 - B_3)(C_1 - C_2) - (B_1 - B_2)(C_2 - C_3)} \quad \text{.... (7.3)}$$

While for the cross,

$$y(q) = \frac{(C_1 - C_2)(I_2(q) - I_3(q)) - (C_2 - C_3)(I_1(q) - I_2(q))}{(B_2 - B_3)(C_1 - C_2) - (B_1 - B_2)(C_2 - C_3)} \quad \text{.... (7.4)}$$

It can be seen that the scattering functions for the three energies are all on the top of the fraction, while the denominator, which is a collection of constants for the given energies, is identical for both. The form of the resonant term is dependant on the cross term pre-factor, B_n, and so the values of *f'* only, since it is assumed the proton number is known precisely. The form of the cross term, however, is dependent only on the values of the resonant term prefactor, C_n, which contains both *f'* and *f''*.

The resonant term can also be further reduced, since $2f_0$ cancels.

$$z(q) = \frac{(f_2' - f_3')(I_1(q) - I_2(q)) - (f_1' - f_2')(I_2(q) - I_3(q))}{(f_2' - f_3')(C_1 - C_2) - (f_1' - f_2')(C_2 - C_3)} \quad \text{..... (7.5)}$$

Equation 7.5 shows the scattering correction term for the second and third energies, f'_2 and f'_3, as having the greatest effect on the solution of the function, since f'_1 is generally smaller. Inaccurate values derived from the Kramers-Kronig relations will have the effect

of altering the solutions to the equation, and in particular, being most sensitive to the variations resulting from the second and third energies in the cycle.

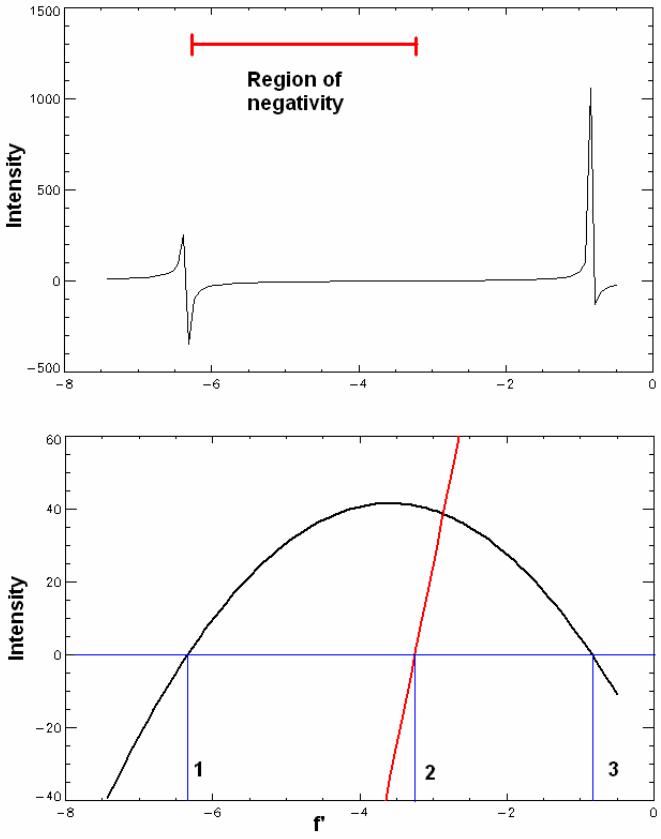

Figure 7.3: *Changes in intensity and sign of the resonant term in varying f'_2 , showing singularities and a region where the solution results in a negative scattering function (top). Bottom shows how the denominator (black) and the numerator (red) of equation 7.5 changes with the same variation.*

The plot in figure 7.3 shows the changes to the resonant term intensity as a function of changing f'_2 (top), for a given value of intensities for I_1, I_2 and I_3 at a single point in q space. Singularities occur in cases where the denominator approaches zero. The resonant term can also have zero intensity when the terms making up the numerator of equation 7.5 cancel to zero. Figure 7.3, bottom, shows the changes in the numerator (red) and

denominator as the middle *f'* (ie f_2') is varied. In regions 1 and 3, the solution is negative, whilst in region 2, the solution becomes positive. The actual solution for the resonant term must be positive, since it is the scattering contribution of the resonant scatterers, and so the true value for f'_2 must be in region 2; where both the numerator and denominator are of the same sign.

Applying this to the scattering functions for all q, it is evident that contrast effects between the scattering functions from the three different X-ray energies can either be enhanced or reduced if the values derived from the Kramers Kronig function happen to sit close to a point of inflection. Out side of these points, all or parts of the resonant term can be negative; the first indication of a wrong solution.

Figure 7.4 shows how a solution for the resonant term can change when the values derived from the Kramers Kronig relation are incorrect. Scattering plots have been modelled using simulated functions for the normal, cross and resonant terms. The normal term is that of a fractal network derived from equation 3.19, the resonant term is that of a distribution of small monodisperse spheres (equation 3.3), and the cross is an arbitrary combination of the two. The actual normal, cross and resonant terms are shown top left. Three functions representing the scattering from three different X-ray energies close to the absorption edge are then derived (figure 7.4, top right). These three functions are then solved for alternate solutions of the normal, cross and resonant terms using 10 different values for the mid energy *f'*, and the corresponding *f''*.

The bottom two plots of figure 7.4 show the effects of varying f_2' over a range of -4.5 to -3.5, with the actual value being -4.0. Lower magnitudes (bottom left) show a resonant term of increased intensity while at the same time contrast variation is lost, resulting in a

gradual change in the shape of the function; particularly noticeable in the higher q region where the spherical form factor of the correct resonant term is close to zero. For values close to the true value with slightly greater changes in f' magnitude - parts of the solution begin to have regions of negative intensity when f' is changed by 0.1. Increase the magnitude of f' further, and the resonant function is reflected along the q-axis, producing solutions with high negative intensities (figure 7.4, bottom right).

Results from this simplified model already provide insight into a method in which wrong results can be identified and inaccurate values of f' corrected. Strongly negative solutions from an experimental observation, can be the result of f' being too high in magnitude, and solutions where parts of the resonant term are negative are indicative of the calculated f' being out by a small margin, of the order of 0.1. In addition, given the width of the beam spectrum at a chosen energy, a small superposition of different results will be observed as the scattering pattern. However due to the Gaussian nature of the beam spectrum, the intensities of the additional superposition caused by a subsequent range of f' are much lower than the central 'focus'. The values can therefore be tweaked with these constraints in mind, to converge on a more accurate solution.

In addition, variations in the values for the third energy indicate a similar effect, but this time strongly negative solutions indicate a f_3' value that is too small in magnitude, whereas intensely positive solutions indicate f_3' as being too large. In any model designed to seek out the correct solutions, additional constraints (using prior knowledge) need to be imposed to consider this, which will be the covered in section 7.5.

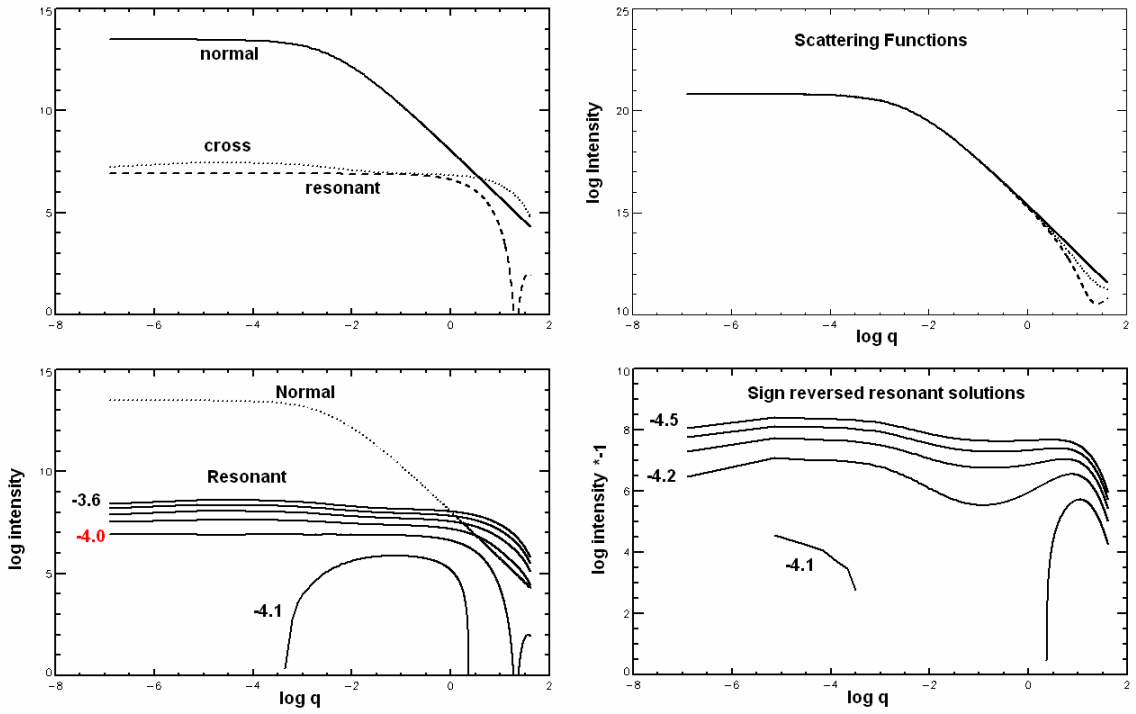

Figure 7.4 *Changes to the resonant term solution with varying f'. Top right: the true functions for the normal, cross and resonant terms are first simulated. Near edge scattering data is simulated using f'=-0.5,-4.0,-7.5, and f''=0.5, 1.5, 2.0 for the three energies (solid line, dotted and dashed) respectively (top left). Bottom left: The true value for the mid f' is -4.0, values of f' of a slightly lesser magnitude result in loss of features where the resonant term intensity is close to 0. Increased magnitude first exaggerates the contrast effects by making some parts of the solution negative at f'=-4.1. Increasing the magnitude further reflects the solution in the q axis, giving solutions of high negative intensity (bottom right) – the signs of the solutions have been reversed to enable logarithmic plotting for clarity.*

Changes in the coefficient, *f''*, do not alter the solution as much. EXAFS plots taken during an experiment are normalised to theoretical data across the chosen range of energies - since it is impossible to do an EXAFS scan spanning all energies from 0 to infinity. On the edge, *f''* is typically of the order of 2.0, with a total range across the entire resonance of 0.5 to 3.5. Energies are chosen so at least two sit in the resonance just

below the absorption edge, revealed by the minimum in *f'*. This makes the total possible range in which *f''* can change to within 0.5 to 2.0.

The resonant term prefactor, C_n, is the sum of the squares of both *f'* and *f''*. With *f'* typically ranging from -0.5 to -8.0, it is clear that this factor will also dominate C_n at energies very close to the absorption edge. For energies very close to the edge, $C_n \rightarrow f'^2$.

7.4 Simplifying the Model

For both *f'* and *f''*, energies far from the absorption edge are fairly constant. Conventional SAXS takes the assumption that they are both equal to zero, and so the scattering function obtained in experiment is that of the normal term. Far below any absorption edge, this can be a valid approximation since the values of both coefficients are minimal in magnitude (ie closer to zero). Taking the assumption of conventional SAXS that the complex corrections to be close to zero for off edge energies, the functions *z(q)* and *y(q)* can be simplified, so that (after expanding the brackets),

$$y(q) = \frac{C_2 I_3(q) - C_2 I_1(q) - C_3 I_2(q)}{B_3 C_2 - B_2 C_3} \quad \ldots. (7.6)$$

$$z(q) = \frac{f_2' I_1(q) - f_3' I_1(q) + f_3' I_2(q) - f_2' I_3(q)}{f_3' C_2 - f_2' C_3} \quad \ldots. (7.7)$$

Taking the additional assumption that for energies very close to the edge and within the absorption resonance, the contribution from *f''* is small compared to *f'*. The normal, cross and resonant terms become:

$$x(q) \approx \frac{I_1(q)}{f_0^2} \quad \ldots\ldots (7.8)$$

$$y(q) \approx \frac{f_2'^2 I_3(q) - f_2'^2 I_1(q) - f_3'^2 I_2(q)}{2f_0\left(f_3' f_2'^2 - f_2' f_3'^2\right)} \quad \ldots. (7.9)$$

$$z(q) = \frac{f_2' I_1(q) - f_3' I_1(q) + f_3' I_2(q) - f_2' I_3(q)}{f_3' f_2'^2 - f_2' f_3'^2} \quad \ldots.. (7.10)$$

The cross and resonant terms have now been reduced so only fluctuations in *f'* need be considered. This is assuming that the scattering function, $I_1(q)$, is taken using an X-ray photon energy far below any absorption edges present in the sample. $I_2(q)$ and $I_3(q)$ are also chosen so that the photon energies are within the absorption resonance just below the minimum, and remain within this region at all times during the experiment.

7.4.1 When energies are above the edge

The assumptions given above break down when chosen energies migrate across the absorption minimum, or even out of the resonance all together. Such events are possible if a larger than expected chemical shift occurs. Provided fluorescence and Resonant

Raman Scattering can be properly accounted for, greater contrast in the resonant term pre-factors can result, and even begin to compare with the cross term for smaller atoms. Above the absorption edge, and outside of the resonance, *f'* once again becomes small (approaching -0.5) whilst the step function, *f''*, can have a value of 3.5 across a wide range of energies. For a heavy metal such as zirconium, the pre-factors of equation 4.2 for a scattering function just above the absorption resonance can become, 1600, -40, 12.5 for the normal, cross and resonant terms respectively. For elements on the lower limit of the range of synchrotron sources, such as vanadium which has a proton number of 23, the numerical values of the pre factors can reach, 529,-23,12.5.

Consider a situation where chosen energies are positioned around the absorption edge in such a way that two or more are on opposite sides of the absorption resonance. In these cases, their complex corrections, *f'*, become identical. Taking equation 4.2, and subtracting one scattering function from the other and rearranging reveals,

$$z(q) = \frac{I_2(q) - I_1(q)}{\left(f_2''^2 - f_1''^2\right)} \text{ for } f_1' = f_2' \quad \ldots\ldots. (7.11)$$

The cross term can be extracted by means of choosing a third energy with an equal value of *f''* to the second.

$$y(q) = \frac{I_3(q) - I_2(q) - \left(f_3'^2 - f_2'^2\right)z(q)}{2f_0\left(f_3' - f_3'\right)} \text{ for } f_2'' = f_3'' \quad \ldots. (7.12)$$

The plot in figure 7.5 shows how energies may be chosen to ensure the conditions of equations 7.11 and 7.12 are met. The first two energies, *E1* and *E2* would sit within the resonance at opposite sides of the absorption edge, meeting the requirements of equation 7.11. The third energy, *E3*, is chosen so the *f''* factors of *E2* and *E3* are the same. The normal term can then be solved by inserting the cross and resonant terms back into equation 3.2. A fourth SAXS measurement, taken at an energy far below the absorption edge, can be used as a comparison in searching for contrast features.

Despite the apparent advantage in completing an ASAXS investigation in this way, contributions from fluorescence and Resonant Raman Scattering need to be considered and accurately subtracted before the above equations can be solved. The two energies within the resonance would also be more susceptible to monochromator fluctuations, resolution, and potential chemical shifts. In principle it would be possible to take measurements at regular intervals across the entire width of the resonance, after the motion of the edge with time has been resolved. Samples with a very high concentration of resonant scatterers would also produce a fluorescence signal which floods above edge scattering features.

Such an experimental set up would be more suited for ASAXS investigations where the percentage of resonant scatterers in the sample is small.

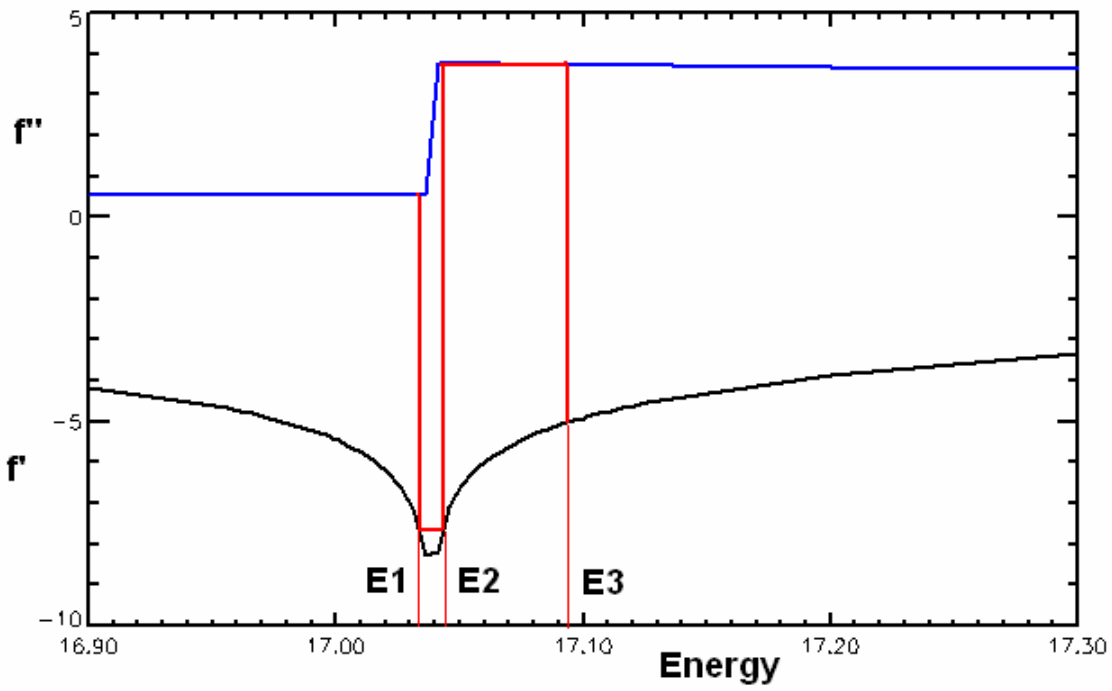

Figure 7.5 *Three energies are chosen so that the factors f' are identical in E1 and E2, and f'' are identical in E2 and E3.*

7.5 Fine tuning 'f prime' – An iterative approach

Provided the concentration of resonant scatterers in the sample is known, a constraint can easily be applied by considering the relation given in chapter 3, (equation 3.1)

$$I(q) = Nr_e^2 \Delta\rho^2 V^2 \left|F(q)\right|^2 S(q) \quad \ldots\ldots 3.1$$

Integrating with respect to q,

$$\int I(q)dq = Nr_e^2 \Delta\rho^2 V^2 \int \left|F(q)\right|^2 S(q)dq \quad \ldots. 7.13$$

Equation 7.13 implies the area and intensity of the curve swept by a scattering function is proportional to the number of particles. In the case of ASAXS, where the normal, cross and resonant terms are three partial scattering functions, each will have their own respective equivalent of the constant, *N*. For the normal term, this is just the number of particles within the sample being scattered by the beam, for the resonant term, it is the number of absorbing particles (resonant scatterers). The cross term, being related to the scattering contribution between a resonant and non-resonant scatterer, has an intensity which also depends on the number of resonant scatterers.

Assuming the total number of particles in the sample to be *N*, the ratio of integrated intensities between the normal and resonant, and normal and cross terms, can be considered as equal to the percentage concentration (number density) of resonant scatterers.

$$\frac{\int z(q)dq}{\int x(q)dq} = \frac{N_r}{N} = \rho_r \quad \text{.... (7.14)}$$

$$\frac{\int y(q)dq}{\int x(q)dq} = \frac{N_c}{N} = \rho_r \quad \text{..... (7.15)}$$

Here, ρ_r is the concentration of the resonant scatterers, which can be considered a molar percentage.

Equations 7.14 and 7.15 are true when the scattering functions are integrated over all *q*-space. Experimentally, it is not feasible to possess a detector capable of such measurements, since such a detector would need to cover the interior of a large hemisphere, with ultra high pixel resolution. At large *q*, small angle scattering functions tend to zero, so as an approximation, the average intensity of the scattering function may be considered as proportional to the integral. Experimental procedure also makes it impossible to measure at *q=0* due to the intensity of non-scattered beam, this must also be considered when determining the average intensities.

For determining the correct normal, cross and resonant terms, equations 7.14 and 7.15 give our first constraint:

The ratio of average intensities between the normal and resonant, and normal and cross terms must be equal to the concentration of resonant scatterers.

The discussion in section 7.3 already provides a template for the second constraint.

Expanding the concepts already covered in section 7.3, variations in the *f'* values for both the second and third energy using a single, averaged value for the intensities of three scattering functions, generates a topology in *f'* space. The correct solution, in which the normal, cross and resonant terms are of the correct intensities, is demonstrated by a global minimum. Solutions are determined by the square of the difference between the concentration of resonant scatterers and the ratio of integrated (average) intensities of the

resonant and normal terms. The correct solution will lie in the region where the squared difference is equal to zero.

$$\left(\frac{\left| \int z(q)dq \right|}{\left| \int x(q)dq \right|} - \rho_r \right)^2 = 0 \ldots. (7.15)$$

Similar results may be obtained for the cross term.

$$\left(\frac{\left| \int y(q)dq \right|}{\left| \int x(q)dq \right|} - \rho_r \right)^2 = 0 \ldots. (7.16)$$

The two relations, 7.15 and 7.16, each contain multiple solutions described by a small ring in *f'* space; the radius of which marks the region where the integrated intensity is less intense than the concentration of scatterers. The two functions can be combined to give a χ^2 (chi square) relation. The rings should then touch to give a single, central solution true for the equations when $\chi^2 \rightarrow 0$ at the point of contact. The functions are summed rather than subtracted to enhance the amplitude of the topology.

$$X^2 = \left(\frac{\left| \int y(q)dq \right|}{\left| \int x(q)dq \right|} - \rho_r \right)^2 + \left(\frac{\left| \int z(q)dq \right|}{\left| \int x(q)dq \right|} - \rho_r \right)^2 \ldots.. (7.17)$$

A second constraint may be included by considering the initial choices in energy as a distance from the absorption edge. Typically, chosen energies will have two within the absorption resonance and one far below. The two within the resonance will be the most prone to errors due to monochromator resolution and fluctuations. The value of *f'* for the off edge energy can be assumed to be constant.

Figure 7.6 reveals the variations in intensity of the resonant term as the two values of *f'* close to the edge are varied using the relation in equation 7.15. The actual (true) solution is marked by a red dot, the solution evaluated from incorrect *f'* during experiment is pointed to by the red arrows. Monochromator resolution, beam spectrum, and associated errors with the beam-line drive motors; the actual energy used, and hence the calculated values of *f'* for this particular ASAXS cycle, may sit within the region outlined by the green square.

The margin of errors associated with monochromator positioning uncertainties then give a second constraint.

Changes in f' cannot fluctuate more than the associated monochromator resolution and movement error.

Using this constraint, a fitting routine can be applied which will allow variations in energy, and hence *f'* only within a certain margin. This prevents other, erroneous solutions occurring where f'_2 becomes greater than f'_3 (for the case where energies are chosen so *E3* has the largest *f'*). The green square outlined in figure 7.6 thus shows the

region within which *f'* is allowed to vary in searching for a correct solution, which as shown also dwells inside the region.

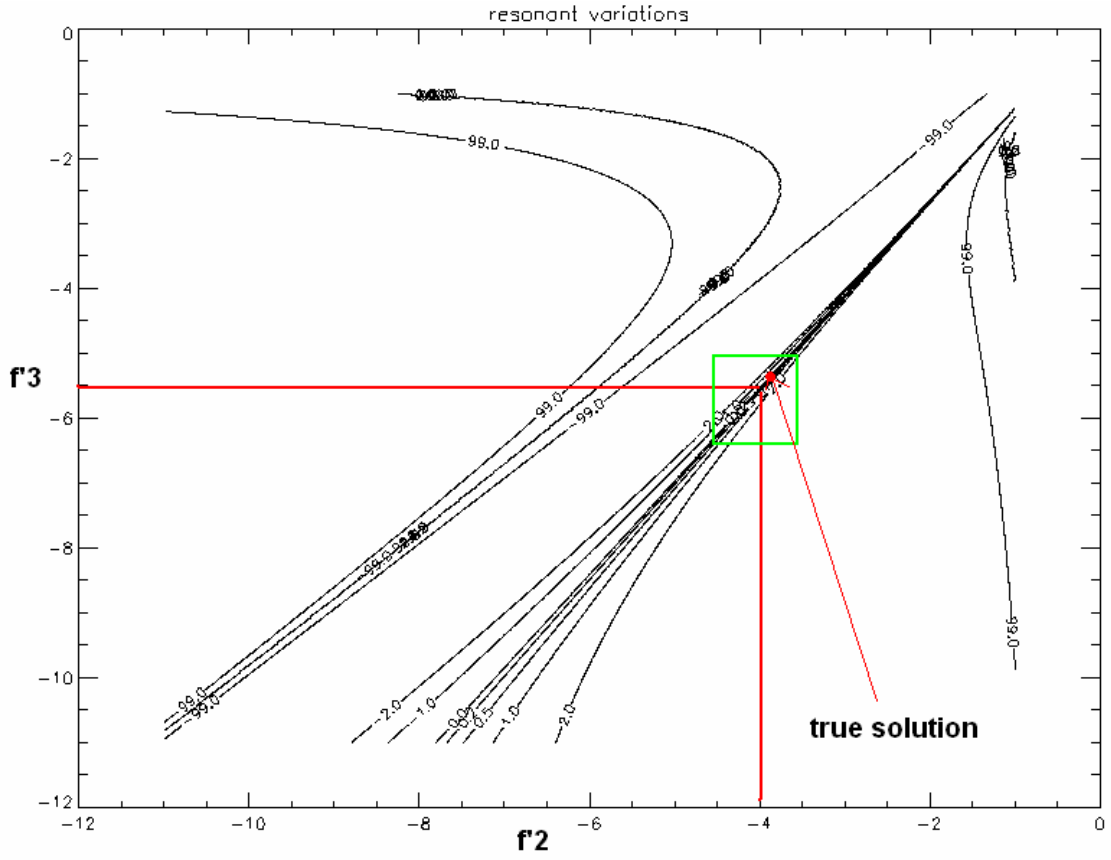

Figure 7.6 *Variations in average intensity of the resonant term as a function of f' for the two near edge energies. The red lines point to a potential solution that may have been calculated from experimental data, while the red spot indicates the position of the true solution due to a uncertainties in monochromator positioning, which causes a slight change in beam energy for that cycle. If the uncertainty and resolution are known, the true solution can be found by tuning f' to values within the green square (the region of error) to find the correct solution for the resonant term.*

With the two constraints in mind, the relation given by equation 7.17 can be applied to an iterative procedure to converge on the true solutions of the normal, cross and resonant

terms. Inclusion of the intensities of all three terms also negates the potential of multiple solutions occurring, provided the following additional constraint and check is carried out:

The normal, cross and resonant terms must have positive intensity for all q.

Mathematically, an integrated function is the area beneath the curve. If part of that function becomes negative, than that integrated section will also be negative. By just considering the first two constraints, it is possible that alternate solutions may arise that show a resonant term of the correct integrated (or averaged) intensity, but also possessing regions of negative intensity. The inclusion of the integrated normal term, $x(q)$, in equation 7.17 will generally minimise this effect since the intensities of the normal and cross terms will change significantly from their true values should this case arise.

The inclusion of the third constraint is thus an extra check to ensure the iteration procedure has not fallen into a local minimum.

Chapter 8

Results and Discussion

Results are presented from experiments performed at beamline 6.2, Daresbury, and beamline I22, Diamond Light Source Ltd. The gelation process is first presented, with the stabilised zirconia and zinc-silica systems as separate sections. The results of both gelation processes are then discussed.

The sintering of yttria stabilised zirconia is then presented. The results are obtained after conducting a time resolved double ASAXS experiment at beamline 6.2, Daresbury. Double ASAXS involves the study of a material across two absorption edges in a single experimental run. A comparison of results obtained from X-ray diffraction (XRD) performed at the Materials Physics Laboratory, Aberystwyth University, is given towards the end of the sintering section.

8.1 The Gelation Process

8.1.1 Stabilised Zirconia

Figure 8.1 shows the raw data for the gelation of a typical Zirconia, YSZ and YSZ-Si sol at beamline 6.2, Daresbury. The scattering functions are those obtained from the lowest energy in each cycle (ie, below both absorption edges) before any contrast variations

occur. The three systems show near identical scattering functions as gelation proceeds. The time resolved SAXS patters shown are those obtained from a X-ray photon energy of 16.8 keV – far below the absorption edges of yttria and zirconia. The alkoxide precursors (b) are slowly hydrolysed resulting in the scattering function for the sol (shown in figure 8.1 c). As gelation proceeds, an increase in intensity of the regions below q=1 is observed.

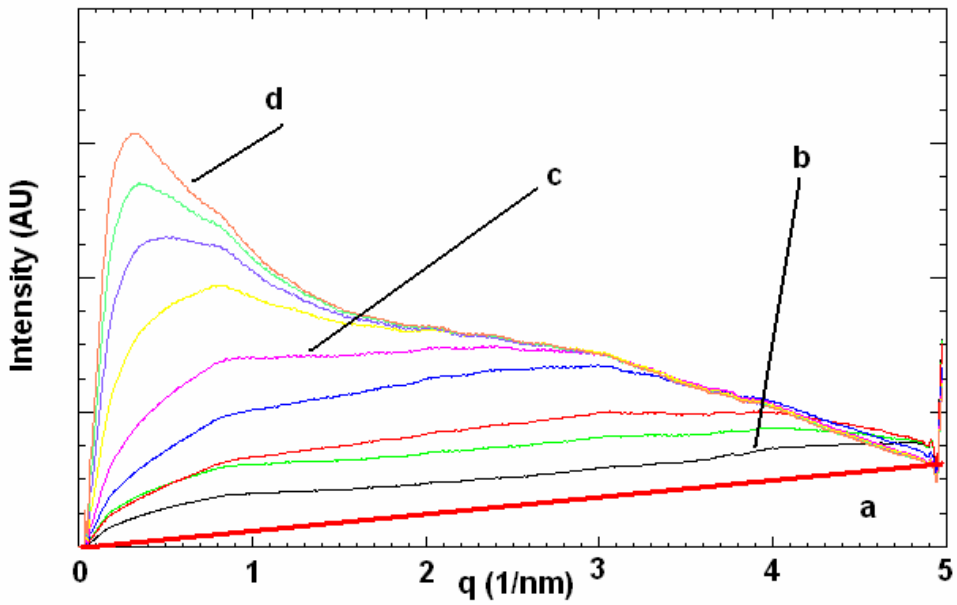

Figure 8.1*: Raw, non radial-averaged, SAXS patterns of the gelation of typical YSZ and YSZ-Si sols. Radial averaging is first performed by subtracting the function described by region (a) (see chapter 6). The initial precursor material (b) is slowly hydrolysed to obtain a clear sol (c). Gelation is revealed by the growth of the low q region (d). This form of scattering is typical for both YSZ and YSZ-Si sols as they gel.*

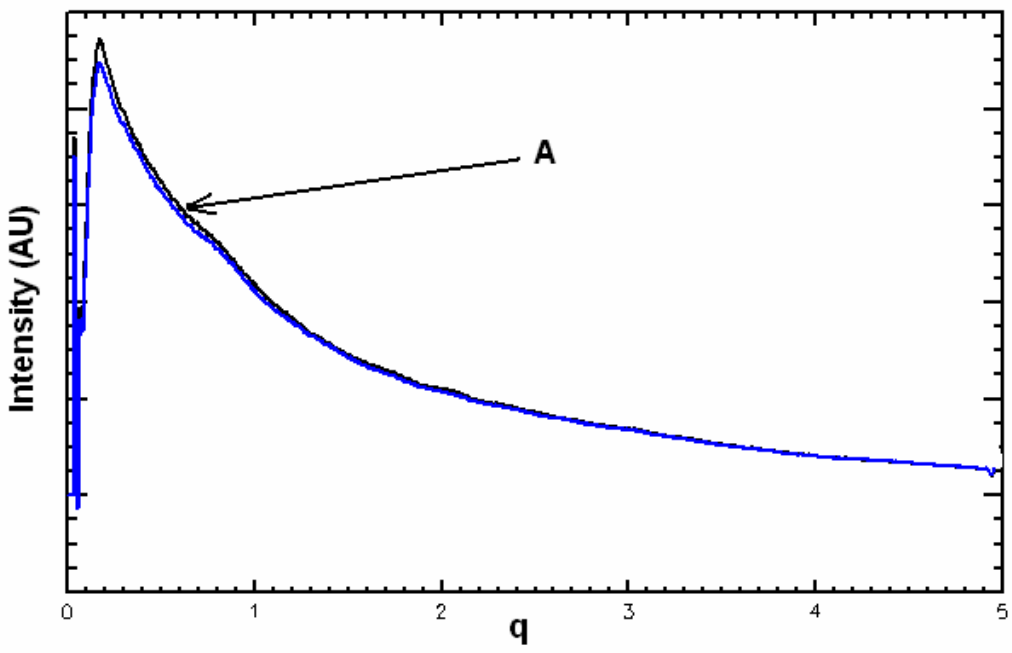

Figure 8.2: *Comparison of the scattering functions obtained for a YSZ-Si gel taken at 3eV (blue) and 27eV (black) below the zirconium absorption edge. Subtle differences in the form of the scattering pattern are observed in the region highlighted by 'A'.*

Comparisons of the energies close to the zirconium absorption edge reveal slight variations in the shape of the scattering function (figure 8.2) for YSZ-Si systems. The subtle differences are enhanced by subtracting one function from the other to reveal contrast variation in the lower q regions which is most intense prior to gelation (figure 8.3), which then becomes less intense as the gelation proceeds. The contrast is limited to the lower q region (below q=1.5 nm^{-1}) with identical shapes in the scattering functions for larger q.

Figure 8.3 shows the difference between scattering patterns at energies taken at -3eV and -27eV below the zirconia edge for YSZ-silica gel. The black curve indicates the difference between functions just after hydrolysis, while the green and red curves represent the differences in scattering functions close to and after gelation respectively.

A similar analysis performed on pure YSZ gels revealed no scattering contrast between functions (ie, the normal, cross and resonant terms were equal in form for the entire gelation stage).

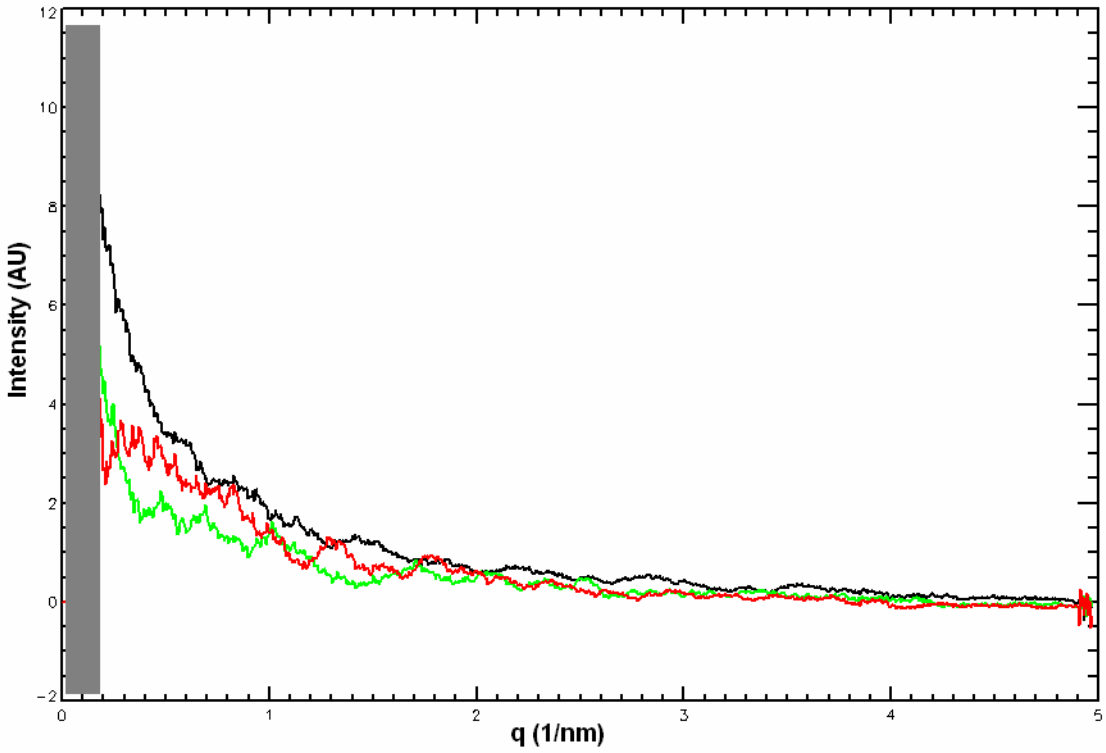

Figure 8.3 *The difference between scattering functions for the two near edge energies on the zirconium edge. The contrast is most intense after hydrolysis (black) and slowly decreases in intensity during the gelation stage (red) and remains present even after gelation (green).*

Applying the deconvolution method using experimentally derived results from the Kramers Kronig function indicates the contrast is dominant in the resonant term (figure 8.4). The normal term reveals a Porod slope of 1.67; while the Porod gradient of the resonant term is 2.16, which close to the fractal dimension of pure zironia (2.35) [78]. The patterns remained a constant shape for all times during the gelation process. By

comparison, across the yttrium K edge, the normal, cross and resonant terms are of similar form throughout the experiment, and do not show similar features in the resonant term as compared with zirconium ASAXS.

Attempts at extracting the partial scattering functions for the pure YSZ gels reveal identical patterns for the normal, cross and resonant terms for the two absorption edges. In both cases, for YSZ with and without silica, varying the quantity of yttria does not make any visible changes to the contrast variations.

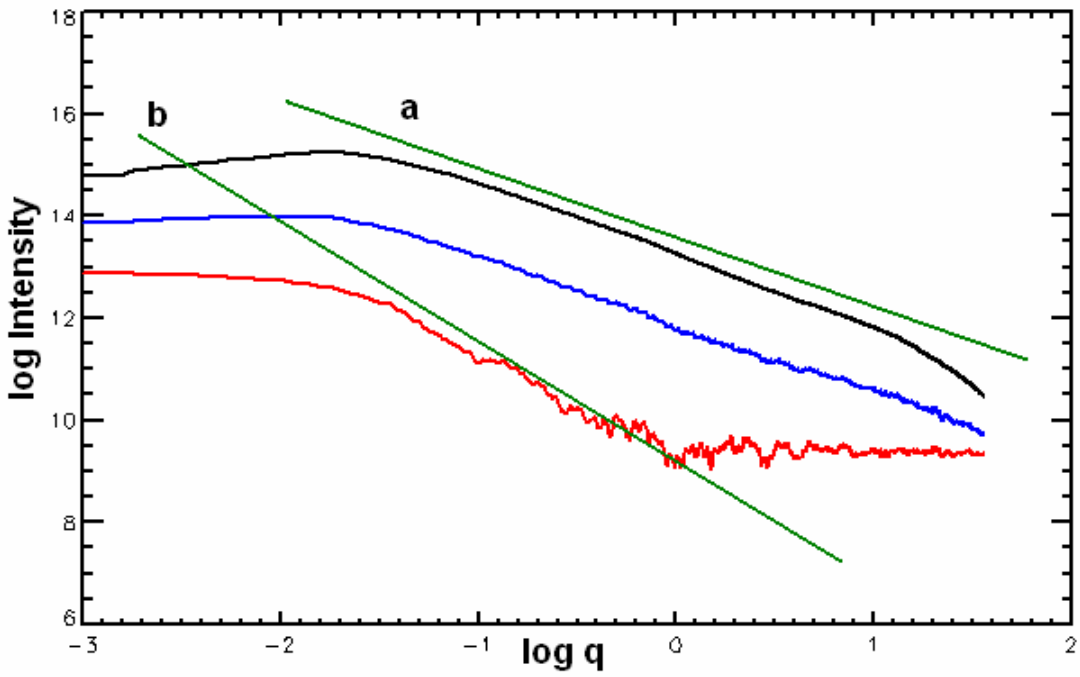

Figure 8.5*: The normal (black), cross (blue) and resonant (red) scattering patterns of yttria-stabilised-zirconia gel in silica. Contrast is revealed in the resonant term by a change of gradient (*log q =-2 *to* log q =0*).. The green lines a and b are a schematic of the linear fits used and the regions of the scattering functions measured.*

8.1.2 Zinc-Silica gels

The quadrant plot in figure 8.6 shows the radially averaged normal, cross and resonant terms at different points in time during the gelation of a zinc-silica sol. After hydrolysis, a gel network begins to form, creating a viscous sol. The network further expands until the material is fully gelled (figure 8.6, bottom right). Most noticeable is the change in gradient of the mid-q range prior to gelation, visible in both the cross and the resonant terms (figure 8.6, top right and bottom left). The partial scattering functions are of similar form to that of the initial sol, shown in the top left of the figure.

Table 1 shows the magnitudes of the gradients of the mid q regions ($-2.7 < \log q < -1.7$) taken from the four log-log plots given in figure 8.6. The gradient for all three terms is 2 prior to hydrolysis. During gelation, the gradient of the normal term drops to 1.17, while the cross and resonant terms show a slight increase in magnitude. A difference in gradients is also revealed at different stages of network formation, with the resonant term shifting from 1.83 to 2.67, and the cross from 1.83 to 2.28, before both terms become identical in form to the normal when the sample fully gels. After gelation has occurred, the mid-q gradient of all three terms becomes 0.83.

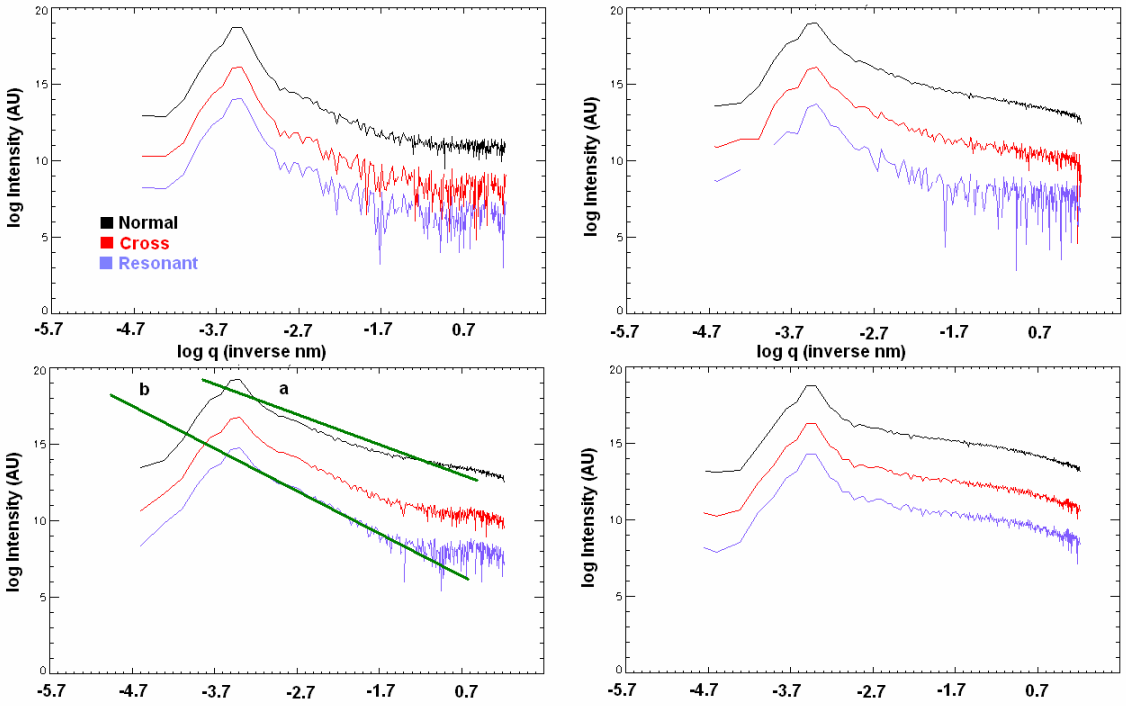

Figure 8.6: *The contrast variation between the normal (black), cross (red) and resonant (blue) terms during the gelation of a silica-zinc sol. The initial liquid precursors (top left) begin to form a viscous sol as gel networks form (top left, bottom right). Bottom right; the material is fully gelled. Contrast visible in both the cross and resonant terms is present during network formation (top right, bottom left). A schematic of the fits to the gradients is shown bottom left (lines a and b) for visual clarity, and to show the difference between the normal, and the cross and resonant terms.*

Time (mins)	Normal	Cross	Resonant
0	2.0	2.0	2.0
20	1.17	1.83	1.83
30	1.17	2.28	2.67
60	0.83	0.83	0.83

Table 8.1: *The gradient of the mid-q region for the normal, cross and resonant terms during the gelation process.*

8.1.3 Discussion of the gelation process

Comparisons between the stabilised zirconia and zinc-silica gels reveal the dominating presence of contrast in the resonant term for the YSZ, which remains a constant shape throughout the gelation process. Contrast, which is also present in the cross term of the zinc systems, is only visible during gel-network formation in the zinc-silica gels.

The results indicate that both zirconia and yttria primaries become part of the gel network, due to their higher coordination states, and since contrast is only present in the resonant term. This contrast is caused by three possible linked combinations. If atom A is the resonant scatterer, and atom B is a non-resonant, and they are both network formers, links may form by three possible combinations; A-A, A-B and B-B.

The slightly higher fractal dimension present in the resonant term of the Si-YSZ gels also indicates zirconia-zirconia linking as well as zirconia-silica and silica-silica, due to the higher coordination state of zirconia. As described in chapter 1, the addition of a chelating agent will saturate a transition ion to its highest coordination number, which in the case of zirconia is 6. Silicon is a tetrahedral ion of coordination number 4. [79]

For zinc-silica systems, contrast is visible in both the resonant and the cross terms, indicating slight inhomogeneities on the nano-scale between zinc-zinc and zinc-silica interactions respectively. As seen from the zirconia systems, a resonant scatterer integrated in the network makes the network appear ‘homogenous’ in the view point of the cross term, and therefore identical to the normal (conventional SAXS) pattern. In the case of the zinc systems contrast, with identical cross and resonant terms, indicates the

resonant scatterers are not being integrated into the gel network and remain trapped within pores. This implies the silica gel matrix forms at the exclusion of zinc. The zinc itself remains in the sol where it eventually becomes trapped within gel pores as zinc oxoacetate primaries.

Though these are quantitive deductions based on the results obtained from ASAXS, further work needs to be performed to fully test this hypothesis. Proposals for future work are outlined in the final part of this thesis (chapter 9, section 4).

8.2 Analysis of the Sintering of Sol-Gel Prepared Yttria-Stabilised-Zirconia using Time Resolved Double ASAXS.

Pre-prepared yttria stabilised zirconia (YSZ) and YSZ in silica gels are analysed using anomalous small angle scattering across both the yttrium and zirconium absorption edges.

8.2.1 Time resolved (Single Energy) SAXS

The growth of a scattering factor maximum (hump) is observed using time resolved SAXS, using a beamline energy set to below the absorption edges of both yttrium and zirconium. Figure 8.7 shows the effect of the scattering function with increasing temperature. The scattering factor maximum, shown in the scattering pattern by a hump, moves to lower q and increases in intensity.

The position of the maximum in *q* space is plotted for different samples in figure 8.8. The figure shows a clear distinction between samples of pure YSZ, and those with YSZ in a silica matrix. The addition of silica (added in the form of TEOS in the sol-gel) slows the growth of the maximum, and only becomes more apparent when temperatures are in excess of 780°C. Subsequent samples with varying yttria content do not show changes in the rate of formation of the hump (also shown in figure 8.8.)

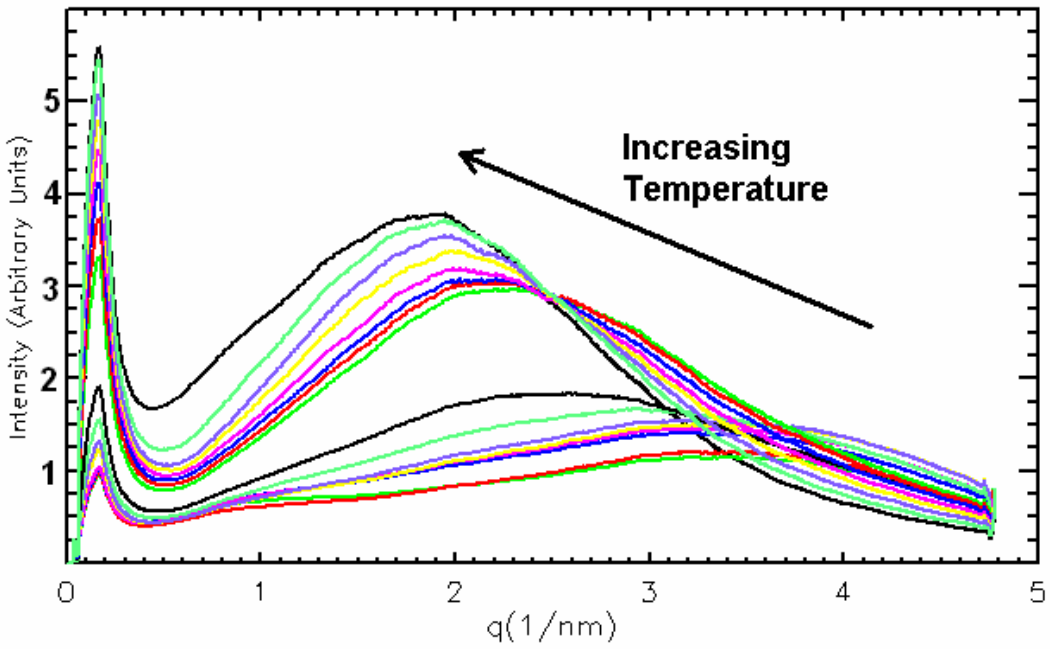

Figure 8.7. *Normal In situ SAXS revealing the growth of a scattering factor 'hump' during the sintering of a sol-gel derived yttria stabilized zirconia ceramic with 5.6 mol% yttria in air. The feature moves from right to left, and increases in intensity as the temperature is increased from 100 to 700°C. The margin of error in intensity is* $\Delta I/I = 2.4*10^{-3}$.

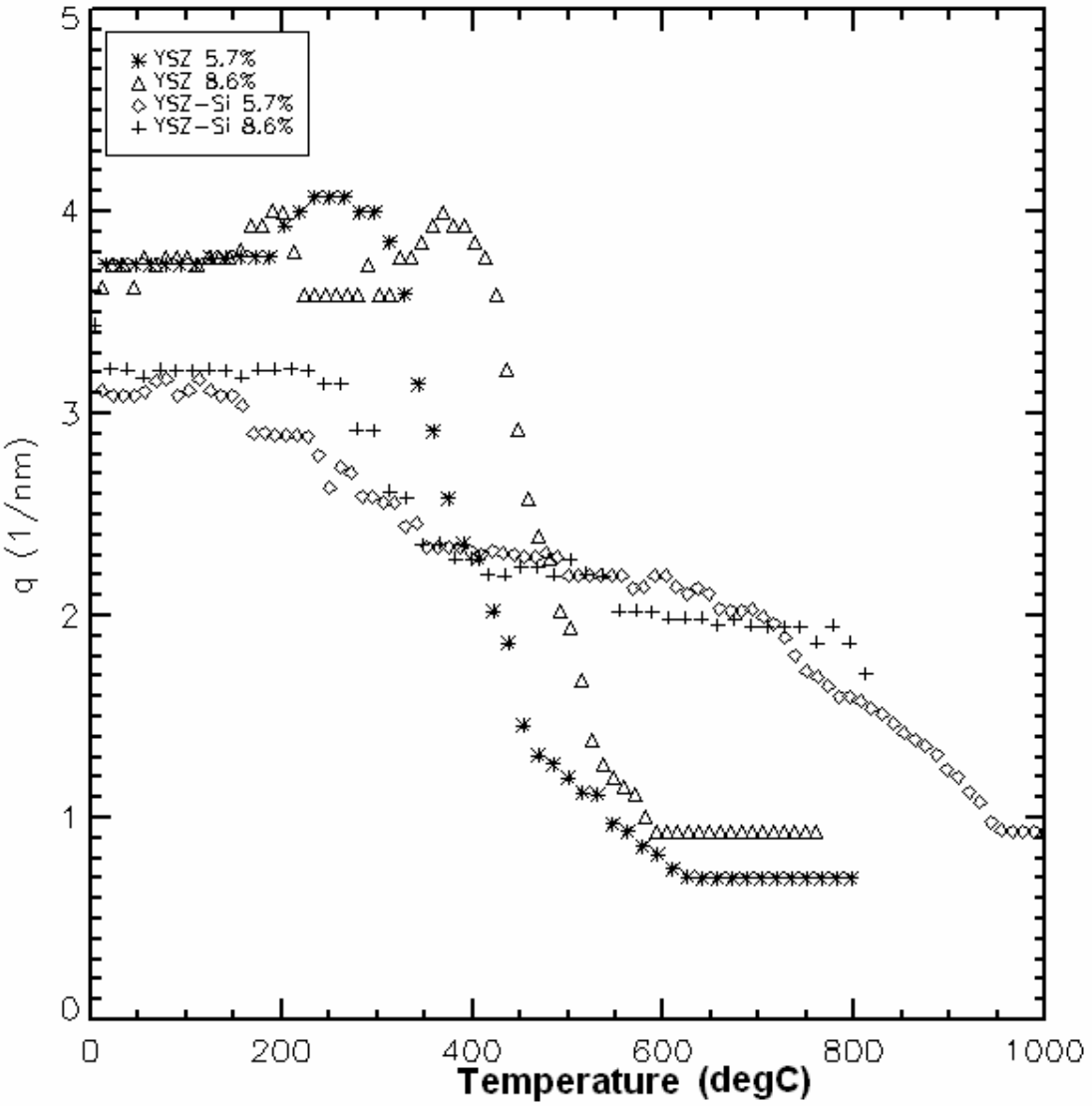

Figure 8.8*: The position of the peak of the structure factor maximum on the q scale as a function of temperature (°C). The addition of silica (crosses and diamonds) increases the nucleation temperature, in comparison to straight YSZ (stars and triangles), which nucleates at just below 400°C. The YSZ and YSZ in silica samples contain 5.7 and 8.6 mol% yttria.*

The scattering factor maximum is attributed to the nucleation and growth of nano-sized tetragonal and cubic YSZ crystals, as has already been described in similar systems [80,81,82]. These crystals swell rapidly, until the individual sizes are outside of the *q*

window. The initial hump seen in all samples near q=4 nm^{-1} is probably caused by pores in the compressed xerogel that slowly shrink due to the combustion of organic matter in air. Scattering functions of pure YSZ samples show a rapid growth of the maximum after 380°C. For those in the presence of a silica matrix crystal growth is gradual; this growth rate increases when temperatures are above 780°C.

8.2.2 Anomalous (energy dependent) effects

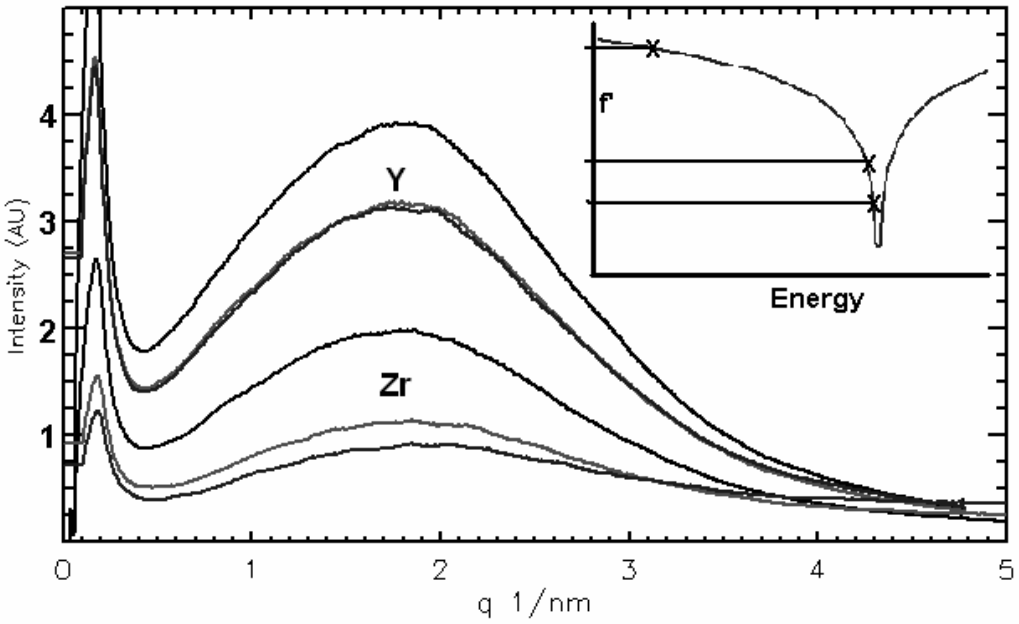

Figure 8.9. *The scattering patterns at six energies; three near the yttrium K edge, and three near the zirconium K edge. Shown here are the scattering functions for YSZ in a silica matrix, heated to 900°C. The anomalous effects are seen as a decrease in overall intensity as first the yttria, and then the zirconia absorbs the X-ray beam; and a broadening of the scattering factor maximum close to the zirconium edge. The insert schematic shows the relative positions of the chosen X-ray energies around an absorption edge, with two being within the minimum (-3 eV and -8 eV) with one far below the edge (-300 eV). This method is followed for both the yttrium and zirconium edges. ($\Delta I/I=2.4*10^{-3}$). (Fluorescence and Resonant Raman Scattering contributions are subtracted using large angle WAXS measurements).*

The results in figure 8.9 show the anomalous effects observed for a sol-gel derived YSZ ceramic at a temperature above the nucleation point, and reveal a decrease in intensity and broadening of the maximum as energies approach the zirconia K edge for a given, fixed temperature. This broadening is the contrast close to the zirconium edge, and indicates that zirconia has the dominant role in the formation of YSZ.

Taking the Porod slopes of the log-log plots (the exponent α) reveals noticeable changes for energies below the zirconium edge, as well as a difference in gradient between those energies on or close to the edge, compared with those below.

Figure 8.10 reveals a rise in gradient from -4 at the time of nucleation, to between -3.2 and -1.8 for energies at or below the yttrium edge, while results taken from the between-edge energy, and those on the zirconium edge reveal shallower gradients. Those on the zirconium edge, in particular, have a Porod exponent close to zero at the highest temperatures. This is due to X-ray absorption by the dense YSZ crystals, leaving the non-YSZ background as the larger contribution. Below nucleation, the Porod scheme does not apply as the samples are still homogenous xerogels, as opposed to nanoscale particles.

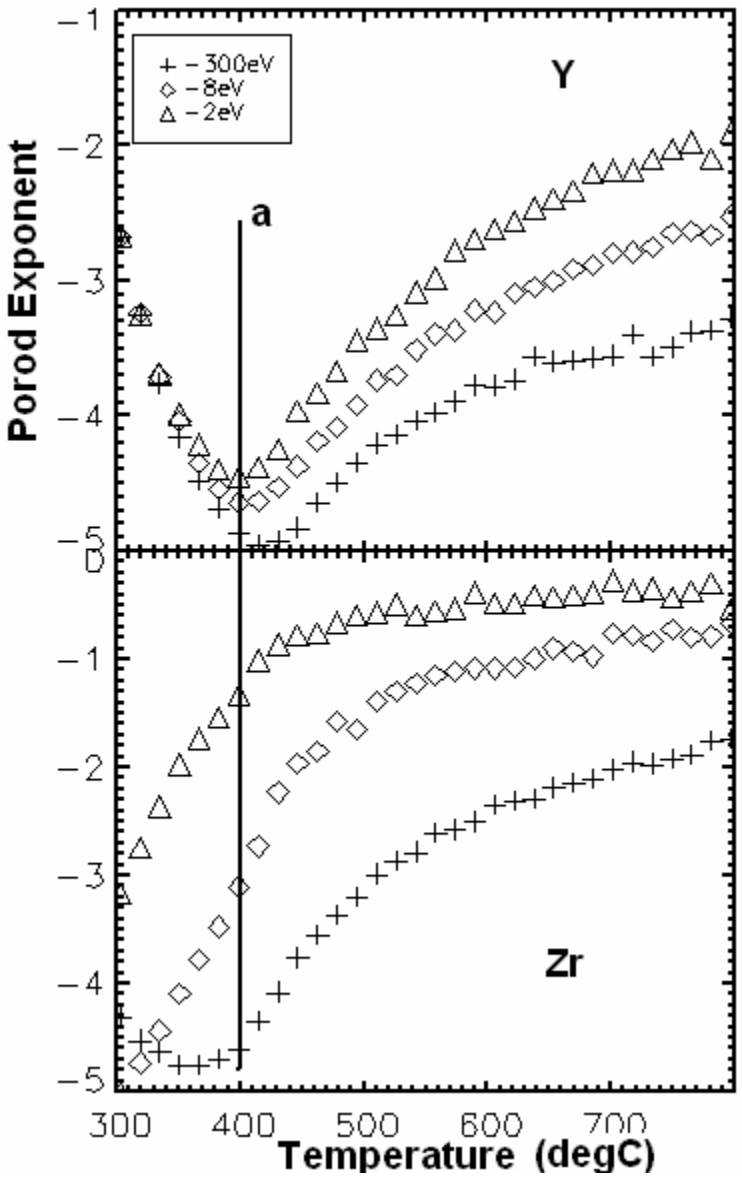

Figure 8.10. *The changes in Porod exponent of scattering patterns around the Y (top) and Zr (bottom) edges during the sintering of YSZ without silica. The nucleation point is clearly visible for energies below the zirconium edge, shown by the vertical line (a). In each case, the triangles represent the energy 300 eV below the edge, with the diamonds and crosses being -8 eV and -3 eV respectively. Porod exponents from energies on the zirconium edge display gradients close to zero.*

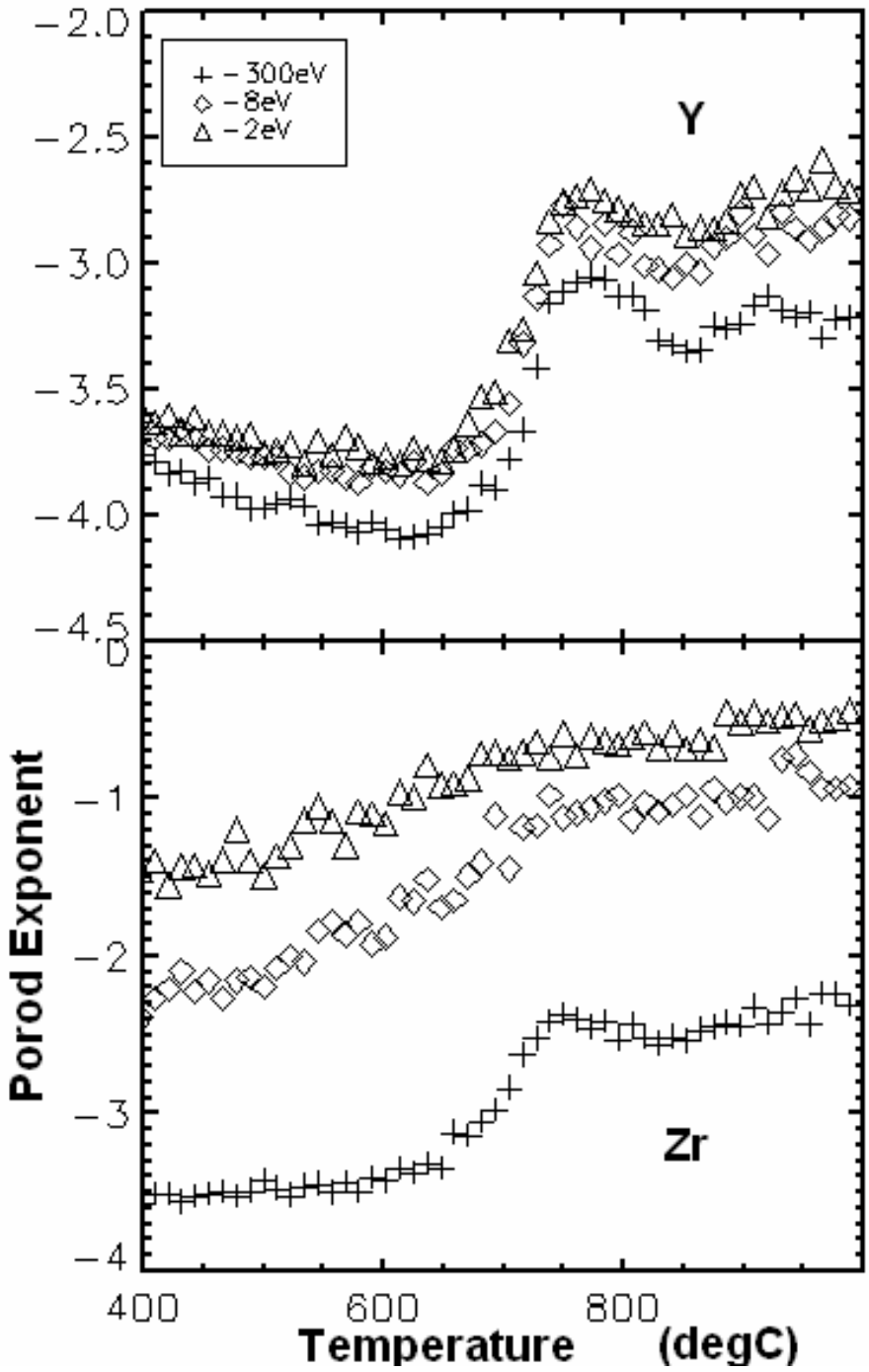

Figure 8.11: *Changes in the Porod gradient of scattering patterns around the Y (top) and Zr (bottom) edges for YSZ in a silica matrix. The nucleation point is much higher than in YSZ without silica (cf. fig. 8.10), visible as a step in the energies below the zirconium edge. The relative edge positions are the same as in figure 8.10.*

By comparison, YSZ in a silica matrix (Figure 8.11) shows a steady gradient of around -4 for each energy until nucleation is about to occur. During this period, gradients below the zirconium edge increase in values of between -3 and -2; shown by the step between 700°C and 800°C in the graphs. Energies on the zirconium edge again show Porod exponents closer to zero, though in this case, the convergences are -0.8 and -0.3 for -3 eV and -8 eV from the zirconium edge respectively. Beyond temperatures of 800°C, wiggles are also seen – particularly on the yttrium edge. This is an indication that yttria is taking part in a second reaction, possibly with the silica matrix itself (see section 8.2.4 for cases of surplus yttria). Further work needs to be carried out to fully explore this cause.

In both cases, the differences in gradient with increasing energy can be explained by the poly-disperse nature of the growing particles. While a gradient of -4 is attributed to a smooth surface, a decrease implies the surfaces are getting rougher with increasing temperature and particle size. The two highest energies, where both yttria and zirconia are highly absorbing, show the Porod background. For straight YSZ, this is air; while for YSZ in silica; the main contribution is the matrix.

8.2.3 In situ ASAXS

Figure 8.12 shows how the three terms of the scattering function evolve with temperature during an *in-situ* experiment of the sintering of yttria stabilised zirconia across the zirconium absorption edge. In addition to scattering from macroscopic objects at low q, a structure factor maximum grows at higher q and moves to the left as temperature increases. While the feature is visible in all three terms, there is a clear

difference in shape between the normal and resonant terms once the temperature reaches 380°C. As the samples are heated further, the resonant term once again becomes identical to the normal beyond 640°C.

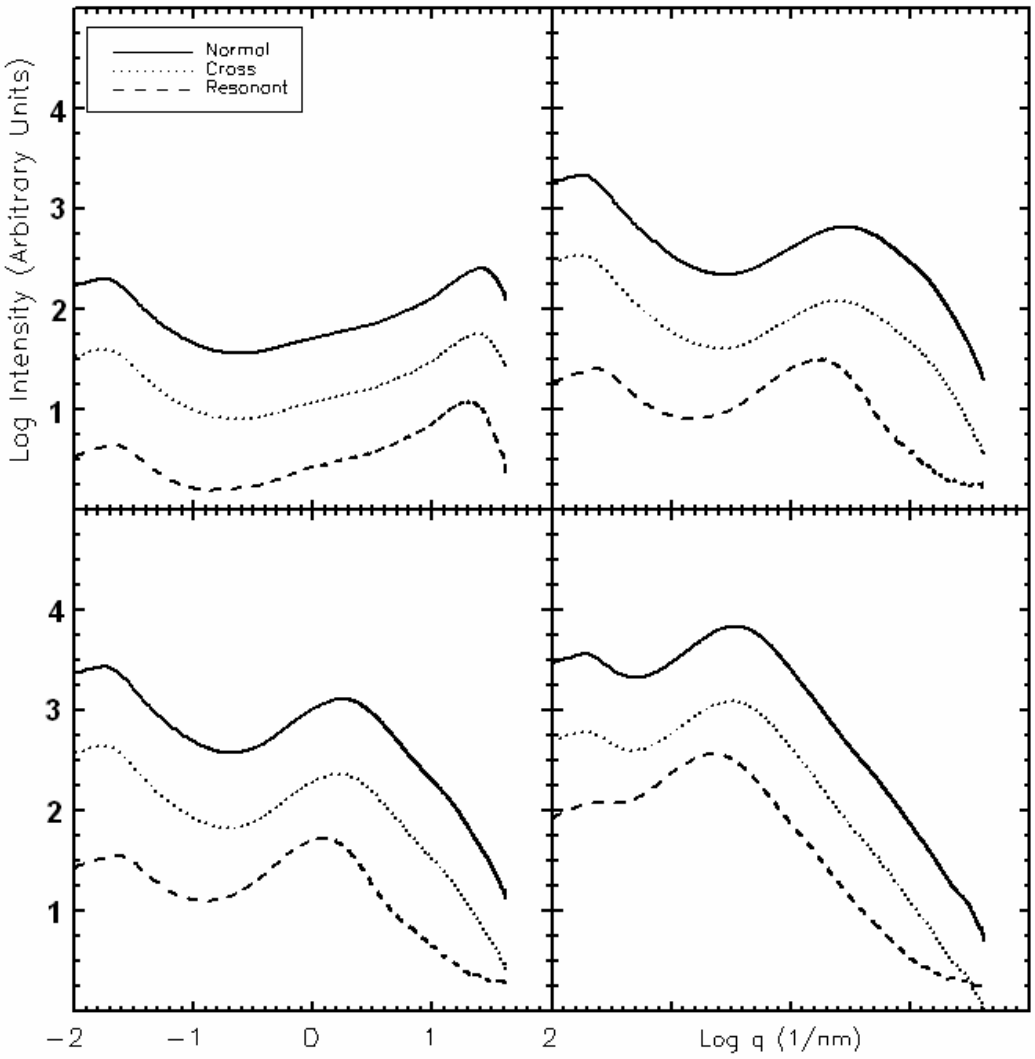

Figure 8.12. *In situ Zirconium ASAXS scattering patterns (log Intensity vs log q) showing the separated normal (continuous line) cross (dotted) and resonant (dashed) scattering contributions. Top left: starting xerogel at room temperature, top right – 380°C, bottom left - 420°C, bottom right - 600°C. The resonant term shows a narrowing during sintering at the intermediate temperatures. At 600°C, the resonant term becomes identical in shape to the normal term again. (ΔI/I is $2.5*10^{-3}$ for the normal and 10^{-2} for the resonant).*

When multiplied by its coefficients (notably *f'*), the cross term will become a negative contribution to the scattering function as energies approach the absorption edge. In figure 8.12, the normal cross and resonant terms have been multiplied by their coefficients, and the sign of *f'* reversed for the cross term for visual clarity.

The difference in width between the normal and resonant terms in *q* space correlates to a distribution in real space. At the nanometer scale, zirconia particles occupy a different region of *q* to that of yttria in the early stages of nucleation (at 380°C). Nucleates then grow with further heating, forcing the zirconia clusters to incorporate the yttria primaries - increasing homogeneity. Patterns in which the normal, cross and resonant terms are identical in shape (though differing in intensity) are an indication of a 2-phase mixture of homogeneous YSZ and air at the nanoscale.

8.2.4 Surplus Yttria

Anomalous scattering from high yttria to zirconia ratios indicate the presence of a saturation point, beyond which pockets of surplus yttria will begin to form, which yttrium ASAXS (edge at 17keV) is able to resolve in the resonant term (figure 8.13, left). In the presence of TEOS, yttria will react with the silica matrix at temperatures over 900°C to form silicates. This effect is shown in the left half of *figure 8.13* as a smaller feature to the right of the main scattering factor maximum in both the normal and resonant terms. The smaller feature, at higher q, indicates the formation of small features – which could be the onset of yttrium silicate nucleation. Further work needs to be performed to investigate this additional reaction.

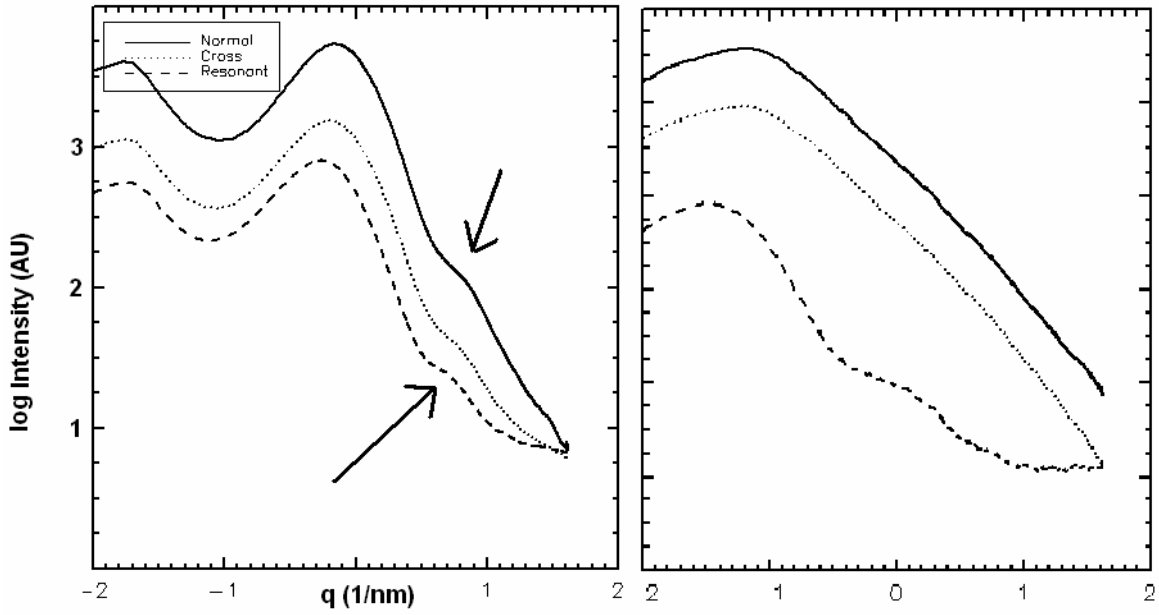

Figure 8.13: *In-situ ASAXS scattering patterns taken across the yttrium edge (log intensity vs log q) of a YSZ sample with higher concentration of yttria (Y/Zr = 15 mol%) at 920°C, showing the separated normal (continuous line) cross (dotted) and resonant (dashed) scattering contributions. Left: YSZ in silica matrix, right: YSZ without matrix. Both normal and resonant terms show an additional feature at larger q in the case of YSZ in silica matrix, while for a matrix free YSZ, the feature is only resolved in the resonant term. ($\Delta I/I=2.5*10^{-3}$ for the normal. $\Delta I/I=10^{-2}$ for the resonant)*

8.2.5 Contrasts between the normal and resonant terms: the role of yttria and zirconia

Comparisons of the results have revealed some interesting differences between the normal and resonant terms. Gaussian fitting using IDL was applied to the scattering factor maxima, and their half widths and position in q space measured. These values of q were then converted to length scales using the relation in eq. 8.1. The resonant term

shows a lower q range and narrowing of the scattering factor maximum, which is described as a larger correlation length. In the cases of YSZ with and without silica, the size distributions diverge with increasing temperature and hence can be a measure of an increase in average particle size. These effects can be seen in Figure 8.14. Results also reveal the presence of silica also decreases the size distribution range for a given correlation length.

$$L = \frac{2\pi}{q} \quad (8.1)$$

On a sub-nanometre level, the results are interpreted as zirconia playing the dominant role, incorporating yttria into the lattice as the crystals grow. This is a thermally driven reaction where zirconia primary particles drift through the less dense medium (if a silica matrix is present) and coalesce to form nano-sized tetragonal crystals. The inclusion of yttria in the growing crystalline structures induces a cubic phase transition [83].

An increased correlation length and wider distribution with a given temperature in the resonant term can be caused when there are larger pure zirconia crystals. Pure zirconia particles nucleate first, some of which absorb yttria to produce the smaller YSZ particles visible in the normal term. Silica, itself densifying with increasing temperature, slows the thermally driven motion of the zirconia primaries, resulting in smaller crystals and lower size distributions for a given temperature. A cartoon to show this process is given in section 8.2.7.

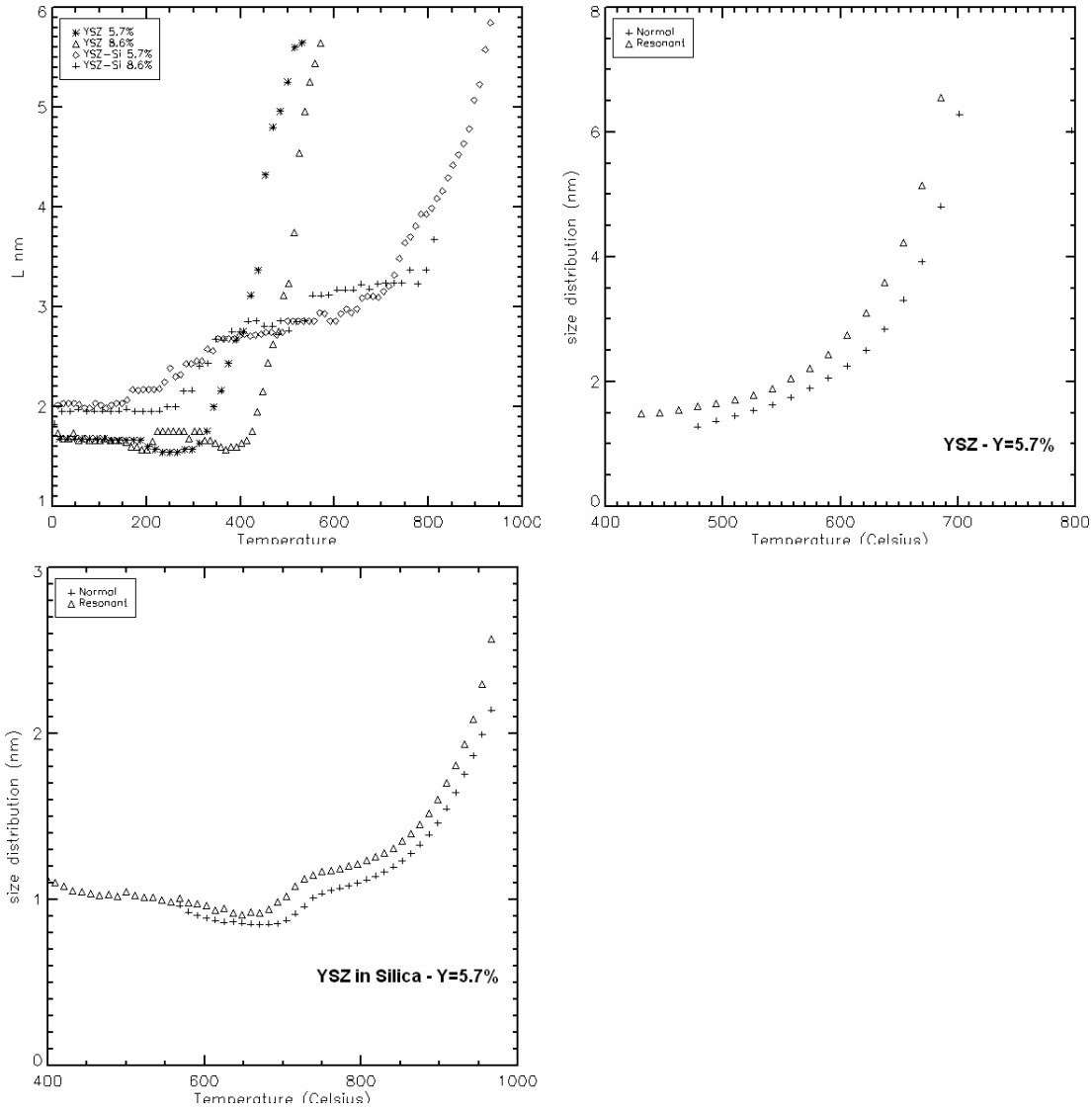

Figure 8.14: *Top left shows the correlation length (L) with temperature for YSZ samples with and without a silica matrix. Pure YSZ (stars and triangles) shows a rapid growth just after nucleation. The plot to the top right displays the half width of the structure factor maximum for the normal and resonant terms for YSZ as temperatures are increased. A similar plot (bottom) is shown for YSZ in silica. The presence of a silica matrix narrows the length distribution range to a couple of nanometers at 1000 degrees Celsius. (Percentages are in terms of mol%)*

8.2.6 Comparative results from wide angle X-ray diffraction

In addition to *in situ* ASAXS, ex-situ experiments were performed on the same samples using X-ray diffraction (XRD) in the materials laboratory, Aberystwyth University. Samples were heated in a furnace in 50°C steps, and X-ray diffraction was carried out once the sample had cooled to room temperature. Bragg peak formation does not commence until sintering temperatures reach 400°C for pure YSZ, *(figure 8.12 top)*. For pure zirconia, quenching reveals a tetragonal-monoclinic phase transition when the original baking temperatures exceed 500°C (*figure 8.16 bottom*). Particle sizes are estimated by measuring the half widths of the growing Bragg Peaks and applying the Scherrer equation[85] (figure 8.15). Results of this investigation are found to compare with those obtained from ASAXS.

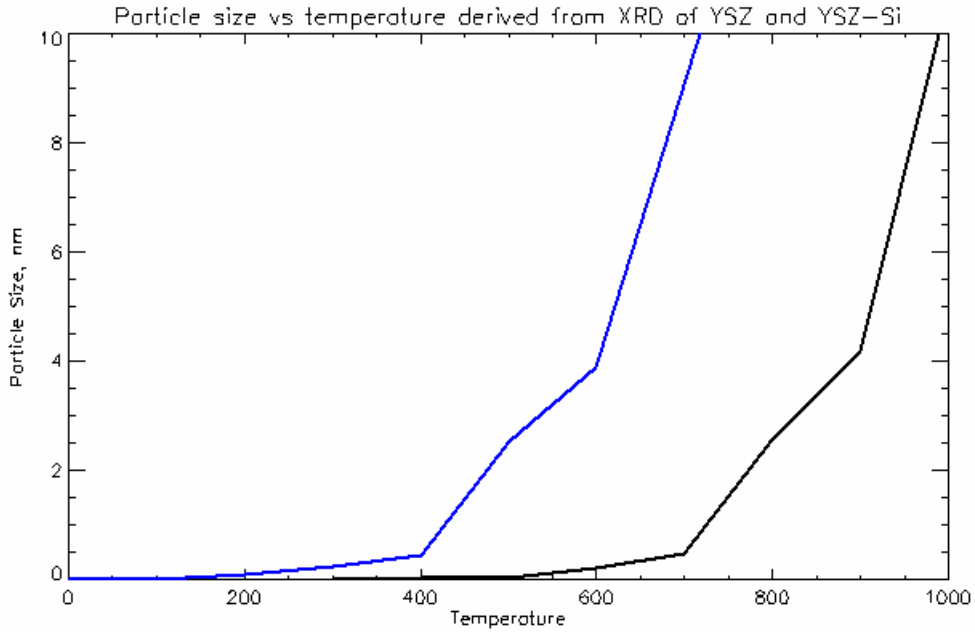

Figure 8.15*: Estimates of particle sizes with temperature measured using XRD. Blue, YSZ, grows much faster than its counterpart in silica (black)*

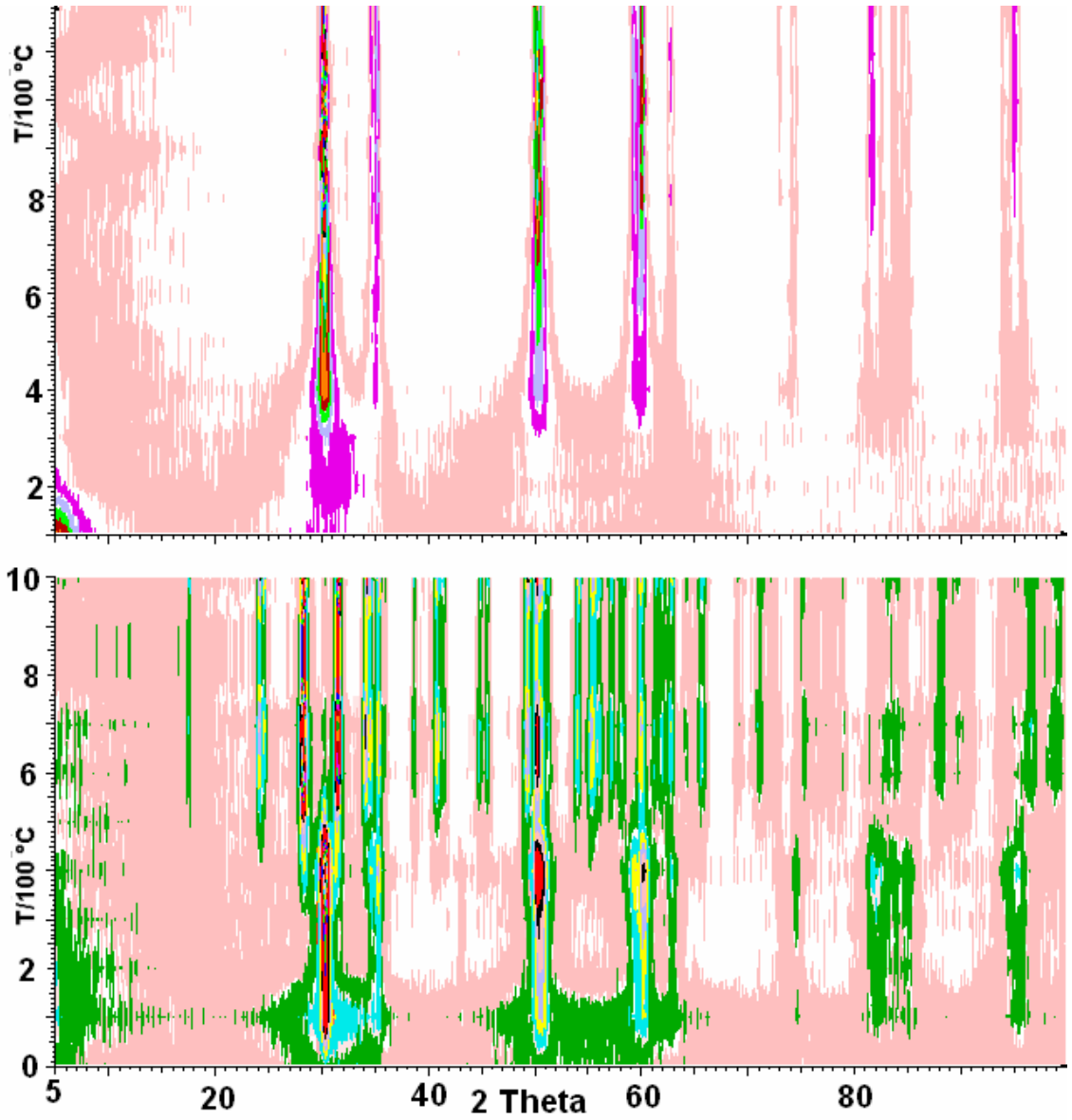

Figure 8.16. *Top: XRD contour maps (count rate vs. Bragg angle and temperature). The count rate is colour coded. Experiments were conducted ex situ after quenching samples from the temperatures indicated. Top: YSZ (8.7 mol%), bottom: pure (unstabilised) zirconia. The latter exhibits a phase transition on quenching when baking temperatures exceed 500°C.*

8.2.7 The nucleation and YSZ process

Figure 8.17 is a schematic of the formation of sol-gel derived YSZ based upon the results of the experiments. Initially, there is a homogeneous distribution of yttria and zirconia primaries in the xerogel. Upon heating, the zirconia will crystallise, incorporating the yttrium ions as the crystals grow. This induces an initial inhomogeneity which becomes apparent by changes in the resonant term on zirconium ASAXS. The final result is pure cubic phased yttria stabilised zirconia in a homogenous distribution; shown in ASAXS by the three scattering functions identical in shape, but differing in intensity.

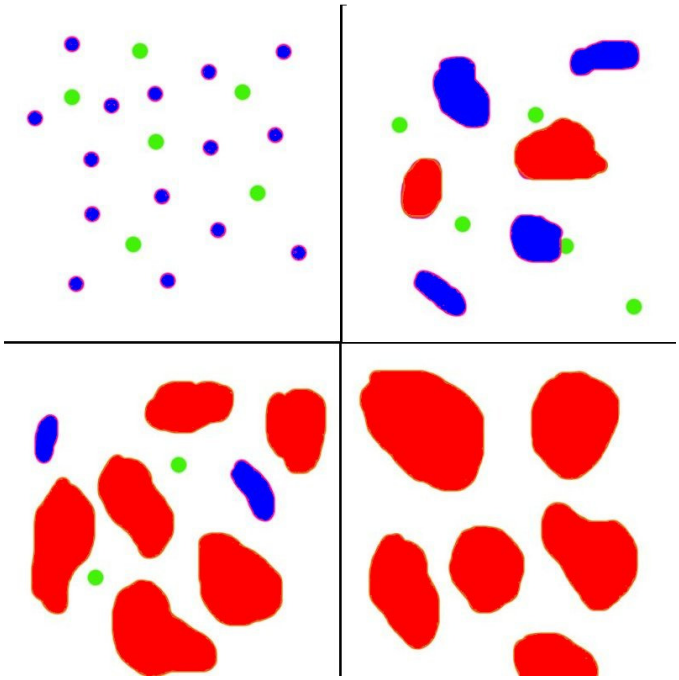

Figure 8.17*: Schematic of the formation of YSZ on heating. Starting from top left: Nucleates of zirconia (blue) grow, absorbing the yttria (green) as they go along - resulting in an initial mixed phase state (top right and bottom right). The material becomes single phase YSZ (red) once all the Yttria has been incorporated into the growing zirconia crystals.*

Chapter 9

Conclusion

It has been shown that Anomalous Small Angle X-ray Scattering (ASAXS) is a useful tool for investigating the sol-gel process. The ability of ASAXS to resolve the scattering functions of individual species within a composite material will also prove useful in acquiring a greater understanding in similar processes with chemical contrast variations in the nano-regime.

Modern synchrotron radiation sources are ideal for time resolved ASAXS experiments due to the high photon flux produced. The only other constraints are the speed in which a beam-line monochromator can cycle the different energies, and the beam spectrum obtained from the monochromator crystals.

9.1 Conclusions on gelation

Time resolved ASAXS on Zirconia and yttria-zirconia in silica reveal the zirconia and yttria primary particles are being fully integrated into the structure of the gel network. ASAXS reveals contrast in the resonant term on the zirconium edge, with the normal and cross terms having identical forms.

By comparison, the addition of zinc ions into the formation of a silica gel reveal the zinc primaries are not being incorporated into the network structure, but rather remain trapped inside gel pores.

In situ EXAFS experiments, ran in parallel with the ASAXS investigations, show a chemical shift of 2.8eV on the zirconium edge during hydrolysis. Once fully hydrolysed, the position of the absorption edge remains constant.

Varying yttria concentration shows no change on the form of the scattering patterns from sols during gelation.

9.2 Conclusions on the sintering of yttria stabilised zirconia

YSZ and YSZ in a silica matrix has been successfully prepared by the sol-gel method, and the roles yttrium and zirconium ions play during sintering have been investigated using *in situ* double ASAXS over two adjacent absorption edges. The presence of a silica matrix slows crystal growth. This growth rapidly increases beyond 780°C, and is also shown in XRD studies. SAXS plots reveal the thermally driven growth of cubic phased nanocrystals averaging 10 nm in size, which is shown by the presence of a scattering factor maximum. The particle sizes determined from SAXS correlate with those obtained from XRD.

Accurate determination of the atomic scattering factors using X-ray absorption spectra is important to make sure the correct solutions for the normal, cross and resonant terms are obtained. The resonant term in zirconium ASAXS displays a narrowing of the

scattering factor maximum, as well as a peak position at lower values of q, and hence a larger particle size. This is interpreted as being due to zirconia playing the dominant role during nucleation. Pure zirconia crystals initially nucleate and absorb yttria as they grow, resulting in stabilisation of the cubic phase. Contrast between the normal and resonant terms vanishes as the temperature increases and all the yttria is absorbed into YSZ, making the sample homogeneous. Yttrium ASAXS shows no observable difference between the normal, cross and resonant terms for typical YSZ where the yttrium concentration is much lower than that of zirconia.

9.3 Future Work

Further work needs to be performed in the study of yttria stabilised zirconia in a silica matrix. Particularly at temperatures beyond 900°C, where a second reaction appears to occur. Sintering experiments need to explore higher temperatures, preferably over 1000°C (to obtain a good range of data) to fully investigate the formation of yttrium silicate.

Investigations should also be performed on different materials, such as YAG formation and superconducting ceramics such as YBCO. Reactions from materials prepared by sol-gel can be compared to those prepared using other industrial methods.

Additionally, ASAXS itself needs to be properly modelled. A computer simulation that generates scattering functions of the normal, cross and resonant terms from user defined materials needs to be produced, which can then further aid the experimenter in

interpreting results. ASAXS experiments on known systems will need to be carried out to assist and validate simulator development.

A project to derive theoretical values of the corrections to the atomic scattering functions (f' and f'') for compounds should also be completed. To date, only the values for pure metals have been derived. No attention has been given to compounds such as oxides. With such models, better fits can be derived when comparing experimental and theoretically derived data.

The techniques of ASAXS can be combined with those of Grazing Incidence SAXS (GISAXS) in order to facilitate time resolved AGISAXS experiments in the study of thin films - such as photovoltaic cells. AGISAXS experiments can also be performed on YSZ films and reactions compared to the results obtained from bulk samples.

Further work should also be carried out in the application of ASAXS style techniques to longer wavelengths. Novel spectroscopic light scattering experiments can be designed using the visible and infrared wavelengths. Here, the anomalous scattering will be the result of molecular absorption – and can be used in the study of biological processes.

Afterthoughts

With synchrotron designs and beam-lines constantly improving, the potential time-resolution and beam-spectra can only improve further. Synchrotron facilities constantly look for new, innovative experimental ideas – posing additional challenges to beam-lines and their staff. These new challenges will enable the synchrotron facility to remain on the

front line of cutting edge research, as experimental demands from research institutes increase.

ASAXS has a great potential, and shows a wealth of promise in the unravelling of further mysteries in the future. With time resolution at I22, Diamond Light Source, now approaching the milli and micro-second regime, ultra high time resolved ASAXS experiments are now within grasp. In addition, anomalous scattering techniques can be applied to Grazing Incidence SAXS (GISAXS), to one day produce the first ever time resolved AGISAXS experiment in the study of thin films.

In the future, the next generation of beam-line designs could utilise ultra high power free electron lasers (FEL), capable of generating intense monochromatic beams of UV, X-ray and gamma photons using inverse Compton scattering [85]. It could be that eventually the synchrotron as we know it will become obsolete, as new, laboratory sized beam-lines are designed; though this will be someway off in the future – and maybe a topic for our children and grandchildren.

Though current SAXS beamlines can only probe energies of between 4keV and 22keV at best, it is not impossible to envisage anomalous scattering experiments of much lower energies, capable of exploring the absorption edges of smaller atoms. Such "Anomalous Small Angle UV Scattering" and "Anomalous Small Angle Light Scattering" experiments could be exploited to investigate complex biological and biochemical processes. Visible light and infra-red energies are also within range of many molecular absorption spectra, making novel spectroscopic scattering experiments very plausible to investigate in-situ changes of micro-structures in biochemical materials and polymers.

References

1. Von Ebelman J., *Ann.Chem*. **1846**, *57*, 319

2. Kozhukharov S., *J. Chem Tech and Metallurgy*. **2009**, *44*, 143-150

3. Roy D. M., Roy R., Osborn E. F., *J. Am Ceram Soc.*, **1953**, *36*, 185

4. Roy R., *J Am Ceram Soc*., **1956**, *39*, 145

5. Shroeder H., *Opt Acta*, **1962**, *9*, 249

6. Dislich H., *J. Non Cryst. Solids*, **1985**, *73*, 599-612

7. Brinker, C. J., Scherer, G. W. *Sol-Gel Science, The Physics and Chemistry of Sol-Gel Processing*, **1990**, *Academic Press*, pp97-216

8. Lours T., Zarzycki J., Craievich A., Dos Santos D.I., Aegerter M. A., *J Non Cryst. Solids* **1987** *95* 1151

9. Saliger R., Heinrich T., Gleissner T., Fricke J., *J Non Cryst. Solids* **1995** *186* 113

10. Itoh M., Hattori H., Tanabe K. J., *J Catal.*, **1974**, *35*, 225

11. Lopez T., Tzompantzi F., Narvarrete J., Gornez R., Boldu J. L., Munoz E., *J Catal* **1999**, *181*, 285

12 Miller J. B., Ko E. I., *J. Catal,* **1996**, *159*, 58

13 Zhuang Q., Miller J. M., *Can. J. Chem.*, **2001**, *79*, 1220

14 Pope E. J. A., Mackenzie J. D., *J Am Ceram. Soc.* **1993**, *76 (5)*, 1325-1328

15. Subbarao, E. C., Maiti, H S. *Solid State Ionics* **1984**, *11 (4)*, 317-338

16. Brown, G., Halback K., Harris J., Winick H.., *Nuclear Instruments and Methods.* **1983,** *208,* 65-77

17. Brinker, C. J., Scherer, G. W. *Sol-Gel Science, The Physics and Chemistry of Sol-Gel Processing*, **1990**, *Academic Press*, pp22-59

18. Sarkisov P. D., Orlova A., Popovich N. V., Anan'eva Yu. E., *Glass and Ceramics*, **2007**, *64*, 3

19. Nassar E. J., Nassor E. C., Ciuffi K. J., *J Mater Sci,* **2007**, *42*, 2244-2249

20. Potdevin A., Chadeyron G., Boyer D., Mahiou R., *J Sol-Gel Sci Techn*, **2006**, *39*, 275-284

21 Lecomte A., Dauger A, Lenormand P., *J Appl. Cryst*, **2000**, *33*, 496-499

22 Yu L., Nogami M., *J Sol-Gel Sci Techn* **2007**, *43*, 355-360

23 Saboori A., Rabiee M., Moztarzadeh F., Sheikhi M., Tahriri M., Karimi M., *Materials Science and Engineering C*, **2009**, *29*, 335-340

24 Stein A., Fendforf M., Jarvie T. P., Mueller K. T., Benesi A. J., Mallouk T. E., *Chem Mater.* **1995**, *7*, 304-313

25 Boyer D., Derby B., *J Am Ceram Soc.*, **2003**, *86 (9)*, 1595-1597

26 Znaidi L., Soler Illia G. J. A. A., Le Guennic R., Sanchez C., *J Sol-Gel Sci Techn*, **2003**, *26*, 817-821

27 Chervin C. N., Clapsaddle J., Chiu H. W., Gash A. E., Satcher J. H., Kauzlarich S. M., *Chem Mater.*, **2006**, *18*, 4865-4874

28 Cui H., Zayat M., Levy D., *J Sol-Gel Sci Techn*, **2005**, *35*, 175-181

29. Zhang J., Feng H., Hao W., *J Sol-Gel Sci Techn*, **2006**, *39*, 37-39

30 Mikrajuddin F., Iskandar F., Okuyama K., Shi F. G., *J App Phys*. **2001**, *89 (11)*, 6431-6434

31 Lecomte A., Blanchard F., Dauger A., Silva M. C., Guinebretiere R., *J Non-Cryst Solids*, **1998**, *225*, 120-124

32 Oliphant M.O. *The acceleration of particles to very high energies. University of Birmingham Archive* **1943**

33. Veksler V. I. *Comptes Rendus de l'Academie Sciences*, **1944**, *43 (8)*, 329-331

34. McMillan E. M., *Phys Rev*. **1945**, *68*, 143

35. Elder F.R., Gurewitsch A. M., Langmuir R. V., Pollocl H. C., *Phys Rev*. **1947**, *71(11)*, 829-830

36 Koch E., *Handbook on Synchrotron Radiation, Vol 1a*, **1983**

37. Livingston M. S., Blewett J. P., *Particle Accelerators*, **1962**, *McGraw-Hill, New York*

38. http://www.diamond.ac.uk

39. http://www.srs.ac.uk/srs/station6.2.htm

40 http://www.diamond.ac.uk/Home/Beamlines/I22.html

41 http://www.bessy.de/bit/bit_show_object.html.php?i_bit_id_object=260

42 Yabashi M., Tamasaku K., Kikuta S., Ishikawa T., *Rev Sci Instrum*. **2001**, *72*, 4080

43 Fresnel A. Oeuvres completes (Impreimerie Imperiale, Paris, 1866), t. 1, 254-255

44. Crew H., The Wave Theory of Light (American Book Company, New York) 1900

45 Newton Sir I, Opticks: Or a Treatise of the Reflexions, Refractions, Inflexions and Colours of Light (London), 1730

46 Maxwell J. C., A Dynamical Theory of the Electromagnetic Field, Philosophical Transactions of the Royal Society of London1865, 155, 459-512

47 http://www.cambridgephysics.org/physicists/bragg_prelim.html

48 Guinier A., Fournet G., *Small Angle Scattering of X-Rays*, **1955**, *Wiley*

49. Glatter O., Kratky O., *Small Angle X-Ray Scattering*, **1982**, *Academic Press*

50 Fournet, G, *Bull Soc. Fr. Mineral. Crystallogr*. **1951**, *74*, 39-113

51 Rayleigh J.S. *Scientific Papers (vol 6: 1911-1919)*, **1899-1920**, *Cambridge University Press*

52 Guinier A., Fournet G., *Small Angle Scattering of X-Rays*, **1955**, *Wiley*, *p19-21*

53 Le Messurier, D., Winter, R., Martin, C. M., *J. Applied Crystallography,* **2006**, *39*, 589-594

54 Materlik G., Sparks C. J., Fischer K., *Resonant Anomalous X-ray Scattering*, **1994**, *Elsevier*

55 Kronig L., De R., *J. Opt Soc Am.*, **1926**, *12*, 547-557

56 Kramers H. A., *La diffusion de la lumiere par les atomes, Atti Cong. Intern. Fisica, (Transactions of Volta Centenary Congress) Como*, **1927**, *2*, 545-557

57 Cromer D. T., Liberman D., *J Chem Phys*, **1970**, *53*, 1891

58 Winter R., Le Messurier D., Martin C. M., *Cryst Rev*. **2006**, *12*, 3

59. Kirby, N., Cookson, D., Buckley, C., Bovell, E., St Pierrre, T., *J. Applied Crystallography*, **2007**, *40*, p402-p407

60. Brumberger, H., Hagrman, D., Goodisman, J., Finkelstein, K. D., *J Applied Crystallography*, **2005**, *38*, 147-151

61. Morfin, I., Ehrburger-Dolle, F., Grillo, I., Livet, F., Bley, F., *J. Synchrotron Radiation*, **2006**, *13*, 445-452

62. Goerigk G, Haubold HG, Schilling W, *J Appl Cryst*, **1997**, *30*, 1041

63 Haug J., Krath H., Dubiel M., Hofmeister H., Hauss S., Tatchev D., Hoell A., *Nanotechnology*, **2009**, *20*, 505705

64 Barnardo T., Hoydalsvik K., Winter R., Martin C. M., Clark G. F., *J Phys Chem C.*, **2009**, *113*, 10021-10028

65 Guinebretiere R., Dauger A., Lecomte A., Vesteghem H., *J. Non Cryst Solids*, **1992**, *147&148*, 542-547

66 Basta M., Picciarelli V., Stella R., *Eur J. Phys,* **1991**, *12*, 210-213

67 Budrugeac P., Musat V., Segal E., *J. Thermal Analysis and Calorimetry*, **2007**, *88*, 699-702

68 Bel Hadj Tahar R., Bel Hadj Tahar N., *J. Materials Science*, **2005**, *40*, 5285-5289

69 Izaki M., Takashi O., *Appl Phys Let*. **1996**, *68 (17)*, 2439-2440

70 Kim Y. J., Shang H., Cao G., *J. Sol-Gel Sci Techn*, **2006**, *38*, 79-84

71 Tokumoto M. S., Briois V., Santilli C. V., Pulcinelli S. H., *J. Sol-Gel Sci Techn*, **2003**, *26*, 547-551

72 Sakohara S., Mori K., *J. Nanopart Res*, **2008**, *10*, 297-305

73 http://skuld.bmsc.washington.edu/scatter/AS_periodic.html

74 Brugemann L., Gerndt E. K. E., *Nuclear Instruments and Methods in Physics Research Section A: Accelarators, Spectrometers, Detectors and Associated Equipment.* **2004**, *53 (1)*, 292-301

75 Ishikawa T., Tamasuku K., Yabashi M., *Nuclear Instruments and Methods in Physics Research Section A: Accelarators, Spectrometers, Detectors and Associated Equipment.* **2005**, *547 (1)*, 42-49

76 Verbeni R., Sette F., Krisch M. H., Bergmann U., Gorges B., Halcoussis C., Martek K., Masciovecchio C., Ribois J. F., Ruocco G., Sinn H., *J. Synchrotron Rad.,* **1996**, *3*, 62-64

77. Cornik R. J., Barnes P, Bushnell-Wye G., Dent A. J., Diakun G. P., Flaherty J. V., Greaves G. N., Heeley E. L., Helsby W., Jacques SA D. M., Kay J., Rayment T., Ryan A., Tang C. C., Terrill N. J., *J Synchrotron Rad.* **2004**, *11*, 163-170

78 Rubio F., Rubio J., Oteo J. L., *J Mater Sci Letters,* **1997**, *16 (1)*, 49-52

79 http://cmt.dur.ac.uk/sjc/thesis/thesis/node79.html

80 Ballauff, M., Jusufi, A., *Colloid Polym Sci* **2006**, *284*, 1303-1311

81 Torma V., Peterlik H., Bauer U., Rupp W., Husing N., Bernstorff S., Steinhart M., Georigk G., Shubert U. *Chem. Mater.* **2005**, *17*, 3146-3153

82 Mroweic-Bailon J., Pajak L., Jarzebski A. B., Lachowski, A. I., Malinowski, J. J., *J. Non-Cryst. Solids*, **1998**, *3 (C8)*, 385.

83 Green D. J., Hannink R., Swain M. V., *Transformation Toughening of Ceramics*. **1989**, *CRC Press*

84 Scherrer P., *Gottinger Nachrichten Gesell,* **1918**, *2*, 98

85 DOE/ Argonne National Laboratory, *World's First X-ray Free Electron Laser is on Course to Completion, Science Daily.* **July 2, 2007.**